

# **Projectile X-Ray Emission in Relativistic Ion-Atom Collisions**

Dissertation  
zur Erlangung des Doktorgrades  
der Naturwissenschaften

vorgelegt beim Fachbereich Physik  
der Goethe-Universität  
in Frankfurt am Main

von  
Shadi Mohammad Ibrahim Salem  
aus Amman (Jordanien)

Frankfurt am Main 2010

vom Fachbereich Physik der Goethe-Universität  
als Dissertation angenommen.

Dekan:	Prof. Dr. Dirk-Hermann Rischke
Gutachter:	Prof. Dr. Thomas Stöhlker
	Prof. Dr. Reinhard Dörner
Datum der Disputation:	16.03.2010

# Contents

<b>1</b>	<b>Introduction</b>	<b>3</b>
<b>2</b>	<b>Theoretical Background</b>	<b>7</b>
2.1	The theoretical treatment of the atomic systems in relativistic collisions . . . . .	7
2.2	Projectile Excitation and Ionization at Relativistic Energies . . .	8
2.2.1	Excitation and Ionization Probability . . . . .	9
2.2.2	The Simultaneous Excitation and Ionization process . . .	14
2.2.3	Calculated Probabilities in the Independent Particle Model	14
2.3	Electron Capture Studies . . . . .	16
2.3.1	Radiative recombination (RR) . . . . .	16
2.3.2	Radiative versus non-radiative electron capture . . . . .	18
2.3.3	Non-relativistic dipole approximations versus exact relativistic treatment of REC capture . . . . .	23
2.4	Alignment of the excited ion states populated via REC . . . . .	26
<b>3</b>	<b>The Experiment</b>	<b>31</b>
3.1	The production of highly-charged heavy ions . . . . .	31
3.2	The Experimental Storage Ring ESR . . . . .	34
3.2.1	The Electron Cooler in the ESR . . . . .	34
3.2.2	The Internal Gas-Jet Target of the ESR . . . . .	39
3.3	The Experimental setup . . . . .	41
3.3.1	The Interaction Chamber . . . . .	41
3.3.2	The X-ray Detectors . . . . .	43
3.3.3	The particle detector . . . . .	43

3.4	Signal Processing and Data Acquisition System . . . . .	45
<b>4</b>	<b>Data Analysis</b>	<b>47</b>
4.1	Doppler Corrections: The Doppler Shift and the Doppler Broadening . . . . .	48
4.2	Detection Efficiency of the x-ray detectors . . . . .	51
4.2.1	Detection efficiency definition . . . . .	51
4.2.2	Physical description of the efficiency-energy relationship	52
4.2.3	Model calculation and discussion . . . . .	59
4.3	The Simultaneous Excitation and Ionization process . . . . .	61
4.4	Single Excitation of He-like uranium ions . . . . .	67
4.5	Analysis of the REC spectra . . . . .	69
<b>5</b>	<b>Results and Discussion</b>	<b>75</b>
5.1	K-shell Excitation of He-like Uranium Ions . . . . .	75
5.2	Electron Capture into H-like Uranium Ions . . . . .	77
5.2.1	$K_{\alpha 1}/K_{\alpha 2}$ Intensity Ratio for REC into $U^{91+}$ . . . . .	77
5.2.2	$Ly_{\alpha 1}/Ly_{\alpha 2}$ Intensity Ratio for REC into $U^{91+}$ . . . . .	78
5.2.3	Differential K-REC Cross Sections . . . . .	80
5.3	Simultaneous ionization and excitation in the $U^{90+} \rightarrow Xe$ collisions . . . . .	83
<b>6</b>	<b>Summary and Outlook</b>	<b>89</b>
<b>7</b>	<b>Zusammenfassung</b>	<b>93</b>

# Chapter 1

## Introduction

Ion-atom collisions is a class of physical phenomena in which radiation can be emitted when an energetic charged ion impinges on a neutral atomic system. During ion-atom collisions, the excitation and/or the ionization of bound electrons of the collision partners can occur and also electrons can be transferred from one collision partner to the other. Although the basic processes have been studied in great detail during the last decades in different collision systems, there are still many aspects which are not fully understood and deserves further investigations. Of a considerable interest are still the many-electron processes in atomic collisions. These effects are produced by a significant mutual interaction of two electrons whose theoretical description requires an extension of the independent-electron model. The understanding of these phenomena requires an understanding of the many-body problem encountered in atomic collisions. Many-electron processes have been studied, both experimentally and theoretically, mainly for non-relativistic systems [1, 2]. Most previous experiments have focused on two-electron processes in helium [3, 4, 5, 6], since this is the simplest system containing more than one electron [7]. Total cross sections of multiple processes for a two-electron system in collisions with neutral targets at low velocities have been studied. These studies include measurements of capture-ionization [8, 9], capture-excitation [10], double capture [11] and double excitation [12].

The availability of heavy highly-charged ions in a large energy domain open new possibilities for multiple processes investigations in few-electron ions, be-

yond the helium atoms. One of such opportunity is the study of the simultaneous ionization and excitation in helium like heavy ions in single collisions with neutral target atoms. The virtue of investigating the process of simultaneous excitation and ionization is that one electron ends up in the continuum, while the other electron ends up in a hydrogen like final state which simplifies the theoretical treatment of the phenomena.

Experimentally, the identification of excitation-ionization events are greatly facilitated in the case of He-like ions where electron capture cannot lead to ground state x-ray emission due to the initially occupied  $K$ -shell. It is important to mention here, that in the experiments using solid targets [13], a measurement of two-electron processes is more difficult due to the high probabilities of excitation and ionization occurring in two successive collisions. In contrast, for gas targets with typical area density of  $10^{12}$  particles/cm<sup>2</sup> the probability for a two-step excitation and ionization process is negligible. The cross section of the simultaneous ionization and excitation process can be determined directly from the  $Ly_\alpha$  radiation measured in coincidence with the projectile having lost one electron.

Radiative transitions in high- $Z$  heavy ions play a key role in understanding the effects of strong Coulomb fields on the electronic structure of atoms and ions. At high- $Z$  the transition rates and energies are strongly affected by relativistic corrections and quantum electrodynamics effects (QED) show up in a clear way [14]. One of the most prominent examples is the  $Ly_\alpha$  transition in hydrogen like ions. In the case of transition rates, relativistic effects are manifested by the strongly enhanced importance of magnetic transitions; the  $2s_{1/2}$  decay in high- $Z$  one-electron ions is almost entirely governed by  $M1$  transitions quite in contrast to the dominant  $2E1$  decay at lower  $Z$  [15]. For heavy He-like ions the two ground state transition, the  $K_{\alpha 1}$  and  $K_{\alpha 2}$  lines are possible. Each line comprises two components; the  $K_{\alpha 1}$  line is composed by the ground state transitions from  $^1P_1 (E1)$  and  $^3P_2 (M2)$  states and the  $K_{\alpha 2}$  line by the ones from  $^3S_1 (M1)$  and  $^3P_1 (E1)$  states. Also the continuous spectrum from  $2E1$  decay of the  $^1S_0$  level may be slightly blended by contributions from  $E1M1$  decay of the  $^3P_0$  state [16, 17]. To be able to account for the magnetic interaction one should consider the coherent sum of the magnetic and the

electric amplitudes of the interaction potential, namely, the Liénard-Wiechert potential [18].

For two-electron high- $Z$  ions, the formation of excited states via Coulomb excitation can be studied by the observation of the radiative decay of the excited levels to the ground state. With increasing nuclear charge, the electron-electron correlation effects are small with respect to the Coulomb interaction between the electrons and the charge of the nucleus. Hence, for high- $Z$  He-like ions the excitation cross sections should be almost unaffected by the presence of the second electron.

For He-like uranium the energy difference between the two-components of the  $K_{\alpha 1}$  line, the  $^1P_1$  and  $^3P_2$  states, is around  $64\text{ eV}$ . Up to now, this energy could not be resolved experimentally due to the limited energy resolution of the germanium detectors.

Within the last years, a new generation of experiments measuring the transitions in few-electrons high- $Z$  ions have been performed at the GSI Helmholtzzentrum für Schwerionenforschung GmbH in Darmstadt. In these experiments [19, 20], the excited ionic states are produced by means of radiative capture of a free electron by heavy ions. In the electron cooler at Experimental Storage Ring (ESR), an ion can recombine with a free electron by one of two basic interaction processes: the radiative recombination RR (*see chapter 2*), and dielectric recombination DR [21, 22, 23, 24]. Under certain conditions, the cross section for radiative electron capture (REC) can be much larger than the cross section for nonradiative capture NRC (*see Chapter 2*). Theoretically, the electron capture in relativistic projectiles has been explained by Anholt and Eichler [18, 25, 26, 27, 28].

Examples include the REC into the  $2p_{3/2}$  state of initially bare and  $^1P_1$ ,  $^3P_2$  states of initially H-like uranium ions as well as their subsequent  $Ly_{\alpha 1}$  ( $2p_{3/2} \rightarrow 1s_{1/2}$ ) and  $K_{\alpha 1}$  ( $^1P_1$ ,  $^3P_2 \rightarrow ^1S_0$ ) radiative decays. A rather surprising theoretical result of these studies is the qualitatively different angular behavior of the x-ray emission from the finally H-like as opposed to He-like ions: while the  $Ly_{\alpha 1}$  radiation exhibited a strong angular dependence, the  $K_{\alpha 1}$  decay gives rise to an almost isotropic emission pattern [29]. Theoretically the behavior of the  $K_{\alpha 1}$  radiation was explained by Surzhykov *et al.* [30].

The present work concentrates on three major tasks. First, the identification of two-electron processes in relativistic heavy ions collisions by measuring the  $Ly_\alpha$  lines of the initially He-like projectile. Second, the formation of the magnetic sublevels by Coulomb excitation as well as by electron capture. The information can be obtained from the study of the angular distribution of  $Ly_{\alpha 1}$  and  $K_{\alpha 1}$  associated with these processes. Third, a particular attention has been paid to the study of the angular distribution of  $K$ -REC photons close to zero degrees which contains information about the contribution of the so called 'spin-flip' of the captured electron.

For this, measurements of  $220 \text{ MeV}/u \text{ } U^{90+} \rightarrow Xe$  and  $U^{91+} \rightarrow N_2$  were performed and analyzed. This study provides a complement to the existing experimental data for the domain of strong Coulomb fields and for energies where relativistic effects play an important role.

This thesis is organized as follows: the theoretical aspects of the simultaneous excitation-ionization and the electron capture in few-electron high-Z projectiles are discussed in **Chapter 2**. The basic concepts of the REC and NRC are discussed by introducing the cross sections for each process. Also a summary of the theory of photon angular distributions in terms of alignment parameters is given at the end of this chapter. In **Chapter 3** the experimental details are discussed. It describes the interaction chamber, the gas-jet target and the characteristic features of the x-ray and particle detectors used in the experiment. A short description of the electronics and data acquisition system is also given in this chapter. In **Chapter 4** details of the data analysis are discussed. **Chapter 5** focuses on the calculated cross sections and the observed angular distribution compared to the relativistic calculations based on the perturbation theory and the single electron model. The performed measurements and the obtained results, with an outlook on further experiments, are summarized in **Chapter 6**. In **Chapter 7**, a summary of the present work in German language is given.



# Chapter 2

## Theoretical Background

### 2.1 The theoretical treatment of the atomic systems in relativistic collisions

Generally, atomic collisions studies focus on the electrons behavior during the collision while the *nuclei* mainly serve as sources of the time-varying electromagnetic fields. If many-electron atoms are involved in the collision, the dynamics become very complicated. To avoid complications arising from many-body effects, the existing theoretical treatments mainly concentrate on a three-body ion-atom collision system, comprising a projectile nucleus, a target nucleus, and an electron. For example, for processes involving inner-shell electrons, the one-electron model is a good approximation. In principle, all particles involved, electrons and nuclei, must be described theoretically by quantum mechanics. For systems where the projectile charge is much larger than the target charge,  $Z_P \gg Z_T$ , undergoing fast collisions, The approach, called the "semiclassical approximation" (SCA) or "impact parameter picture" can be used. For a fast collision and for collision distances comparable with, or larger than the atomic  $K$ -shell radius, the transient perturbation of the target atom by the projectile is small enough that the first-order time dependent perturbation theory is expected to be a good approximation, even for high- $Z$  projectile. This approximation imply an important simplification for heavy-ion collisions with an energy exceeding a few  $MeV/u$  .

While the electrons interaction with the radiation field can be treated only by perturbation theory, their interaction with the atomic field can, in principle, be handled exactly. For that, exact solutions of the Dirac wave equation 2.1 are required. The Dirac equation is given by [31]:

$$(c\vec{\alpha} \cdot \vec{p} + \vec{\beta} m_e c^2 + V(\vec{r}))\psi(\vec{r}) = E\psi(\vec{r}); \quad (2.1)$$

where  $\psi$  is the wave function of a particle of mass  $m$  which is in the Coulomb potential  $V$ ,  $\vec{p}$  is the linear momentum of the electron,  $\vec{\alpha}$  and  $\vec{\beta}$  are the  $4 \times 4$  Dirac matrices. This equation successfully formulated the relativistic equation for an electron moving in a Coulomb field, which automatically guaranteed the spin and magnetic moment of the electron.

## 2.2 Projectile Excitation and Ionization at Relativistic Energies

The theoretical description of excitation and ionization in helium like systems relies on two assumptions. First, the process is described within the framework of the independent particle approximation (IPA), in which the electrons are assumed to move independently of each other in the average field generated by the nucleus and the other electrons. Therefore in this approximation, the processes of the excitation and ionization are not correlated. Second, the single electron processes are described in the assumptions of the classical trajectory model of the inter-nuclear motion.

For a classical description of atomic collisions, it is useful to introduce the concept of the impact parameter. It is assumed that, during the collision, the particle follows a classical trajectory with an incoming and an outgoing branch (*see figure 2.1*). The asymptote to the incoming branch is parallel to the beam direction while the asymptote to the outgoing branch defines the deflection angle  $\theta$  with respect to the incoming beam direction. The distance from the scattering center to the projectile is denoted as the impact parameter  $\mathbf{b}$ , where the bold notations denote vectorial quantities.

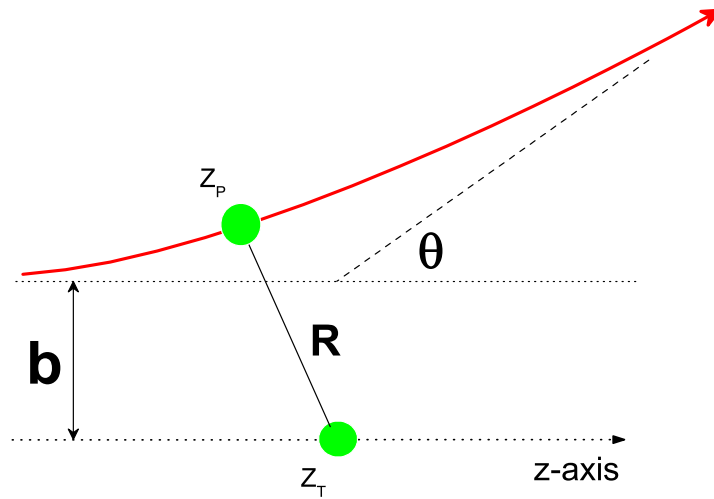


Figure 2.1: The classical trajectory of a particle in the laboratory system, defined by the impact parameter  $\mathbf{b}$  and the scattering angle  $\theta$ .

### 2.2.1 Excitation and Ionization Probability

For the calculation of the transition probabilities and of the cross section for excitation of high- $Z$  projectile ions, at relativistic velocities, a complete Liénard-Wiechert interaction potential must be considered [28].

#### Liénard-Wiechert potential

Assuming the impact parameter picture, the projectile moves with constant velocity  $v$  at an impact parameter  $b$  along a classical straight-line trajectory (see figure 2.2) which, in the laboratory system, is given by:

$$\mathbf{R} = \mathbf{b} + \mathbf{v}t. \quad (2.2)$$

When defining the coordinate systems, it is convenient to place the target nucleus at the origin of the laboratory system with the  $x$  and  $z$  axes taken in the directions of  $\mathbf{b}$  and  $\mathbf{v}$ , respectively. The projectile nucleus is located at the origin of the moving emitter system with the coordinates  $(x', y', z')$ . The electron  $e^-$  has the coordinate  $\mathbf{r}$  with respect to the target frame and  $\mathbf{r}'$  with respect to the projectile frame.

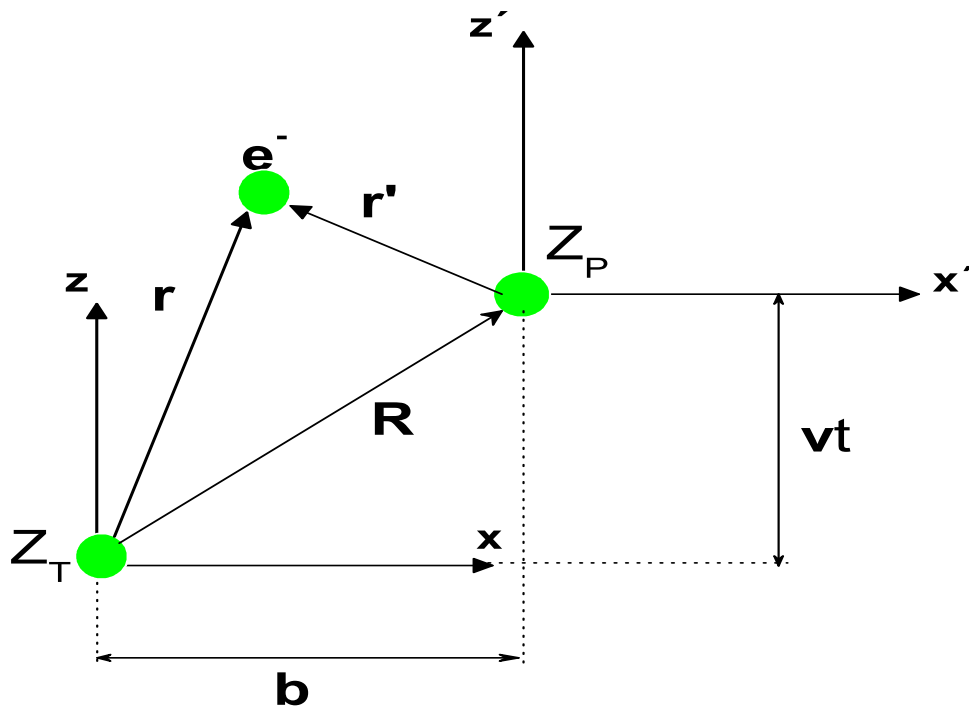


Figure 2.2: The coordinate systems, laboratory and emitter frames, for a collision between two atoms: the target and  $Z_T$  the projectile  $Z_P$  [28].

In the projectile frame, the electrostatic potentials (scalar and vector) created by the projectile charge  $Z_P \cdot e$  can be described by the following equations:

$$\Phi'(r', t') = \frac{Z_P \cdot e}{r'} \quad (2.3)$$

$$\mathbf{A}(r', t') = 0. \quad (2.4)$$

From figure 2.2, the electron-projectile distance as seen in the projectile system, ( $r'$ ) can be expressed as:

$$r' = \sqrt{(x - b)^2 + y^2 + \gamma^2(z - vt)^2}. \quad (2.5)$$

By using the Lorentz transformation, the Liénard-Wiechert potential produced by the projectile in the target frame are:

$$\Phi(r, t) = \frac{\gamma Z_P \cdot e}{\sqrt{(x-b)^2 + y^2 + \gamma^2(z-vt)^2}} \quad (2.6)$$

and

$$\mathbf{A}(r, t) = \frac{\mathbf{v}}{c} \Phi(r, t). \quad (2.7)$$

From the basic equations of electrodynamics the electric field  $\mathbf{E}$  is expressed in terms of the potentials  $\mathbf{A}$  and  $\Phi(r, t)$  as [32]:

$$\mathbf{E} = -\frac{1}{c} \frac{\partial \mathbf{A}}{\partial t} - \nabla \Phi. \quad (2.8)$$

In particular, the electric field produced by the charge  $Z_P \cdot e$  at the position of the target nucleus is directed radially from the projectile's position to the observation point at the target nucleus. Writing  $b = R \sin \theta$  and  $vt = R \cos \theta$ , one can obtain [18]:

$$\mathbf{E} = \frac{-Z_P \cdot e \mathbf{R}}{\gamma^2 R^3 (1 - \beta^2 \sin^2 \theta)^{3/2}}. \quad (2.9)$$

The angular dependence of the electric field strength is illustrated in figure 2.3 for various projectile velocities in terms of the Lorentz factor  $\gamma$ . Along the direction of motion, the field strength is decreased by a factor of  $\gamma^{-2}$  as compared to a charge at rest. On the other hand, perpendicular to the trajectory, the field is increased by a factor of  $\gamma$ . The flattening of the surface into disk shapes is an effect of the Lorentz contraction of the electromagnetic fields.

### First-order perturbation theory

The first-order time-dependent perturbation theory is expected to be a good approximation if the transient perturbation of the target atom by the projectile is small. This condition is valid only for a fast collision and if the impact parameter is comparable with the atomic K-shell radius [28].

To calculate the cross section between any pair of specified initial and final states,  $i$  and  $f$ , the impact parameter dependent transition probability can be expressed in terms of the transition amplitude  $A_{fi}$

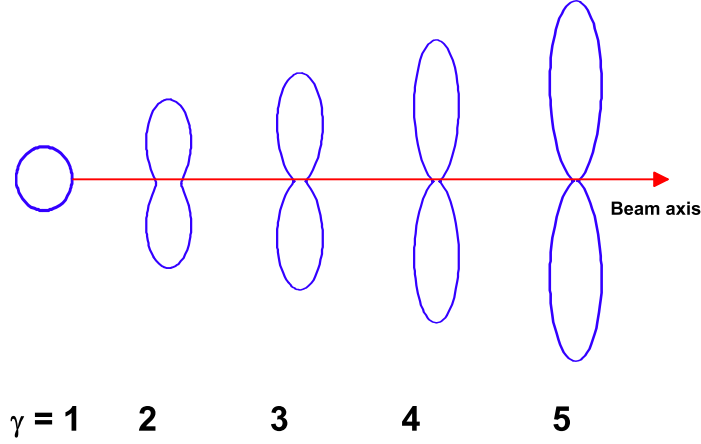


Figure 2.3: Polar diagrams for the angular dependence of the electric field strength produced by a point charge moving with the velocity  $v$  to the right.

$$P_{fi}(b) = |A_{fi}|^2 \quad (2.10)$$

The transition amplitude for excitation of a projectile electron can be written as [18]:

$$A_{fi}(b) = i\gamma Z_P e^2 \int dt e^{i(E_f - E_i)t} \int d^3r \psi_f^\dagger(\mathbf{r}) \frac{1 - \beta \hat{\alpha}_z}{r'} \psi_i(\mathbf{r}), \quad (2.11)$$

where  $\gamma = (1 - \beta^2)^{-1/2}$ ,  $\beta = v/c$ , and  $\hat{\alpha}_z$  is the Dirac matrix in the  $z$  direction. The electron-projectile distance measured in the projectile system,  $r'$ , is given by equation 2.5.  $E_i$ ,  $\psi_i$  and  $E_f$ ,  $\psi_f$  are the initial and final energies and wave-functions of the electron, respectively.

For the description of the initial and final states of the projectile electron, the relativistic hydrogen like wave-functions are used. The bound-state wave-functions can be written in the form:

$$\psi(\mathbf{r}) = \begin{pmatrix} g_\kappa(r) \cdot \chi_{\kappa\mu}(\Omega) \\ i f_\kappa(r) \cdot \chi_{-\kappa\mu}(\Omega) \end{pmatrix}, \quad (2.12)$$

where  $g_\kappa(r)$  and  $f_\kappa(r)$  are real radial functions, whereas the  $\chi_{\kappa\mu}(\Omega)$  are the normalized spin-angular functions [18]. The Dirac angular momentum quantum number  $\kappa = \pm(j + 1/2)$  is a nonzero integer which can be positive or negative and  $\mu$  is the magnetic quantum number. In equation 2.11, the last integral represents the transition matrix element  $M_{fi}(b, t)$  which can be expressed by the bracket notation for the space integral as

$$M_{fi}(b, t) = \langle f | \frac{1 - \beta\alpha_z}{r'} | i \rangle. \quad (2.13)$$

For the description of the impact parameter dependent ionization, a semi-classical approximation (SCA) originally developed by Bang and Hansteen [33, 34] is adopted. In the SCA, the ionization probability  $P^{ion}(b)$  is determined within first order perturbation theory. Based on the SCA, Trautmann and Rösel developed a model to calculate the ionization cross section [35]. The model neglects the magnetic part of the full interaction potential, and assumes non-relativistic collision kinematics. However, exact Dirac wave functions are used.

The magnetic contribution to the total ionization amplitude arises if one considers a relativistic collision where the perturbing spherically-symmetrical Coulomb potential is Lorentz transformed to the laboratory frame of the ionized atom. This transformation leads to the extension of the potential in the transverse direction and shrinkage in the longitudinal direction (*see figure 2.3*), yielding the Liénard -Wiechert potential [28]. Within this picture, the magnetic part of the interaction amplitude is added incoherently. This correction leads to an increase of the total ionization cross sections with increasing  $\beta$  values. It should be noted, that the model proposed by Anholt *et al.* [36], where electric and magnetic contributions are added incoherently, generally yields a fairly good agreement with the existing experimental cross section data [25, 37], with one interesting exception at ultra-relativistic energies [38].

## 2.2.2 The Simultaneous Excitation and Ionization process

The consequence of the independent particle approximation is that, the many-body problem can be reduced to a single-electron problem. In this approach the probability for a simultaneous ionization and excitation of the ground state electrons into the final  $nlj$  state of the projectile,  $P_{nlj}^{ion-exc}$ , can be expressed as an uncorrelated product of single-electron probabilities:

$$P_{nlj}^{ion-exc}(b) \approx P^{ion}(b)P_{nlj}^{exc}(b) \quad (2.14)$$

Here,  $P^{ion}(b)$  is the single-electron ionization probability for collision with an impact parameter  $\mathbf{b}$  and  $P_{nlj}^{exc}$  is the single-electron excitation probability into the state characterized by quantum numbers  $nlj$ .

The total cross section for the process of ionization and excitation into the  $nlj$ -state of the projectile is then given by:

$$\sigma_{nlj}^{ion-exc} = \int_0^\infty 2\pi b P_{nlj}^{ion-exc}(b) db. \quad (2.15)$$

Using the equations 2.14 and 2.15, the cross section for the simultaneous ionization and excitation processes can be derived.

## 2.2.3 Calculated Probabilities in the Independent Particle Model

The curves representing calculated probabilities of individual single-electron processes for  $220 \text{ MeV/u } U^{91+}$  projectile are shown in figure 2.4a. In the case of excitation, only probabilities for the population of the  $2s_{1/2}$ ,  $2p_{1/2}$ , and  $2p_{3/2}$  states summed over the final magnetic sub-states are presented. The probability for  $K$ -shell ionization of  $U^{91+}$  calculated within SCA approximation is also shown. One can observe that the excitation probability into the  $2s_{1/2}$  state reaches its maximum at much smaller impact parameters than that for the  $2p$  states. The main reason for this behavior is due to the relativistic radial contraction of  $s$  orbital occurring for high- $Z$  ions. According to the equation 2.14, the reduced probabilities for the simultaneous excitation and ionization



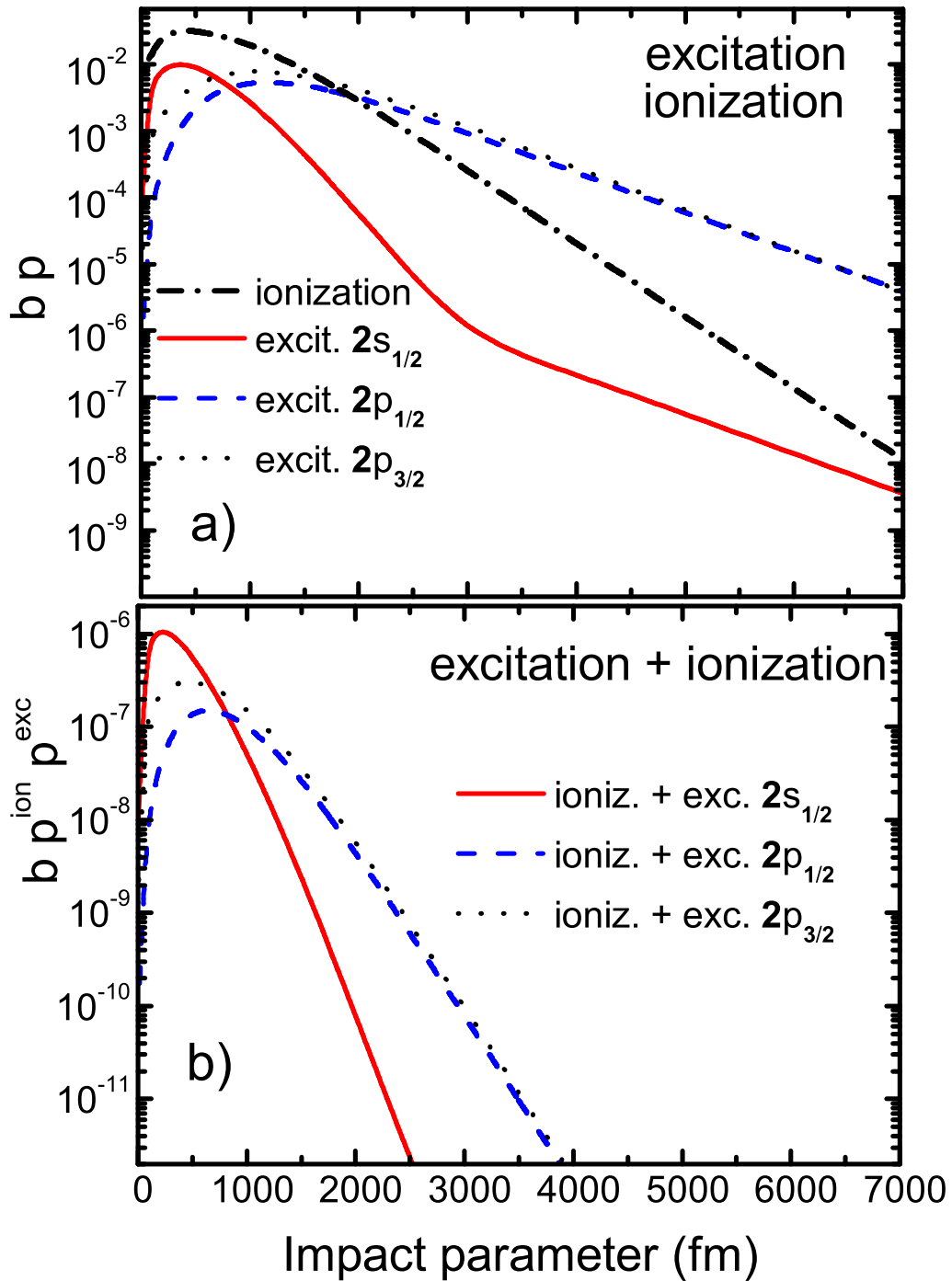


Figure 2.4: Calculated probabilities for excitation and ionization in hydrogen like uranium ions and excitation-ionization processes helium like uranium ions, plotted versus collision impact parameter [39]. For further explanation see the text.

process in He-like uranium ions are plotted in figure 2.4b. Due to its multiplicative nature, the impact parameter dependence of excitation plus ionization exhibits a prominent suppression of probabilities at large impact parameters as compared to the single-electron processes. Hence, the cross sections for the simultaneous excitation plus ionization can be regarded as equivalent to the impact parameter differential measurement in the sense, that they probe the individual single-electron processes at small impact parameter  $b$ . The calculated cross section ratios  $\frac{\sigma^{exc}(Ly_{\alpha 1})}{\sigma^{exc}(Ly_{\alpha 2})}$  are considerably different for single excitation and excitation accompanied by  $K$ -shell ionization, and are equal to 0.84 and 0.42 [39], respectively.

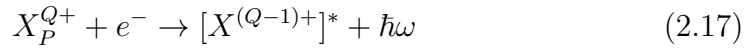
## 2.3 Electron Capture Studies

### 2.3.1 Radiative recombination (RR)

Another basic process in atomic collision physics is the charge transfer between the collision partners (target and projectile). The simplest transfer mechanism is the radiative recombination RR, in which a free electron is directly captured by the projectile, denoted by  $X_P^{Q+}$ , and the excess energy and momentum are carried away by a photon:



for electron capture into the ground state, and



for electron capture into excited states.

After the capture into an excited state there will be further radiative transitions within the ion until the electron has reached the lowest accessible energy level. Energy conservation requires that

$$\hbar\omega = E_{KIN} + |E_b|, \quad (2.18)$$

where  $E_{KIN}$  is the kinetic energy of a free electron captured into a bound atomic state  $n$  with binding energy  $E_b$  and  $\hbar\omega$  is the energy of simultaneous

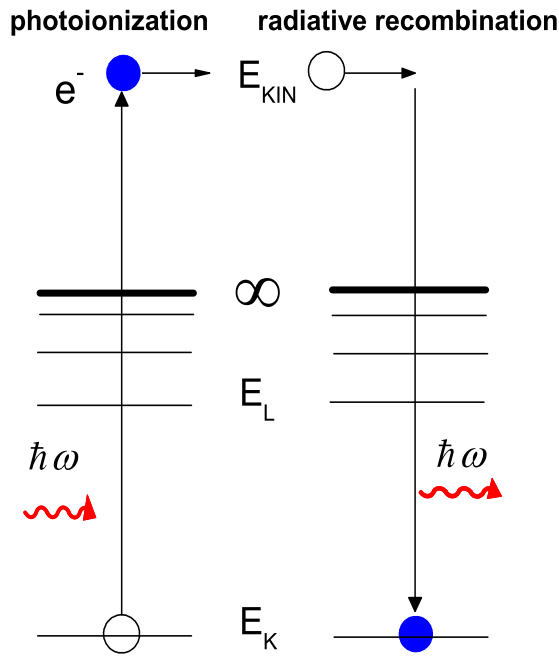


Figure 2.5: Radiative recombination can be viewed as time-reversed photoionization: an electron is captured into a bound state of the ion with simultaneous emission of a photon.

emitted photon. The process is the time reversal of photoionization in which a photon with an energy  $\hbar\omega$  hits the projectile atom and ejects an electron [18](see figure 2.5).

By the principle of detailed balance [40], the differential cross section of RR is related to the photoelectric effect and can be written as [41]:

$$\frac{d^2\sigma_{RR}(E', \theta')}{dE'd\Omega'} = (2J_n + 1) \frac{(\gamma - 1 + E_b/m_e c^2)^2}{\gamma^2 - 1} \frac{d^2\sigma_{ph}(E', \theta')}{dE'd\Omega'}. \quad (2.19)$$

Since RR takes place in a moving frame, the primed quantities (energy and angles) should be distinguished from the unprimed laboratory quantities. The multiplying factor  $(2J_n + 1)$  takes into account all bound states  $n$ .

### 2.3.2 Radiative versus non-radiative electron capture

In the case that the captured electron was previously bound in an atom, the transferred electron can be considered as "quasi-free". Therefore, the electrons are captured from the bound states of the target into the bound state of the projectile.

For the collisions of highly-charged ions with light target atoms, capture of quasi-free electron target atoms can be divided in two main groups of mechanisms: the radiative electron capture REC, and the non-radiative electron capture NRC.

REC can be described as a recombination process within the impulse approximation, taking into account the momentum distribution of the electrons in the target atom. The impulse approximation can be applied as long as:

$$\frac{v_T}{v} = \sqrt{\frac{E_b^T}{E_{KIN}}} \ll 1 \quad (2.20)$$

where  $v_T$  is the orbital velocity of the target electron,  $v$  is the velocity of the electron,  $E_b^T$  the electron binding energy in the target and  $E_{KIN}$  the kinetic energy of electron.

If an electron is captured directly from the target to the K-shell of the projectile by a simultaneous emission of photon, this process is called "K-REC" and the capture into L-shell is called "L-REC". The schematic representation of the processes is shown in figure 2.6.

In relativistic form, the energy of the emitted photon is given by:

$$\hbar\omega_{REC} = m_e c^2 (\gamma - 1) + E_f - \gamma E_i + \beta \gamma c \vec{p}_i, \quad (2.21)$$

where  $m_e c^2 (\gamma - 1) = E_{KIN}$  refers to the kinetic energy of the electron,  $E_i$  and  $E_f$  are the initial and final binding energy of the electron in the target and projectile, respectively. The last term represents the momentum distribution of the target electrons (Compton profile) which defines the characteristic width of the energy distribution of the REC photons [41].

In the non-radiative electron capture NRC, the energy difference between the initial bound state of the electron in the target and the final bound state

in the projectile is converted into kinetic energy of the collision partners, for which:

$$E_f \approx T_K + E_i. \quad (2.22)$$

In the non-relativistic collision domain, the electron transfer process is entirely governed by nonradiative electron capture (NRC). From the historically first theory for NRC, the Oppenheimer-Brinkman-Kramers approach (OBK) [42], it is known that this process has a dramatic velocity dependence which approaches  $v^{-12}$  or  $E^{-6}$ . Also, its cross section follows a strong dependence on the projectile and target atomic charge numbers ( $Z_P$  and  $Z_T$ ):

$$\sigma_{NRC} \propto \frac{Z_T^5 Z_P^5}{v^{12}}. \quad (2.23)$$

This rapid decrease of the cross section at high energies is mainly caused by the requirement that a given momentum component in the initial electronic wave-functions has to find its counterpart in the final momentum wave-function displaced by the momentum  $m_e v$  of an electron traveling with the speed of the projectile [28].

Although, in the ultra-relativistic limit the correct asymptotic energy dependence of  $\sigma_{NRC}$  is given by  $E^{-1}$ , this process practically plays no role at relativistic encounters ( $\beta > 0.5$ ) of heavy highly-charged ions with low- $Z$  target atoms.

Contrary, at highly energetic collisions, electron transfer is entirely dominated by REC, where the coupling between the electron and the electromagnetic field of the moving ion results in an electron capture via simultaneous emission of a photon carrying away the energy and momentum difference between the initial and final electron states. The general scaling properties of REC can be derived from the nonrelativistic dipole approximation of Stobbe (*see section 2.3.3*) and is given by:

$$\sigma_{REC} \propto \frac{Z_T Z_P^5}{v^{5/2}}. \quad (2.24)$$

The interplay between both capture processes, REC and NRC, is depicted in figure 2.7a, where the measured electron capture cross-sections for  $U^{92+}$  ions

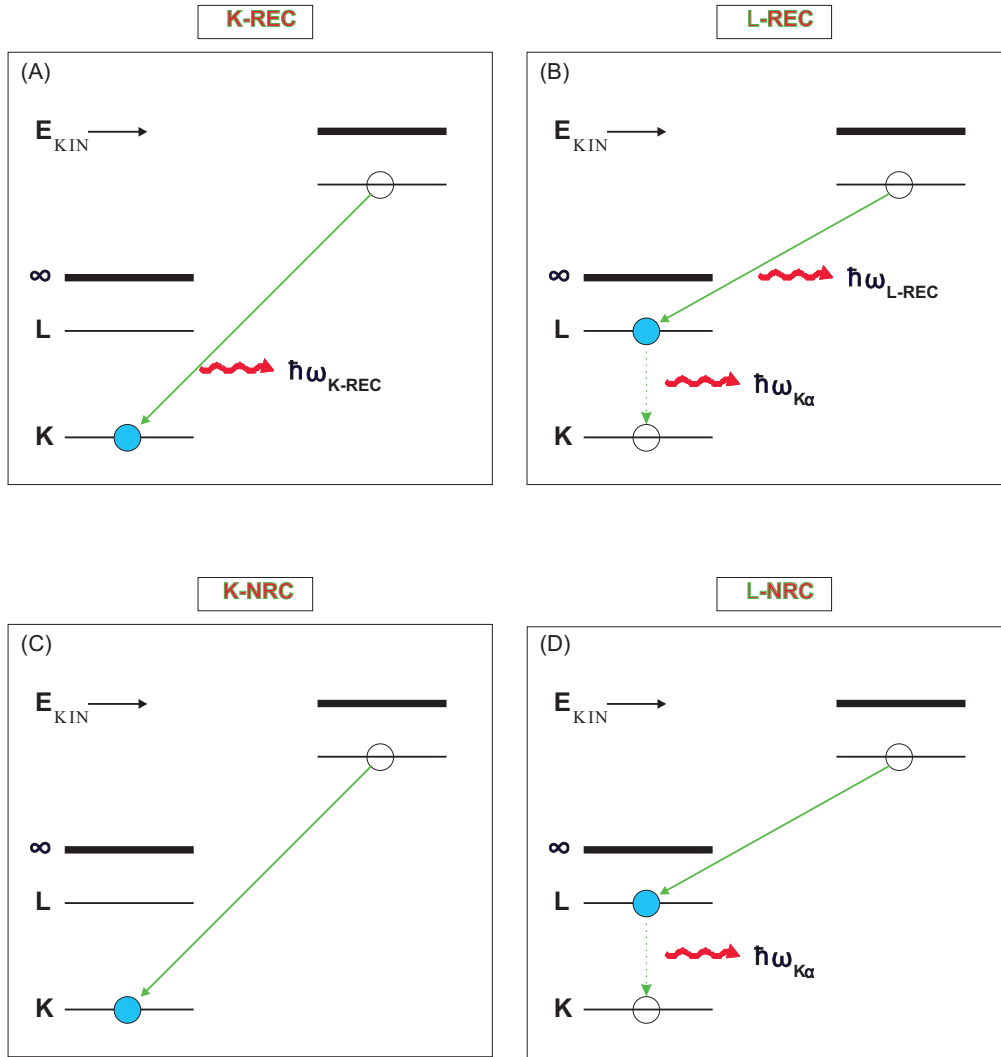


Figure 2.6: Schematic representation of the REC and NRC processes. The electron is captured from a bound state of the target atom into the K-shell of the projectile with the emission of a K-REC photon (A), or no photon emission (C). The electron capture into the L-shell is followed by the decay in the ground state resulting in a photon emission of energy  $\hbar\omega_{\text{K}\alpha}$  (B and D).

on a  $N_2$  collisions are given [43]. The experimental data are compared with a theoretical estimation (*full line*) based on the eikonal approximation [27] for NRC (*dashed line*), while REC was taken into account by using the nonrelativistic dipole approximation [44]. As seen in the figure 2.7a, an excellent agreement between the experimental results and the theoretical calculations can be stated. It can be seen from figure 2.7b, that for low- $Z$  target atoms and high projectile energy ( $300 \text{ MeV}/u$ ), the REC cross section exceeds the cross section for NRC. In this case, the electrons loosely bound in low- $Z$  target atoms are more likely to be captured with photon emission than without. From this point of view, the REC mechanism deserves particular attention.

In order to describe the important relativistic effects that appear in the case of collisions in high- $Z$  systems, an exact theoretical treatment is required. Usually the photoionization deals with many electron systems, which are complicated to be described theoretically. On the Contrary, REC can be studied on simple and clean atomic systems, i.e, capture into bare ions. The theoretical analysis of the decay dynamics of excited states and the x-ray production is useful in the understanding of the population mechanisms in the case of H-like relativistic heavy ions in collision with light gaseous targets. The case of H-like uranium ions colliding with  $N_2$  target will be discussed in detail in section 2.4. Emphasize has been put particularly on the formation of the  $^3P_0$  and  $^3P_2$  levels by using electron capture into hydrogen like uranium ions.

Both the total and the angle-differential REC cross sections can be deduced from the equations for the RR (*see eqn. 2.19*). This cross section has to be multiplied by the number of quasi-free target electrons by using the impulse approximation (*see eqn. 2.20*). However, it should be stressed that the RR angular distribution of the photons in the laboratory system can be considered valid only partially for the REC process. The binding of the electrons in the target will introduce a deviation from the  $\sin^2\theta$ -distribution at small forward and backward angles. Therefore, the deviation from the symmetric  $\sin^2\theta$ -distribution provide a direct study of the relativistic corrections imposed by the presence of the high nuclear charge. A non-zero cross section at forward and backward angles seems to be the unique signature of spin-flip contributions. In the following, the theoretical models are presented.

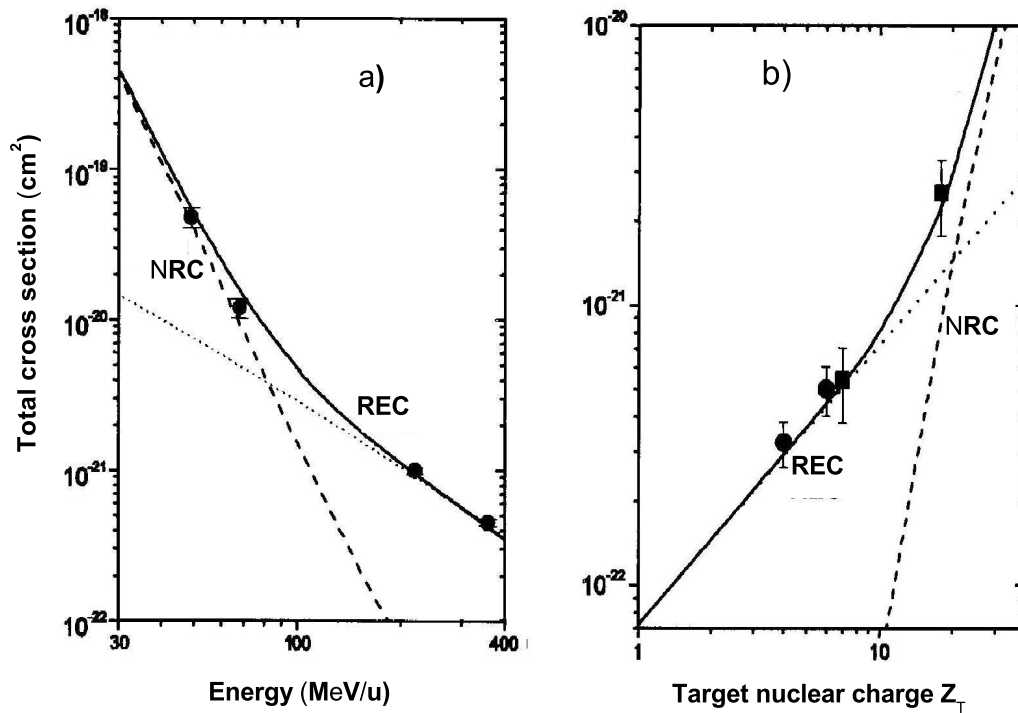


Figure 2.7: (a) The total electron capture cross section dependence on projectile energy for bare uranium ions on  $N_2$  [43]. (b) The total electron capture cross section dependence on target nuclear charge  $Z_T$  for bare uranium ions at  $300 \text{ MeV}/u$  colliding with gaseous targets  $N_2$  and  $Ar$  (solid squares) and with solid targets  $Be$  and  $C$  (solid circles) [27, 43]. The dashed line represents the eikonal approach [27] for the NRC process. The dotted line shows the prediction obtained for REC within the dipole approximation. The solid line represents the sum of both predictions.



### 2.3.3 Non-relativistic dipole approximations versus exact relativistic treatment of REC capture

By considering the assumptions of  $\hbar\omega \ll m_e c^2$  and  $\alpha Z_P \ll 1$ , where  $\alpha$  is the fine-structure constant, it is justified to adopt the non-relativistic dipole approximation for calculating the cross section for the photoelectric effect or for radiative recombination. Within this framework, the general result for radiative recombination into the  $1s$  state is given by the Stobbe formula:

$$\sigma_{RR}^{Stobbe} = 9.165 \times 10^{-21} \left( \frac{\nu^3}{1 + \nu^2} \right)^2 \cdot \frac{e^{-4\nu \arctan(1/\nu)}}{1 - e^{-2\pi\nu}} \text{ cm}^2, \quad (2.25)$$

where  $\nu = e^2 Z_P / \hbar v$  is the Sommerfeld parameter. The Stobbe cross section proves to be quite useful to estimate REC into the K-shell up to projectile energies of a few hundred  $MeV/u$ , corresponding to electron kinetic energies  $(\gamma - 1)m_e c^2$  well below the electron rest energy.

Within Stobbe's non-relativistic dipole approximation, the differential cross section is given by:

$$\frac{d\sigma_{RR}^{Stobbe}}{d\Omega} = \sigma_{RR}^{Stobbe} \frac{3}{8\pi} \sin^2\theta, \quad (2.26)$$

where  $\theta$  denotes the angle between the directions of incoming electron and the emitted photon in the laboratory system.

A relativistic theory for REC has been developed in the recent years [45, 46, 47, 48]. The exact relativistic differential photoelectric cross section was calculated for the projectile in the emitter system. From this calculation the corresponding differential cross section for the RR process was derived by the principle of detailed balance. From equation 2.19, one obtains

$$\frac{d\sigma_{RR}(\theta')}{d\Omega'} \propto \frac{\sin^2\theta'}{(1 + \beta \cos\theta')^4}, \quad (2.27)$$

where the maximum of the cross section distribution is shifted towards backward angles. Finally, one has to transform all primed quantities into the laboratory system (unprimed quantities) by applying Lorentz transformations (see figure 2.8):

$$\cos\theta' = \frac{\cos\theta - \beta}{1 - \beta \cos\theta} \quad (2.28)$$

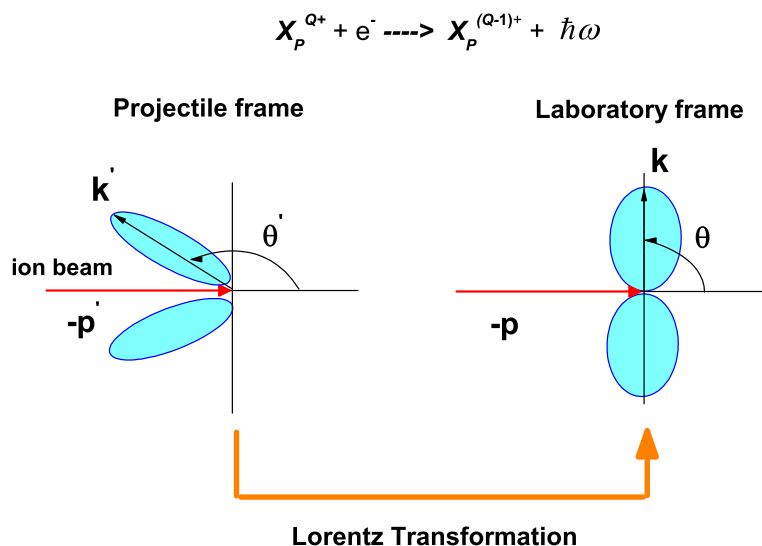


Figure 2.8: Schematic illustration of the photon angular distribution for REC in the projectile and laboratory frame.

As a result of this transformation, the desired differential cross section for the REC becomes

$$\frac{d\sigma_{REC}(\theta)}{d\Omega} = \frac{1}{\gamma^2(1 - \beta\cos\theta)^2} \frac{d\sigma_{REC}(\theta')}{d\Omega'}. \quad (2.29)$$

In figure 2.9, the calculated differential K-REC cross section for bare uranium ions at an incident energy of  $220 \text{ MeV}/u$  is presented. The result of the fully relativistic calculation (*see full line*) is compared with the non-relativistic angular distribution given by equation 2.26. According to the relativistic description, the differential cross section for K-REC shows a pronounced deviation from the symmetry around  $90^\circ$ , the maximum of the distribution being markedly shifted into the forward direction. As discussed in detail by Ichihara [49], this behavior is essentially associated with the occurrence of magnetic (spin-flip) transitions which are not considered by a non-relativistic theory. The term "spin-flip" means that the spin projection of the captured electron in the final state is opposite to the spin projection of the initially free electron, both projections being defined with respect to the electron's direction of motion. The exact theoretical angular distribution as function of the pro-

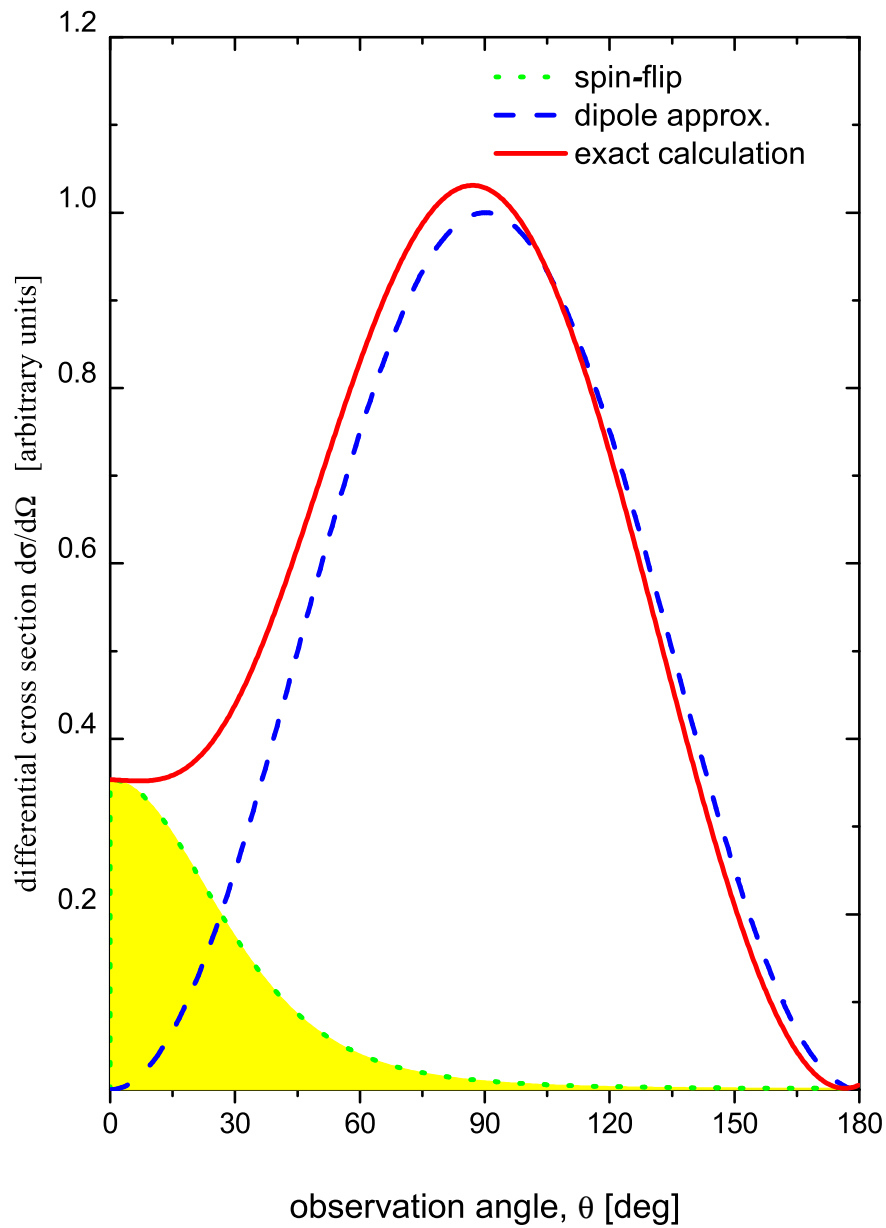
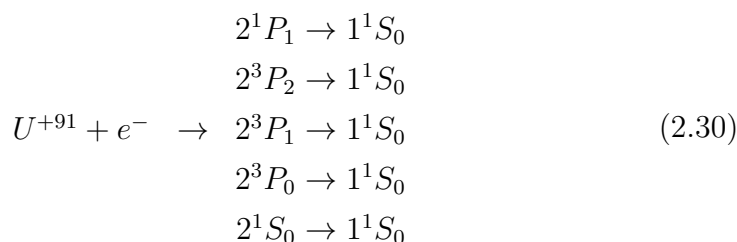


Figure 2.9: Angle-differential REC cross sections for electron capture into the K-shell of uranium ions at  $220 \text{ MeV}/u$ . The solid line refers to complete relativistic calculations and shaded area to the spin-flip contributions. The dashed line represents the non-relativistic theory for dipole approximation [48].

jectile energy and nuclear charge number has been presented in detail in Ref. [41]. At small values of  $Z_P$ , the angular distribution is practically a pure  $\sin^2\theta$ -distribution at all energies considered.

## 2.4 Alignment of the excited ion states populated via REC

After the radiative electron capture REC into excited states of heavy ions, a radiative transition to the ground state will also occur. By REC in the excited projectile states, one has the possibility to study the population mechanism on the magnetic subshells in few-electron highly charged ions (*see figure 2.10*). An electron could be captured to the  $1s$  state of the uranium ion via an L-shell intermediate state. In the case of the hydrogen like uranium ions the process can proceed through the following steps:



In the single-electron case, the  $2p_{3/2}$  state decays to  $1s_{1/2}$  mainly by the  $E1$  transition. In the two-electron case, the system of  $2p_{3/2}$  and  $1s_{1/2}$  electrons forms  $2P_{1,2}$  states which provides the  $K_{\alpha 1}$  transition. While the system of  $2p_{1/2}$  and  $1s_{1/2}$  electrons forms  $2P_{0,1}$  states providing the  $K_{\alpha 2}$  line.

Information on the population of magnetic sub-states can be obtained by the study of angular distributions of the emitted photons. The angular distribution of the photons in the emitter frame is related to the alignment parameter by [49, 50]

$$W(\theta) = A_0 + A_2 P_2(\cos\theta') \propto 1 + \beta_{20} \left(1 - \frac{3}{2} \sin^2\theta'\right), \tag{2.31}$$

where  $\theta'$  is the angle between the direction of the de-excitation photon and the beam direction while  $P_2(\cos\theta')$  denotes the second-order Legendre polynomial. The well known expression 2.31 takes into account only the dominant

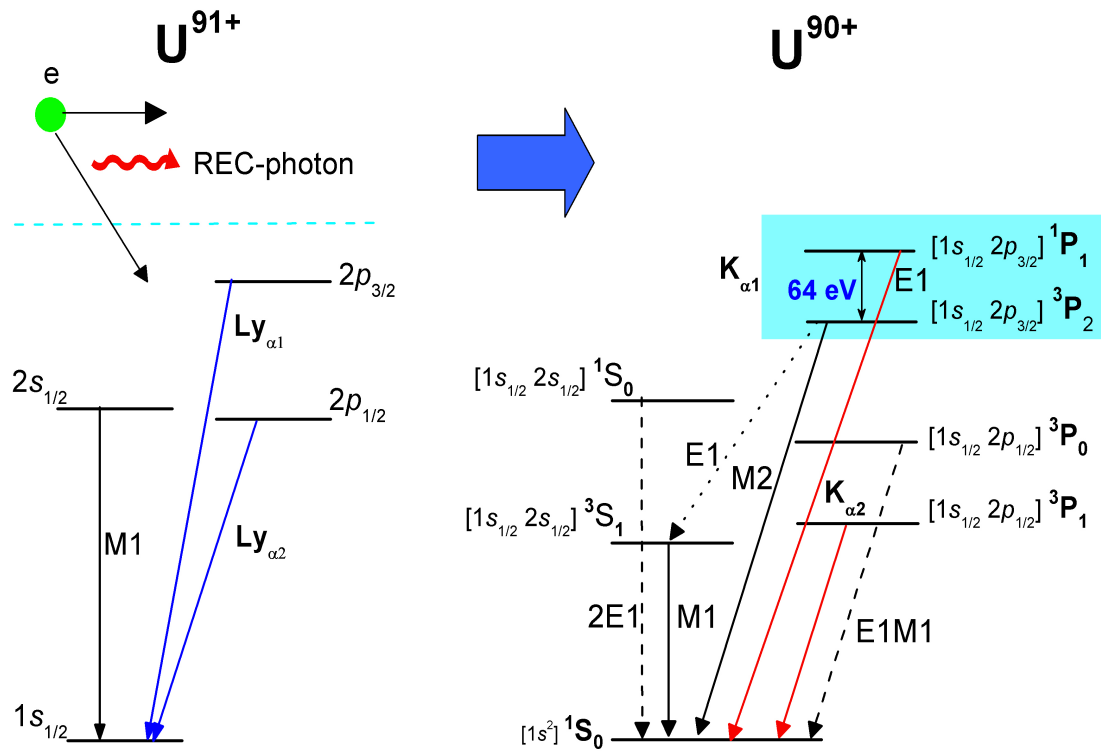


Figure 2.10: Level diagram for H- and He-like U. Multipolarities for the most probable decay modes are indicated by solid arrows, weaker decay modes are shown as dashed arrows.

electric dipole (E1) term whereas the weaker magnetic quadrupole decay (M2) is neglected. As seen from equation 2.31, the angular distribution is determined by the so-called *anisotropy* coefficient  $\beta_{20} = \alpha A_{20}$ , while the coefficient  $\alpha$  depends only on the total angular momenta of the initial and final ionic states, respectively. For the case of the  $2p_{3/2} \rightarrow 1s_{1/2}$  transition,  $\alpha = 1/2$  [50].

The population of magnetic sublevels is likely to deviate from a statistical distribution. In such cases the levels are aligned, thereby the pairs of atomic sublevels with the same magnetic quantum number (but with opposite signs) will be necessary equally populated. Here, it is assumed that neither the ions nor the the target atoms are polarized in ion-atom collisions. Consequently, the state of the ion is axially symmetric about  $z$ . This restricts the anisotropy parameters  $A_{k\kappa}$  ( $\kappa = -k + \dots + k$ ) of the state to  $A_{k0}$ , where  $k$  can take only even values 2, 4, ...,  $2J-1$ . It follows that only states with  $J \geq 3/2$  are aligned.

The alignment of an atomic level is commonly described in terms of one or several parameters  $A_{k\kappa}$  which are related to the the population cross sections  $\sigma(\mu_n)$  of the various sublevels  $\mu_n$ . For example, for  $J = 3/2$  the alignment parameter can be expressed as [50, 51]:

$$A_{20} = \frac{\sigma(\frac{3}{2}, \pm\frac{3}{2}) - \sigma(\frac{3}{2}, \pm\frac{1}{2})}{\sigma(\frac{3}{2}, \pm\frac{3}{2}) + \sigma(\frac{3}{2}, \pm\frac{1}{2})}, \quad (2.32)$$

where  $\sigma(2p_{3/2}, \mu_n)$  describes the the population of substate  $\mu_n$  of the  $2p_{3/2}$  level.

For the  $2p_{3/2} \rightarrow 1s_{1/2}$  transition, after transformation to the laboratory frame, the differential  $Ly\alpha 1$  cross section has the general form [52]

$$\frac{d\sigma_{Ly\alpha 1}(\theta)}{d\Omega_{lab}} \propto \frac{1}{\gamma^2(1 - \beta\cos\theta)^2} \left[ 1 + \beta_{20} \left( 1 - \frac{3}{2} \frac{\sin^2\theta}{\gamma^2(1 - \beta\cos\theta)^2} \right) \right]. \quad (2.33)$$

Note that due to the Lorentz transformation to the laboratory system, the maximum of the distribution is located at a forward angle of  $\cos\theta_{lab} = \beta$ . The equation 2.33 proves that the  $Ly_{\alpha 1}$  is strongly an anisotropy radiation.

For helium like uranium ions (*see figure 2.10*) as produced by the radiative electron capture of initially hydrogen like ions, most recent studies have paid attention to study the angular distributions of  $K_{\alpha 1}$  which has two compo-

nents  $^1P_1$  and  $^3P_2$  states [20]. From equation 2.31, one can obtain the angular distributions of the  $J_f = 1 \rightarrow J_0 = 0$ :

$$W_{E1}(\theta) \propto \left(1 + \frac{1}{\sqrt{2}}A_{20}(\alpha_f J_f = 1)P_2(\cos\theta)\right), \quad (2.34)$$

and  $(J_f = 2) \rightarrow (J_0 = 0)$  transition:

$$W_{M2}(\theta) \propto \left(1 - \sqrt{\frac{5}{14}}A_{20}(\alpha_f J_f = 2)P_2(\cos\theta)\right). \quad (2.35)$$

The knowledge of the many-electron alignment parameters is required for studying of the angular distribution. Theoretically, this study has been done by Surzhykov and Fritzsche [53]. By using the independent particle model IPM [54], the alignment parameters could be expressed in terms of the H-like alignment parameter  $A_{20}(2p_{3/2})$ :

$$A_{20}(J_f = 1) = \frac{1}{\sqrt{2}}A_{20}(2p_{3/2}), \quad (2.36)$$

and

$$A_{20}(J_f = 2) = \sqrt{\frac{7}{10}}A_{20}(2p_{3/2}). \quad (2.37)$$

The results of the theoretical calculations of the alignment parameters for  $2p_{3/2}$  state of hydrogen like and the  $^1P_1$ ,  $^3P_2$  states of helium like ions are presented in Ref. [55].

Figure 2.11 represents the shape of the angular distributions of the  $K_{\alpha 1}$  decay, indicating an almost isotropic behavior. Recently, it has been found that such an isotropy results from the mutual cancelation of the angular distributions of the strongly anisotropic (electric dipole and magnetic quadrupole) transitions, both of which contribute to the  $K_{\alpha 1}$  radiation [48, 56].

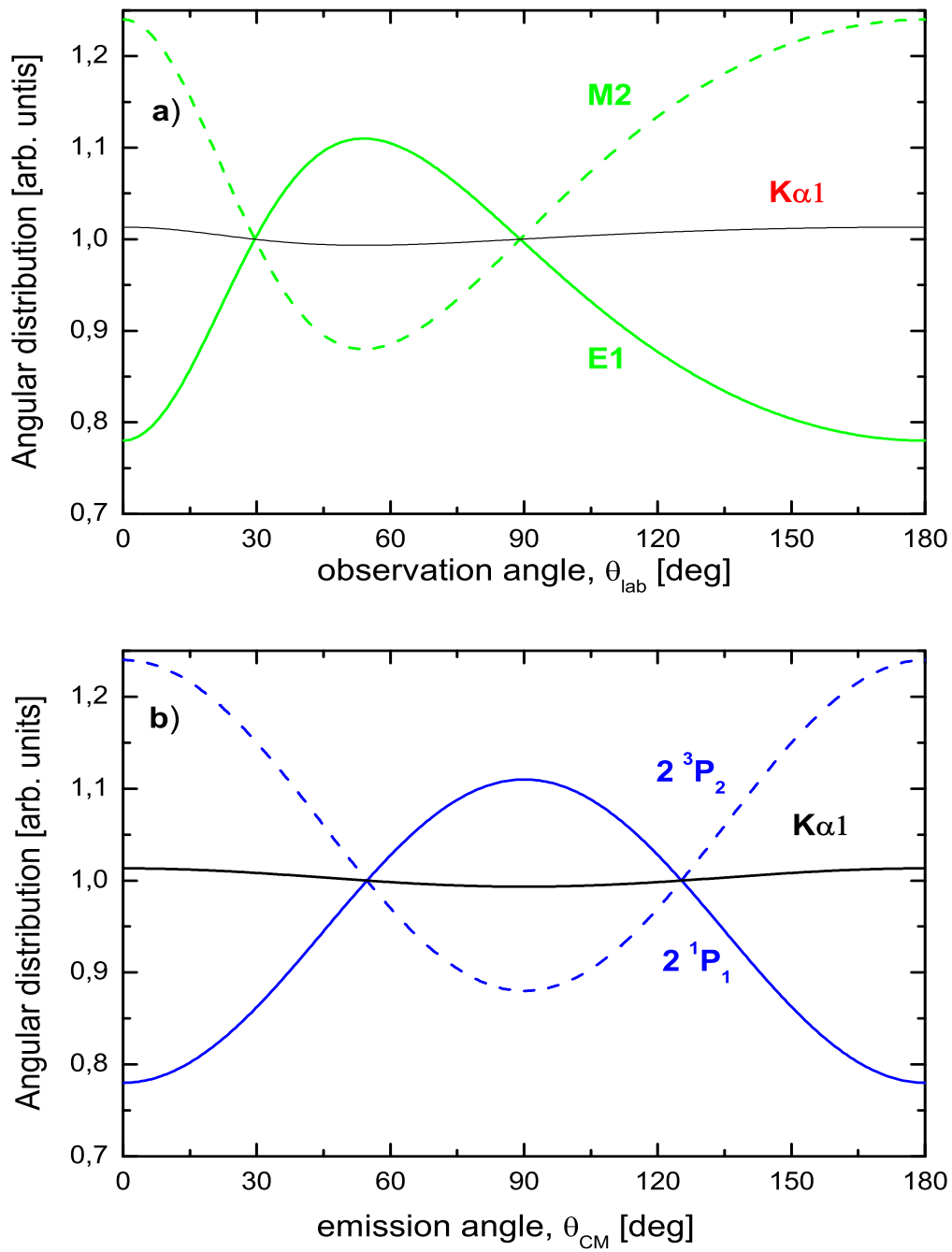


Figure 2.11: The angular distribution of the  $K\alpha_1$  decay in (a) the laboratory and (b) the emitter systems, for initially H-like uranium ions at 220 MeV/u. Additionally, the angular distributions for the electric and magnetic components of the decay are displayed [55].



# Chapter 3

## The Experiment

The measurements presented in this work have been carried out using the internal gas-jet target of the experimental storage ring ESR at GSI. The x-ray emitted during the collision of  $220 \text{ MeV}/u$   $U^{90+}$  ions with  $Xe$  atoms were detected at different observation angles in coincidence with up- and down-charged projectile ions,  $U^{91+}$  and  $U^{90+}$ .

In the following, the production of highly-charged ion beams at the GSI facility, the ESR, the target environment, the detection system and the data acquisition procedure will be discussed.

### 3.1 The production of highly-charged heavy ions

The production of highly-charged ion beams is a difficult task, requiring successive ion-atom collisions at a center-of-mass energy greater than the binding energy of the electrons to be removed. For the case of uranium, the heaviest stable atom, the K-shell binding energy amounts to  $130 \text{ keV}$ . Thus, in order to remove the K-shell electron, at least this energy must be transferred in the collision. This can be accomplished with a relativistic heavy-ion beam hitting a stationary target.

At the GSI accelerator facility, the ion beams of all stable elements across the periodic table, up to uranium, are delivered to the the UNiVersal Linear ACcelerator (UNILAC) by three different injectors equipped with three dif-

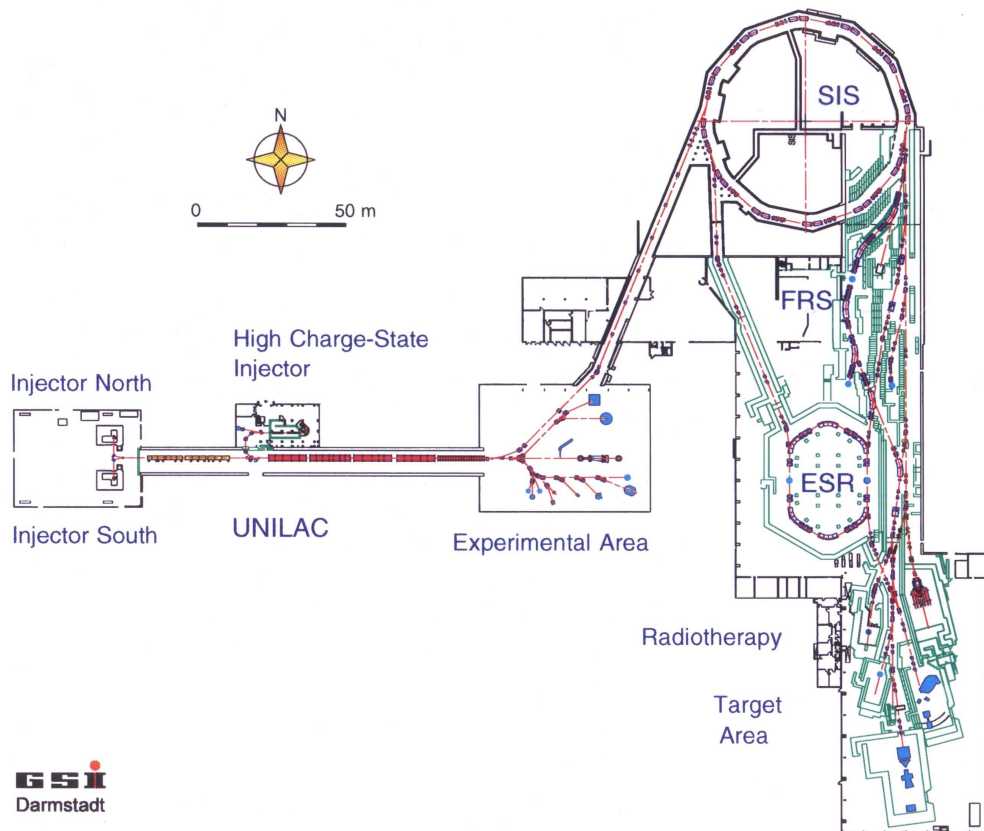


Figure 3.1: Layout of the accelerator facility and experimental areas at GSI.

ferent ion sources: the standard injector with a Penning ion source, the high current injector with a MEVVA ion source [57, 58], and the high-charge state injector. For details about ion sources available at GSI see [59, 60]. The layout of the accelerator facility and experimental areas at GSI are displayed in figure 3.1.

For the production of the H- and He-like uranium ions used in the experiment described in this work, the whole GSI accelerator chain was used. For that, Low-charge uranium ions ( $U^{4+}$ ) delivered by the ion sources are first pre-accelerated in the UNILAC which consists of three main parts: the 36  $MHz$  high-current  $RFQ/IH$ -injector, a  $N_2$  gas stripper where uranium ions with maximum charge state 28+ can be produced at the energy of 1.4  $MeV/u$  and finally, a 108  $MHz$  radio frequency (RF) accelerator which accelerates the ion beam up to 11.4  $MeV/u$ . After passing through a foil-stripper, ions with charge state 73+ are selected and injected into the SIS. The ions either are shot into the SIS over one single revolution (single-turn injection), or over several revolutions (multi-turn injection). In the SIS, the ions are accelerated to the higher beam energies required for the experiments. The maximum magnetic rigidity of the SIS is 18  $Tm$  and thus, the maximum energy that can be reached is limited to 2.1  $GeV/u$  for light ions and 1  $GeV/u$  for heavy ions.

Accelerated ions are subsequently extracted from the SIS and guided towards the ESR, the Fragment Separator (FRS), the different experimental areas or towards the heavy ion Cancer therapy dedicated area. The extraction from the SIS can be done in a pulsed mode (short extraction,  $\tau \sim 1 \mu s$ ) or in a semi-continuous mode (long extraction,  $\tau \sim 10 s$ ). To achieve the highest possible charge state (bare ions) an additional stripper foil, placed behind the SIS, is used.

In the ESR, highly-charged ions used for atomic physics experiments can be manipulated (decelerated and/or cooled) and stored for quite long times (*see section 3.2.1*). After being stored in the ESR, the beam can eventually be re-injected from the ESR into the SIS for further acceleration or extracted to a fixed target area for experiments (HITRAP and Cave A).

## 3.2 The Experimental Storage Ring ESR

The geometry of the ESR is arranged as a doubly mirror symmetric stretched hexagon with a design circumference of 108  $m$ , half the circumference of the SIS. It consists of six bending magnets and two long (10  $m$ ), straight sections which are provided for electron cooling and in-ring experiments around the internal gas-jet target apparatus. The beam focusing is performed by twenty quadrupole magnets arranged in four triplets and four doublets along the ring.

Figure 3.2 shows a schematic drawing of the ESR and its major components: the electron cooler device, the internal gas-jet target, the radio frequency cavities (*rf-cavities*) and the interaction chamber. The maximum magnetic rigidity of  $B\rho = 10 \text{ Tm}$  makes the ESR capable to accept fully stripped uranium ions at a maximum ion energy of 550  $\text{MeV}/u$ .

For experiments using highly-charged heavy ions the vacuum in the ESR must be at the level of  $10^{-11} \text{ mbar}$ . The vacuum quality strongly influences the life time of the ion beam in the ring.

### 3.2.1 The Electron Cooler in the ESR

Depending on the beam energy, two cooling techniques are available: stochastic cooling, for high energies and electron cooling for ions with energies below 400  $\text{MeV}/u$ .

Electron cooling is based on the Coulomb interaction of the circulating ions with the electrons in the 2.5  $m$  long electron cooler straight section [61]; it is a method for shrinking the size of the divergence and the energy spread of the stored charged-particle beams without significantly removing particles from the beam. The electrons are continuously produced in an electron gun with a heated cathode. They are accelerated electrostatically to a velocity equal to the average ion velocity, and are inflected into the straight section where both beams overlap a certain length. At the end of this section, the electrons are separated again from the ion beam. In order to conserve the electron beam diameter of  $\approx 50 \text{ mm}$  a variable longitudinal solenoidal magnetic guiding field of  $\approx 0.1 \text{ T}$  is also applied in the electron cooler [61, 62]. A schematic representation of the electron cooler in the ESR is represented in the figure 3.3

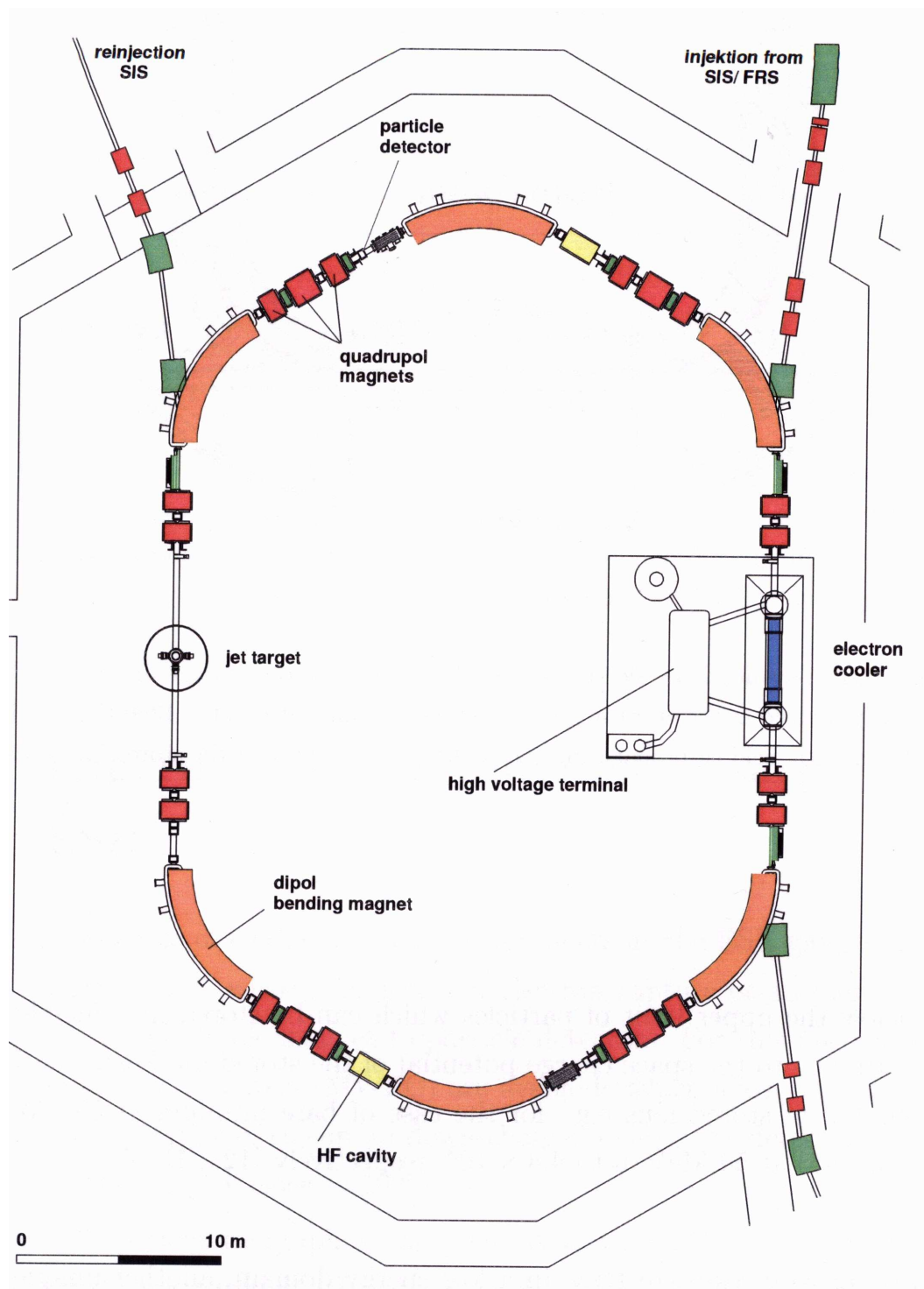


Figure 3.2: Layout of the Experimental Storage Ring (ESR) at GSI. The positions of the e-cooler and the internal jet-target are marked.

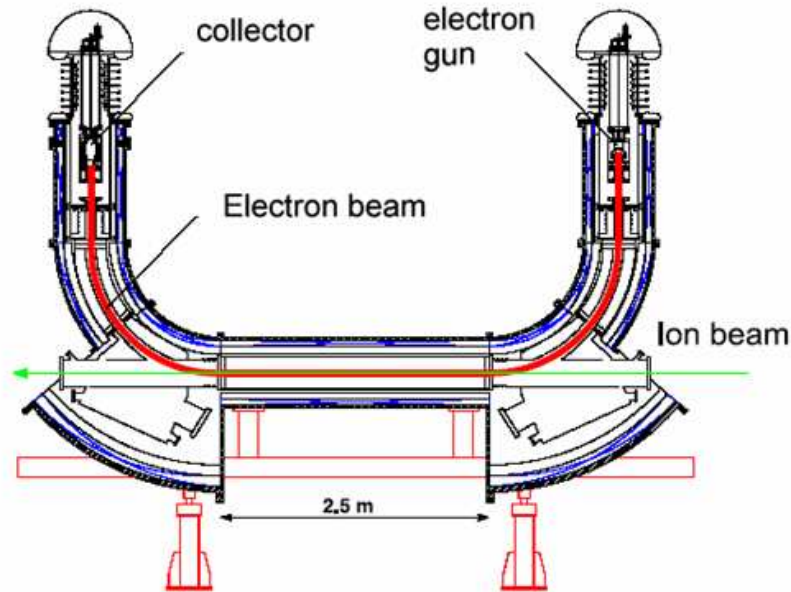


Figure 3.3: Layout of the electron cooler device used at the storage ring ESR.

and the major ESR parameters are listed in the table 3.1.

The ion beam heat is transferred to the electrons through the Coulomb interaction and consequently the ion motion is reduced. The distribution of the ion velocities become narrower in all three space dimension, which implies that the temperature of the ion beam will be decreased. The operation with high electron currents is less desirable in most experiments with highly-charged ions because the beam life time  $\tau$  drops significantly with increasing the electron current:  $\tau \propto 1/I_{cooler}$ . Therefore, a high cooling efficiency by operation of the electron cooler at low electron currents is desired in order to reduce ion beam losses [63]. For cooling of stored beams, electron currents of typically 100 mA to 300 mA are used [64]. For example, the estimated lifetime of bare uranium ions of 20 MeV/u is about 10 sec (see the table 3.2).

After the cooling, the relative momentum spread of the injected ion beam is reduced from  $\Delta p/p \approx 10^{-3}$  to about  $10^{-5}$ . A spectrum of an uncooled ion beam in comparison with a cooled one is presented in figure 3.4. The cooling technique leads to an emittance of the stored beam of less than  $0.1 \pi \text{ mm mrad}$ , and to small beam sizes with typical diameters of less than 5 mm. However,

Table 3.1: The major ESR parameters.

Ring circumference	108	<i>m</i>
Magnetic rigidity	0.5 - 10	<i>Tm</i>
Energy range	3.0 - 560 for U	<i>MeV/u</i>
Cycle length	1.5 s to hours	
Extraction	fast:~ 0.5	$\mu s$
	slow: to some 10	<i>s</i>
Beam diameter	1-5	<i>mm</i>
Beam emittance (with e-cooling)	0.1 $\pi$	<i>mm.mrad</i>
Cooling time	0.2 (for U <sup>92+</sup> )	<i>s</i>
Life time	100 (for U <sup>92+</sup> at 20 <i>MeV/u</i> )	<i>sec.</i>
Working pressure	10 <sup>-11</sup>	<i>mbar</i>
Length of the cooling section	2.5	<i>m</i>

Table 3.2: Estimated life times for different bare ions stored in the ESR.

Ion Species	Beam Energy ( <i>MeV/u</i> )	Life time	Note	Ref.
<i>U</i> <sup>92+</sup>	100	6 <i>min.</i>	with cooling	[65]
<i>U</i> <sup>92+</sup> , <i>Au</i> <sup>79+</sup>	20 - 30	10 - 30 <i>s</i>	with cooling	[66]
	20	100 <i>s</i>	without cooling	[66]
	200 - 400	few minutes	with cooling	[66]
<i>Ni</i> <sup>28+</sup> , <i>Kr</i> <sup>36+</sup> , <i>Xe</i> <sup>54+</sup>	20 - 30	1000 <i>s</i>	with cooling	[66]
	200 - 400	few hours	with cooling	[66]

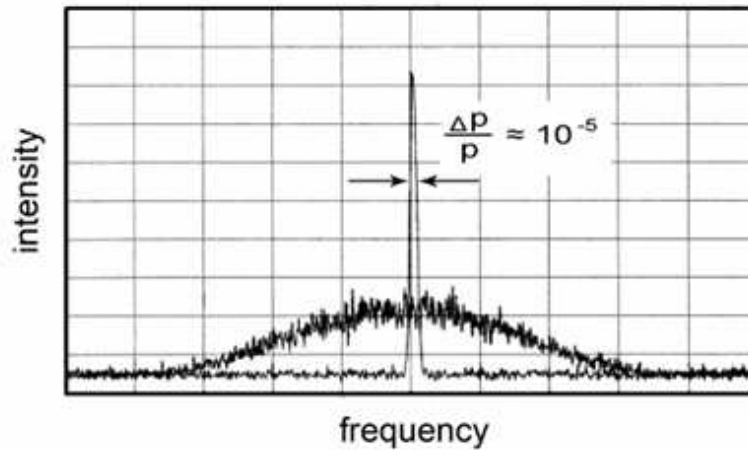


Figure 3.4: Schottky frequency spectrum for a circulating beam of  $U^{92+}$  ions at  $295 \text{ MeV}/u$ . The broad distribution refers to the non-cooled beam, measured directly after injection into the ESR. The narrow distribution reflects the momentum profile of a continuously cooled ion beam.

both the final emittance and relative momentum spread of the stored beam depend on the number of stored ions and the applied cooler current.

The effective number of stored particles per second available for experiments averaged over a time cycle of one day, has been continuously improved since 1992, from about  $10^3$  particles/sec to  $10^6$  particles/sec today [41, 67, 68]. The effective number of stored particles at the ESR over the years, is displayed in figure 3.5.

A further, unique feature of the ESR is the deceleration capability down to  $4 \text{ MeV}/u$ . This allows experimental investigations with few-electron, heavy ions in a different energy domain, far below the production energy of bare ionic species. For this purpose, the electron cooler has to be switched off and the beam must be rebunched and decelerated. At that final stage of beam handling, the electron cooler is again switched on. For the case of H- and He-like uranium ions used in the present experiment, the energy was reduced from  $360 \text{ MeV}/u$  to the required value of  $220 \text{ MeV}/u$ .



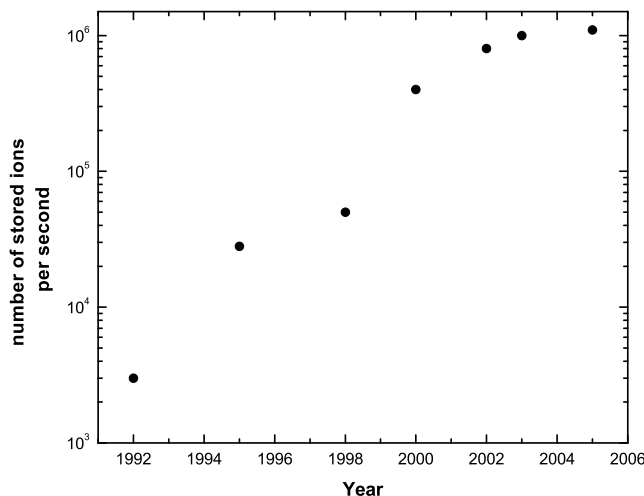


Figure 3.5: The effective number of stored particles per second available for experiments in ESR. The average over a time cycle of 1 day is displayed [41].

### 3.2.2 The Internal Gas-Jet Target of the ESR

Another experimental device in the ESR is the internal gas-jet target, which provides an important tool for a broad range of atomic as well as nuclear physics experiments.

In the interaction chamber the stored ion beam crosses a perpendicular oriented molecular or atomic gas-jet. The jet is produced by expanding the gas in vacuum through a Laval nozzle of 0.1 *mm* in diameter. The setup consists of an injection and a dump part, each separated by skimmers in four stages of a differential pumping system. A schematic picture of the gas-jet with its different stages is shown in the figure 3.6. The first stage of the injection part, with nozzle and first skimmer, is pumped by a system of roots pumps. The remaining three stages of the injection part and the four stages of the gas-jet dump are pumped by a differential pumping system of turbo-pumps. The multi-stage pumping is needed to preserve the high level vacuum in the ring ( $10^{-9} - 10^{-11}$  *mbar*) and to produce a well defined interaction region. To perform standard services without breaking the ESR vacuum, the injection part

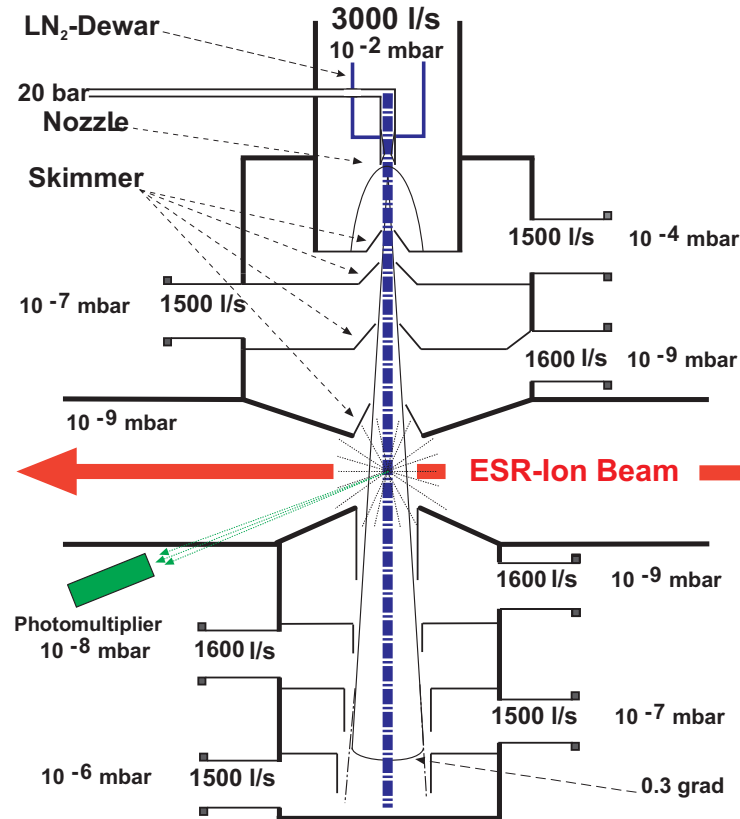


Figure 3.6: Schematic representation of the ESR internal gas-jet target [69, 70].

and the gas-jet dump can be separated from the interaction chamber by the use of two ultra-high vacuum (UHV) compatible valves. The installation of the large pumping speed at the injection part made it necessary to choose a distance between the nozzle and the interaction point of approximately  $500\text{ mm}$ . For an interaction length of  $5\text{ mm}$ , the geometric acceptance of the skimmer system is  $\approx 1\text{ mrad}$  [69, 70].

To operate the target with different gas species at optimum performance, the distance of the nozzle to the first skimmer can be 3-dimensionally adjusted via remote control. Typical distances between nozzle and the first skimmer are  $30\text{ mm}$  for light gases and  $60\text{ mm}$  for heavy gases. To optimize the overlap between the ESR-ion beam and the target, the counting rate of photons originating from the interaction region, detected by a photomultiplier in the ring, is maximized by shifting the position of the ion beam relative to the gas-jet.

### 3.3 The Experimental setup

Figure 3.7 shows the basic principle of the charge exchange experiments at the ESR gas-jet target. The primary beam of stored ions of charge state  $Q$  crosses a perpendicular oriented atomic supersonic gas beam. The outgoing projectile beam, comprising ions of different charge states, is analyzed by the first dipole magnet downstream of the jet target zone. The radius  $r$  of the trajectory of an ion moving in the magnetic field  $B$  of the dipole magnet is related to its charge state  $Q$  as:

$$r = \frac{p}{QB} \quad (3.1)$$

where  $p$  is the momentum of the ion. This leads to the result

$$\frac{\Delta r}{r} \propto \frac{\Delta Q}{Q}, \quad (3.2)$$

which implies that the trajectories for the charge exchanged projectiles,  $(Q - 1)$  and  $(Q + 1)$  are slightly deflected from the initial ion trajectory and several charge states can be detected by a position sensitive detector. Position sensitive multi-wire proportional counters (MWPC, *see section 3.3.3*), mounted horizontally left and right relative to the central beam trajectory allow to accurately determine the position of the up- and down-charged ions with a detection efficiency close to 100% [71].

#### 3.3.1 The Interaction Chamber

Surrounding the internal target area of the ESR, a special designed interaction chamber, which allows to record x-rays emitted from the beam-target interaction volume at different observation angles, is installed. The accessible angles are  $4^\circ$ ,  $35^\circ$ ,  $60^\circ$ ,  $90^\circ$ ,  $120^\circ$ , and  $150^\circ$  with respect to the beam axis. A sketch of the experimental arrangement at the present interaction chamber of the ESR gas-jet is shown in the figure 3.8. The different germanium detectors which can be mounted at these observation angles are isolated from the ultra-high vacuum environment by  $50 \mu m$  stainless steel or  $100 \mu m$  thick Beryllium windows. Except for the near  $0^\circ$  detector, each detector is equipped with a collimator of

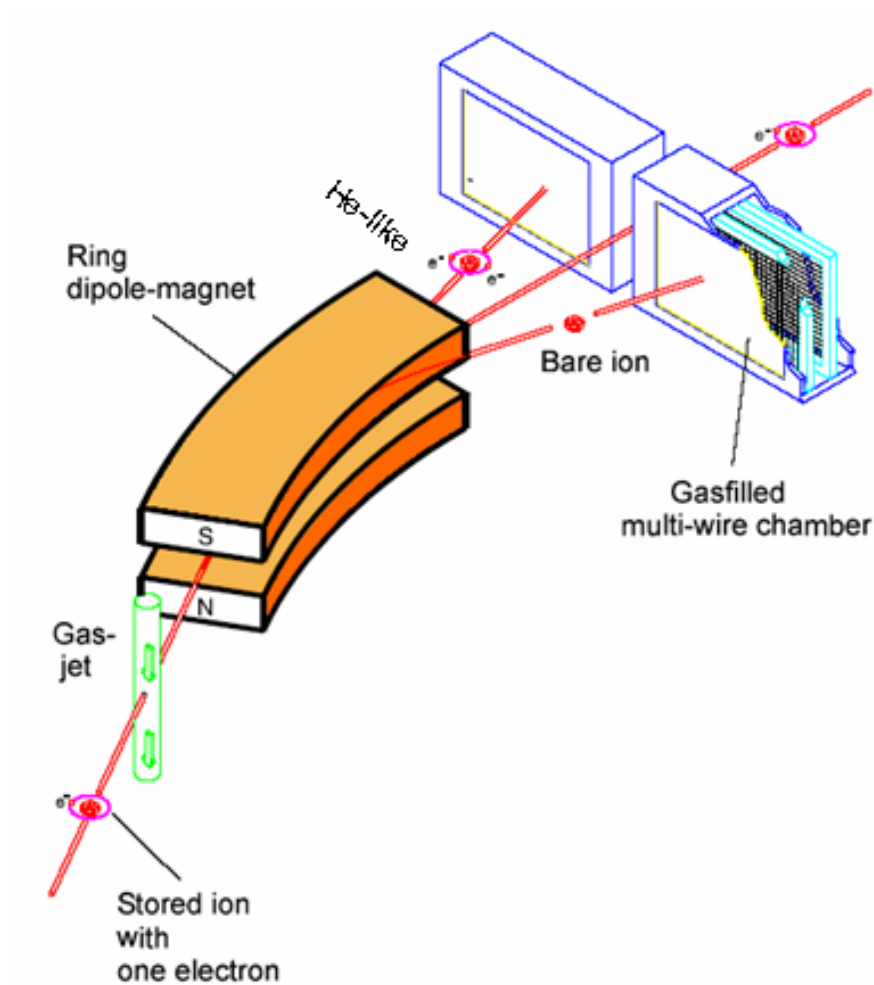


Figure 3.7: Principle of the charge exchange experiments at the internal jet target of the ESR illustrated for the case of H-like ions primary beam. Up-charged ( $Q + 1$ ) and down-charged ( $Q - 1$ ) ions are separated from the primary beam and detected by particle detectors.

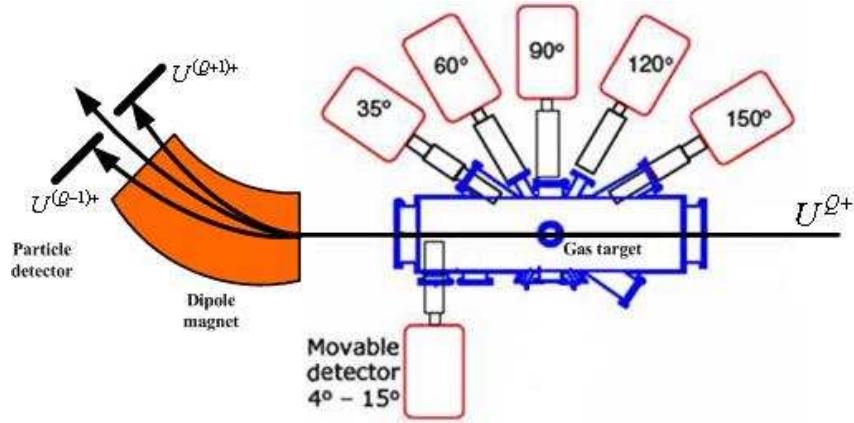


Figure 3.8: Layout of the experimental arrangement at the ESR jet-target. Photon emission is observed in coincidence with the up- or down-charged ions, detected by a particle counter placed behind the dipole magnets.

a narrow angular acceptance in order to reduce the Doppler broadening (*see chapter 4*).

### 3.3.2 The X-ray Detectors

In the present experiment, for the photons detection, different high-purity germanium detectors have been used (*see figure 3.9*). A general presentation of the detection principle of Ge-based detectors can be found in Reference [72]. A list of the used detectors and their main characteristics is given in the table 3.3. Having different crystals, the energy resolution and the detection efficiency is different from one detector to the other. This is reflected in the quality of the registered x-ray spectra. To get the best possible energy separation of the lines of interest in the x-ray spectra, the Doppler broadening was reduced by using collimators with different solid angles. On the same time, the x-ray detectors with the better energy resolution have been used for detection at higher observation angles in order to compensate for the Doppler shift.

### 3.3.3 The particle detector

During the interaction with the target atoms, the projectile ions can undergo charge exchange via ionization or capture. In the present experiment, ions with

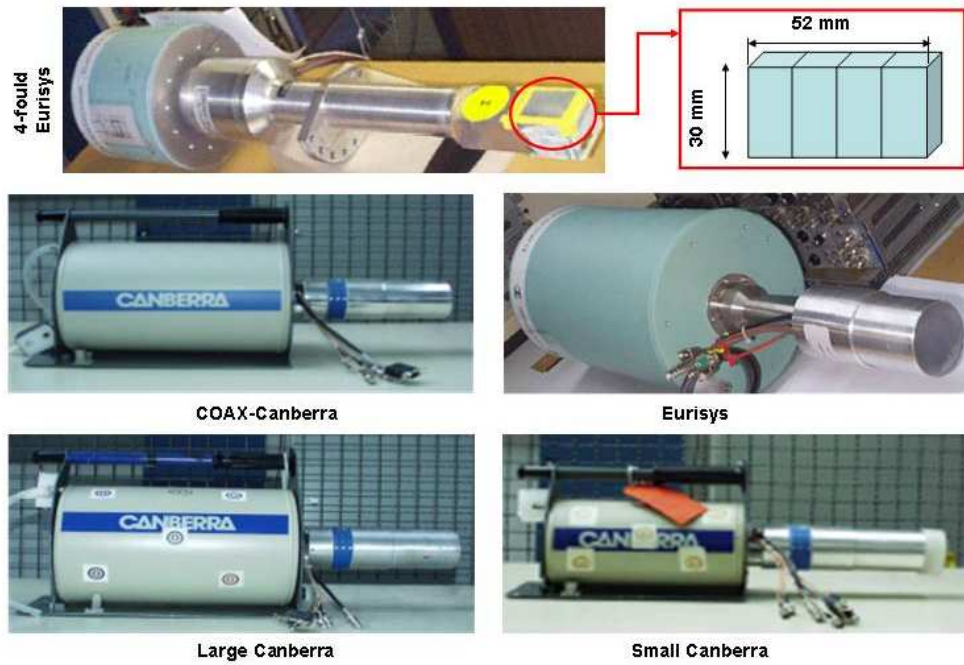


Figure 3.9: The Ge(i) detectors used in the experiment.

Table 3.3: Characteristics of the Germanium detectors used in the present experiment.

Detection Angle	0°	35°	60°	90°	120°	150°
Producer	Eurisys	Canberra	Eurisys	Canberra	Canberra	Canberra
Bias Voltage (V)	1000	3500	3000	3000	3000	3500
Polarity	positive	negative	negative	negative	negative	negative
Crystal geometry	4 stripes	circular	circular	circular	circular	circular
Crystal thickness (mm)	12.5	41	20.5	15	13	15
Crystal area (mm <sup>2</sup> )	1550	1520	2000	500	500	500
Be entrance window: thickness (μm)	175	500	300	150	150	150
Energy resolution at 60 keV (eV)	-	850	660	570	580	500
† Detection efficiency at 60 keV (%)	-	91	87	82	82	82

† for more details, see chapter 4.

charge difference  $\Delta Q = \pm 1$  have been detected with two dedicated *multi-wire proportional counters* (MWPC) placed on the internal, respective external side of the ring, behind the analyzing dipole magnet (*see figure 3.7*).

Generally, the standard MWPCs consists of a set of thin, parallel and equally spaced wires, symmetrically sandwiched between two cathode planes [73]. The first set of wire built is the anode and in the front layer is the cathode of the detector. The read-out of the signal is done by the delay-line method.

The detection efficiency of the ions is better than 99 % and the spatial resolution is about 1.9 *mm*. The particle detectors were specially designed and built in the GSI detector laboratory. The detectors are mounted in a stainless steel pocket and are separated from the ultra-high vacuum environment of the ESR by 25  $\mu\text{m}$  thick stainless steel window. Good description of their construction and development is given in Reference [71] by Klepper and Kozhuharov.

## 3.4 Signal Processing and Data Acquisition System

The detector signals are processed using standard NIM electronics. The preamplifier output (Pre-Amp) from each germanium detector was sent to two amplifiers, an "energy" amplifier (Amp) and a "timing" amplifier (TF-Amp.). The output of the energy amplifiers were routed to a peak-sensing analog-to-digital converter (ADC). The outputs of the timing amplifiers were sent to a discriminator (CF Discriminator) and then directed to the time-to-digital converter TDC. For the particle detector, only the anode signal was used for the hardware coincidence with the germanium detectors. A block diagram of the electronics used in this work is shown in figure 3.10.

Data acquisition is based on the Multi-Branch System (MBS) developed at GSI. The MBS runs under the operating system Lynx on a CAMAC processor board CVC. The system works stand alone, it reads all data from the CAMAC modules and writes them on a local tape drive or directed on the disk.

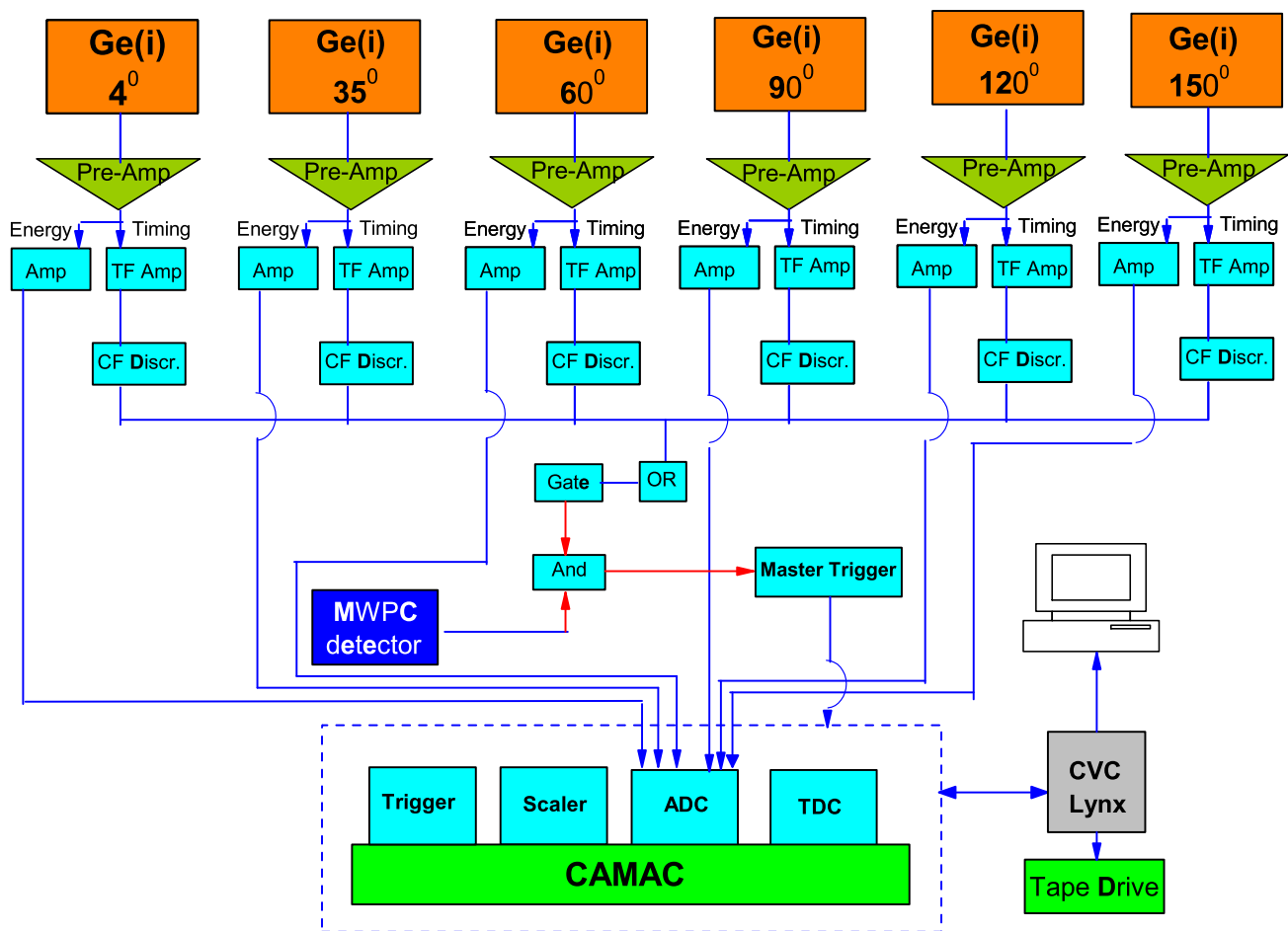


Figure 3.10: Block diagram of the electronics and data acquisition used in this work.



# Chapter 4

## Data Analysis

In this chapter the details of the data analysis, which concentrates on the x-ray spectra, are represented. The analysis of the stored data was performed using the multi-parameter analysis software "SATAN" [74] developed at GSI. The fitting software "*PeaKFit v4*" was used to analyze the x-ray spectra.

The analysis of the recorded x-ray spectra for the ion-atom processes of interest is based on the following steps:

- Doppler Correction.
- Detection efficiency correction.
- Peak fitting procedure.
- Determination of the characteristic ( $K_\alpha$  and  $Ly_\alpha$ ) transition intensities.

In order to identify and disentangle the different projectile radiation contributions in the total spectra, the precise knowledge of the main transition energies for the H- and He-like uranium ions is needed. The energies of the  $Ly_\alpha$  and  $K_\alpha$  transitions (*see figure 2.10*) have been calculated by Artemyev et.al. [75] and are listed in the table 4.1.

Table 4.1: Most probable characteristic transitions for  $U^{90+}$  and  $U^{91+}$ .

Ion	Transition	Type	$E_{emitter}$ (keV)	Transition Probability ( $s^{-1}$ )	Note
$U^{91+}$	$2p_{\frac{3}{2}} \rightarrow 1s_{\frac{1}{2}}$	$Ly_{\alpha 1}$	102.17	$3.95 \times 10^{16}$	Electric dipole
	$2p_{\frac{1}{2}} \rightarrow 1s_{\frac{1}{2}}$	$Ly_{\alpha 2}$	97.61	$4.73 \times 10^{16}$	Electric dipole
	$2s_{\frac{1}{2}} \rightarrow 1s_{\frac{1}{2}}$	$M1$	97.69	$1.95 \times 10^{14}$	Magnetic dipole
$U^{90+}$	$2^1P_1 \rightarrow 1^1S_0$	$K_{\alpha 1}$	100.61	$5.00 \times 10^{16}$	Electric dipole
	$2^3P_1 \rightarrow 1^1S_0$	$K_{\alpha 2}$	96.17	$2.99 \times 10^{16}$	Electric dipole
	$2^3P_2 \rightarrow 1^1S_0$	$M2$	100.55	$2.06 \times 10^{14}$	Magnetic quadrupole

## 4.1 Doppler Corrections: The Doppler Shift and the Doppler Broadening

The radiation emitted by ions moving with relativistic velocities is affected by the Doppler effect which introduces a difference in the transition energies between the emitter and observer frames (Doppler Shift) and between transitions observed at different angles (Doppler Broadening). Therefore photon energies measured in the laboratory system have to be corrected for the relativistic Doppler shift using the relation [76]:

$$E_{emitter} = E_{lab} \cdot \gamma \cdot (1 - \beta \cos \theta_{lab}) \quad (4.1)$$

where  $E_{emitter}$  and  $E_{lab}$  are the photon energies in the emitter and laboratory systems, respectively,  $\theta_{lab}$  denotes the laboratory observation angle (close to  $0^\circ$ ,  $35^\circ$ ,  $60^\circ$ ,  $90^\circ$ ,  $120^\circ$  and  $150^\circ$  in this work),  $\beta$  is the reduced velocity in units of the speed of light and  $\gamma$  is the relativistic Lorentz factor ( $\gamma = \frac{1}{\sqrt{1-\beta^2}}$ ). The corresponding values of Doppler corrected energies for the main transitions in the present experimental study are listed in the table 4.2. In figure 4.1, the ratio  $E_{lab}/E_{emitter}$  is plotted as a function of observation angles for the beam energy of  $220 \text{ MeV}/u$ .

Another relativistic effect on the measured x-ray energy spectra is, as men-

Table 4.2: Transition energies transformation from laboratory frame to the emitter frame.

Transition	$E_{emit}$ (keV)	$E_{lab}$ (keV)				
		35°	60°	90°	120°	150°
$Ly_{\alpha 1}$	102.17	159	117.5	82.7	64.4	55.2
$Ly_{\alpha 2}$	97.61	152.3	112.3	79.1	61.5	52.7
K-REC	250	388	287.5	200	155	132.5
L-REC	149.4	233	171.8	121	94.1	80.6

tioned above, the increase in the line width  $\Delta E$  due to the opening of the observation angle  $\Delta\theta$ . However, the observed line width of the x-ray energy is defined not only by the Doppler broadening but also by the energy resolution of the detector. From the equation 4.1, the relation which describes the Doppler width at observation angles between  $0^\circ$  and  $180^\circ$ , can be written as a function of the width of the observation angle  $\Delta\theta$ :

$$\Delta E_{lab} = \frac{E_{lab} \cdot \beta \cdot \sin \theta_{lab}}{1 - \beta \cdot \cos \theta_{lab}} \Delta \theta_{lab}, \quad (4.2)$$

where  $\Delta E$  is the energy broadening due to the width  $\Delta\theta$  in the observation angle. This dependence is presented in figure 4.2 for two different values of  $\Delta\theta$ . It can be observed that the reduction of the angular width reduces significantly the broadening of the measured transition energies. The immediate consequence of this observation is the use of different collimators in front of the detectors to improve the separation of the different energies corresponding to the different transitions in the H-like uranium ion. For example, the germanium detector located perpendicular to the beam direction ( $\theta = 90^\circ$ ), having an area of  $500 \text{ mm}^2$  and placed  $500 \text{ mm}$  away from the target center has an angular opening of  $\Delta\theta = 2.86^\circ$  in the laboratory system, which indicates a Doppler width (in  $keV$ ) equal to  $0.029 * E_{lab}$  for the x-ray energy emitted by the  $220 \text{ MeV}/u$  uranium ions. However, apart of this improvement, the collimation of the detectors implies the reduction of the observation solid angle by reducing the detector active area and therefore of the reduction of the detection efficiency.

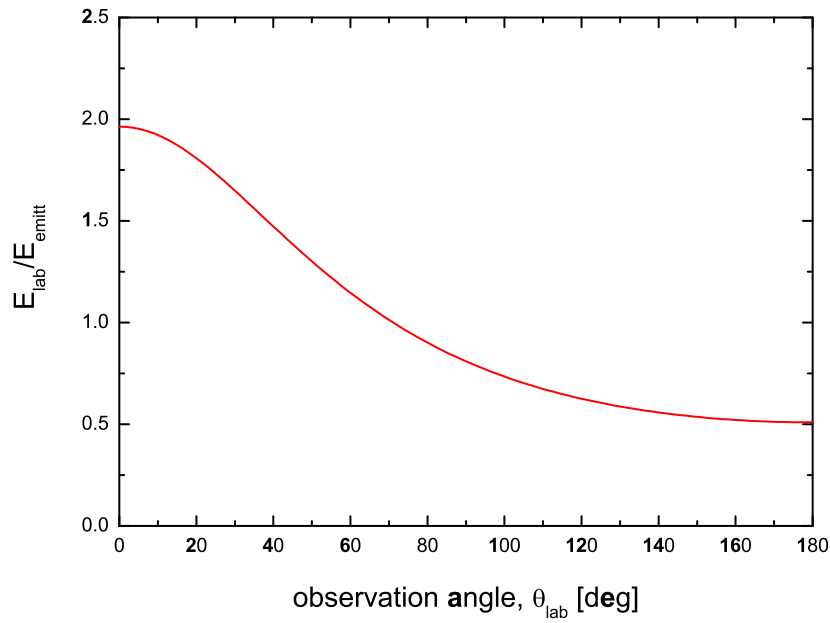


Figure 4.1: Relativistic transformation of the transition energy from the emitter frame moving with a reduced velocity of  $\beta \approx 0.6$  ( $220 \text{ MeV}/u$ ) in the laboratory frame as a function of observation angle.

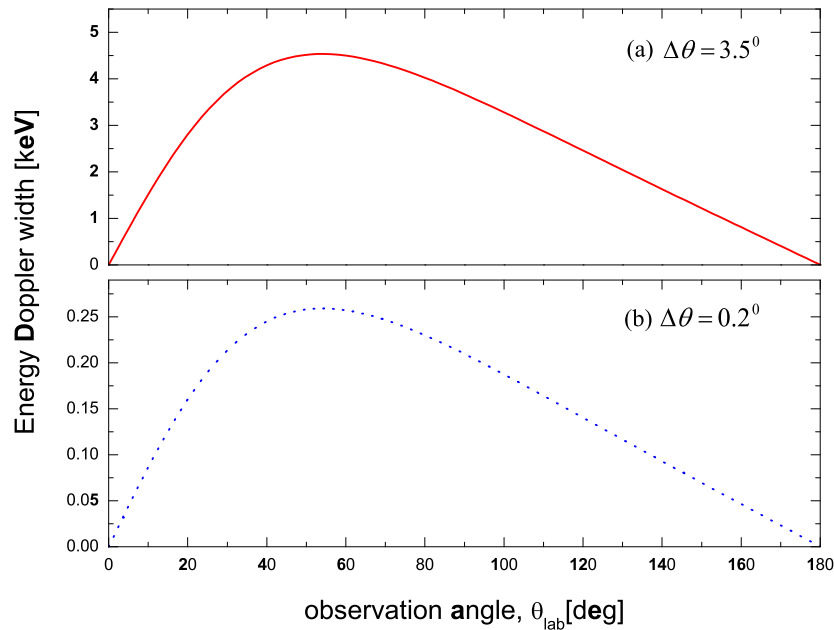


Figure 4.2: Doppler broadening for the transition in H-like uranium ions as calculated from the equation 4.2: (a) without collimator ( $\Delta\theta = 3.5^\circ$ ), and (b) with the collimator ( $\Delta\theta = 0.2^\circ$ ).

## 4.2 Detection Efficiency of the x-ray detectors

The necessity of absolute measurements of x-rays yields by intrinsic germanium detectors has created the demand for determining the absolute detection efficiency. For the detectors used in the present experiment, two approaches can be considered: the experimental evaluations or theoretical determination by simulation of the experiment conditions. In the present work, the detection efficiency for all detectors used was determined by a theoretical model originally introduced by Hansen et al. [77]. This model calculates the absolute detection efficiency for semiconductors-based photon detectors (Si(Li), Ge(i) and Ge(Li)) in the energy range  $13\text{ keV}$  to  $100\text{ keV}$ . A comparison with experimental data made by the authors in the reference [77] shows that the results obtained by using this model are in agreement with the measured values with an accuracy of  $\sim 3\%$  for photon energy between  $13\text{ keV}$  and  $60\text{ keV}$ .

In order to theoretically estimate the absolute detection efficiency, a number of physical and geometrical parameters such as: source-detector distance, semiconductor dead-layer thickness, the thickness of the gold contacts, the sensitive detection area and collimation geometry are required and should be carefully measured.

The procedure used for the determination of the detection efficiency, for the intrinsic germanium detectors used in the present experiment, based on the Hansen model, is presented in the following subsections.

### 4.2.1 Detection efficiency definition

The absolute detection efficiency, defined as the ratio between the number of recorded photons,  $N_\gamma$ , and the total number of photons emitted by the source,  $N_s$ :

$$\epsilon_{abs} = \frac{N_\gamma}{N_s}, \quad (4.3)$$

is dependent not only on detector properties but also on the details of the counting geometry.

The intrinsic efficiency is defined as the ratio between the number of recorded photons and the number of photons reaching the detector,  $N_d$ :

$$\epsilon_I = \frac{N_\gamma}{N_d}. \quad (4.4)$$

The intrinsic efficiency depends primarily on the detector material, the sensitive detection area, and the radiation energy. The two efficiencies are simply related by the formula:

$$\epsilon_I = \epsilon_{abs} \cdot \frac{\Delta\Omega}{4\pi}, \quad (4.5)$$

where  $\Omega$  is the solid angle of the detector seen from the actual source position.

## 4.2.2 Physical description of the efficiency-energy relationship

According to the Hansen's model [77], the absolute detection efficiency of a semiconductor detector can be defined as the product of the intrinsic efficiency  $\epsilon_I$  and several correction factors. For the case of the germanium detectors used in the present experiment, the detection efficiency for photons of energy  $E$  can be written as:

$$\epsilon(E) = \epsilon_I(E) \cdot G(E) \cdot f_{Be} \cdot f_d \cdot f_e \cdot f_c \quad (4.6)$$

where  $G(E)$  is the geometric factor correction,  $f_{Be}$  and  $f_d$  are transmission factors through the detector beryllium window and frontal dead layer, respectively.  $f_e$  is the escape correction factor for the germanium x-ray leaving the detection sensitive volume and  $f_c$  accounts for the effect of collimation.

Considering the absorption of the photons between the source and the detector, the photons are attenuated in intensity as they pass through the matter. This attenuation can be described as an exponential decay along the propagation distance [78]:

$$I(x) = I_0 \cdot e^{-\sigma_{total} \cdot \rho \cdot x} \quad (4.7)$$

where  $I_0$  is the initial intensity incident on the absorber,  $\sigma_{total}$  is the total cross section of the photon interaction with matter for a given energy, which is a sum of the cross section of all processes (photoelectric effect, Compton scattering and pair production) [78, 79],  $\rho$  is the density of the matter and  $x$  is the thickness of the absorber. From the equation 4.7, the correction factors for the absorption in the different layers ( $f_{Be}$ ,  $f_d$ ,  $f_c$ ,  $f_e$ ) can be calculated as:

$$f = e^{-\sum \mu_i x_i} \quad (4.8)$$

where  $\mu_i$  is the total attenuation coefficient of the  $i$ th element and  $x_i$  is the thickness of the  $i$ th absorber place between the source and the detector front face.

For the energy range of interest in this work ( $13 \text{ keV} - 100 \text{ keV}$ ), the main contribution for the photon interaction cross section is given by the photoelectric effect. However, from the point of view of Hansen model used, this energy range divides into two regions: (1) the low-energy range, where  $\sigma_{ph} > 10\sigma_{sc}$ , the upper limit being  $60 \text{ keV}$  for germanium and (2) high energy range, where  $\sigma_{ph} \leq 10\sigma_{sc}$ . Here  $\sigma_{ph}$  is the photoelectric cross section and  $\sigma_{sc}$  is the cross section for the competing process, Compton scattering process.

In general, the attenuation coefficient-energy relationship presented in the figure 4.3 can be described as follows:

$$\mu = a \cdot E^b \quad (4.9)$$

where  $a$  and  $b$  are the coefficients which can be determined. Equation 4.9 can be written as:

$$\ln \mu = \ln a + b \ln E. \quad (4.10)$$

In order to calculate the correction factors needed in this analysis, the absorption curves represented in figure 4.3 were fitted and the two parameters  $a$  and  $b$  were determined. The results are summarized in the table 4.3.

Table 4.3: Fit values for the parameters  $a$  and  $b$  describing the energy dependence of the photon attenuation coefficient (see equation 4.9).

Material	$\ln a$	$\ln b$
Germanium	$11.8612 \pm 0.0711$	$-2.7162 \pm 0.0188$
Beryllium	$-0.9028 \pm 0.0334$	$-0.2432 \pm 0.0083$
Lead	$14.6010 \pm 0.0160$	$-2.5770 \pm 0.0046$

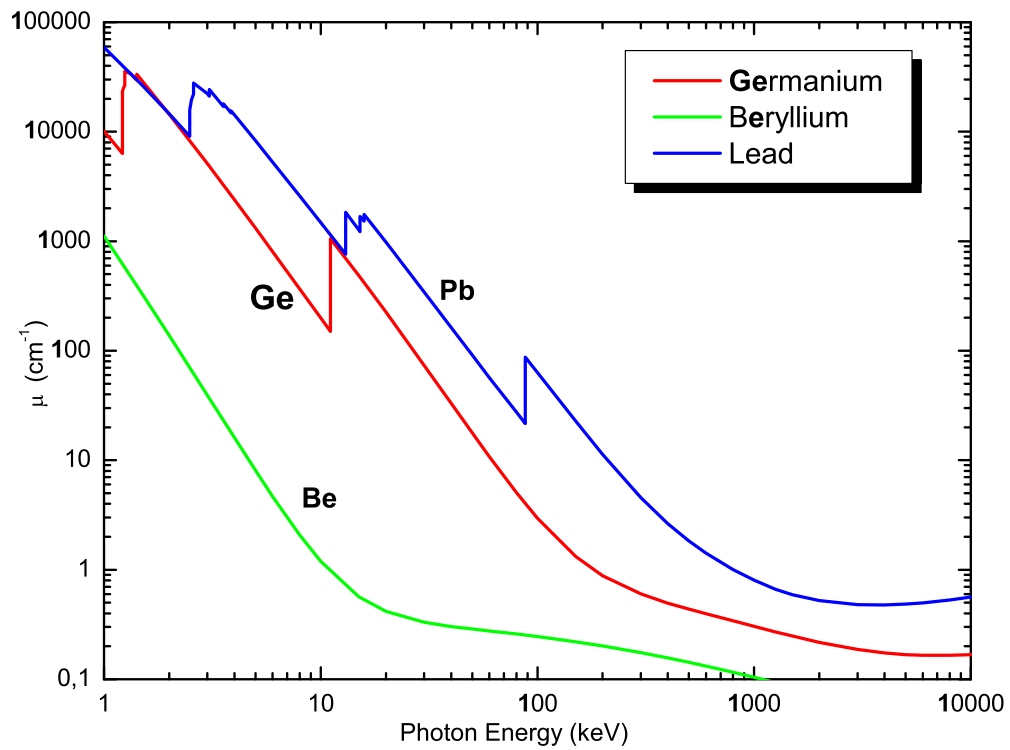


Figure 4.3: Total linear attenuation coefficients plotted as a function of photon energy for germanium, beryllium and lead [72].



### The intrinsic detection efficiency $\epsilon_I(E)$

Generally, the intrinsic detection efficiency of the detector for photons, at low energies and normal incidence, is given by:

$$\epsilon_I = 1 - e^{-\mu_t \cdot D} \quad (4.11)$$

where  $\mu_t$  is the total absorption coefficient and  $D$  is the thickness of the sensitive volume. The absorption coefficient  $\mu$  is energy and material dependent and accounts for different photon absorption processes. Figure 4.3 shows the energy dependence of  $\mu$  for different materials (Ge, Be, Pb). In the case of Ge, the attenuation coefficient  $\mu$  for the energy range  $13 \text{ keV} \leq E \leq 100 \text{ keV}$  is given by the relation:

$$\mu_t(E) = 75.41 * 10^4 E^{-2.72} \text{ cm}^{-1}. \quad (4.12)$$

Hence, the intrinsic detection efficiency for a detector with thickness  $D$  in  $\mu\text{m}$  for x-rays with energy  $E$  in  $\text{keV}$ , can be written as:

$$\epsilon_I = 1 - e^{[-75.41 * D * E^{-2.72}]}. \quad (4.13)$$

For all germanium detectors used in the present work  $D \sim 15 \text{ mm}$  or larger (see the table 3.3) and therefore the intrinsic efficiency  $\epsilon_I$  is not significantly different from unity for the energy range mentioned above.

### The geometric factor $\mathbf{G(E)}$

For a detector of radius  $r$ , thickness  $D$  and front face distance  $d$  from a point source (see figure 4.4), the solid angle  $\Omega$  can be given as [72, 80]:

$$\Omega = 2\pi \cdot \left(1 - \frac{d}{\sqrt{d^2 + r^2}}\right). \quad (4.14)$$

Depending on the energy of the incoming photon, it will penetrate to different depths in the sensitive volume. In the case that the distance source-detector,  $d$ , is larger than the crystal radius,  $r$ , the mean interaction depth  $Z(E)$  can be written as:

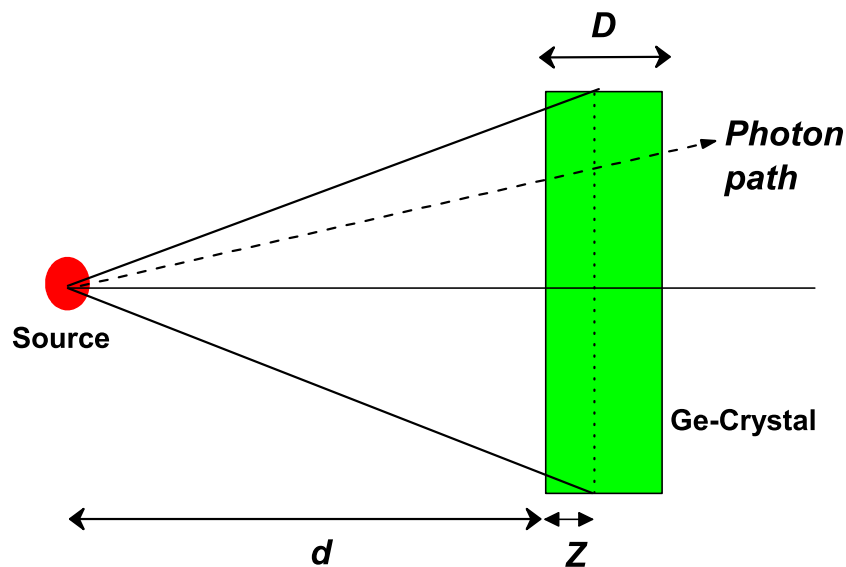


Figure 4.4: The source-detector geometry.

$$Z(E) = \frac{\int_0^D z e^{-\mu z} dz}{\int_0^D e^{-\mu z} dz}, \quad (4.15)$$

where  $\mu$  is the mass attenuation coefficient for germanium. From the equations 4.14 and 4.15, the fractional solid angle subtended by a point source at distance  $d$  from the face of the detector of radius  $r$  is given by:

$$G(E) = \frac{\Omega}{4\pi} = \frac{1}{2} \left( 1 - \frac{[d + Z(E)]}{\sqrt{r^2 + [d + Z(E)]^2}} \right). \quad (4.16)$$

### Beryllium-window correction factor $f_{Be}$

In a similar way as in the case of germanium, the attenuation coefficient for beryllium can be written as:

$$\mu_{Be}(E) = 0.749 * E^{-0.243} \text{ cm}^{-1}. \quad (4.17)$$

Therefore, the transmission factor through the Be-window is

$$f_{Be} = e^{-\mu_{Be}x_{Be}}. \quad (4.18)$$

With the beryllium thickness,  $x_{Be}$ , measured in  $\mu m$  and the photon energy  $E$  in  $keV$ , the equation can be written as:

$$f_{Be} = e^{-0.749 \cdot 10^{-4} x_{Be} E^{-0.243}}. \quad (4.19)$$

For germanium detectors used in this work (*see the table 3.3*), the thickness of the beryllium window is around  $150 \mu m$  and the correction factor for the energy range of the measured transition is 1% or less.

### The dead layer correction factor $f_d$

The dead layer correction factor accounts for the electron loss at the entrance face of the germanium crystal. For a germanium dead layer of  $x_{Ge} \sim 0.5 \mu m$ ,  $f_d = 0.965$  for  $13 keV$  photons. For all used detectors, the dead layer correction factor was independently calculated.

### The escape correction factor $f_e$

During the photon interaction with the crystal, it is probable that some of germanium characteristics x-rays will escape the sensitive area. In this particular case, the energy deposited in the detector is  $\Delta E = E_{photon} - K_\alpha$ . The fractional escape of the germanium K x-rays from the sensitive volume is given by [77]:

$$f_e = 1 - \frac{\omega_K}{2} \left( k_\alpha \left[ 1 + \frac{\mu_{K_\alpha}}{\mu_t} \ln \left( \frac{\mu_{K_\alpha}}{\mu_{K_\alpha} + \mu_t} \right) \right] + k_\beta \left[ 1 + \frac{\mu_{K_\beta}}{\mu_t} \ln \left( \frac{\mu_{K_\beta}}{\mu_{K_\beta} + \mu_t} \right) \right] \right), \quad (4.20)$$

where  $\mu_t$  is the total attenuation coefficient for the incident photons;  $k_\alpha$  and  $k_\beta = 1 - k_\alpha$  are the fractions of Ge K x-rays in the  $K_\alpha$  and  $K_\beta$  groups,

Table 4.4: The K-line energies and corresponding fluorescence coefficient for Ge.

Symbol	Value	Unit	Ref.
$K_{\alpha 1}$	9.88	keV	[81]
$K_{\beta 1}$	10.98	keV	[81]
$\omega_K$	0.57	–	[82]
$k_{\beta}$	0.15	–	[83]

respectively;  $\mu_{K\alpha}$  and  $\mu_{K\beta}$  are the respective total attenuation coefficients for the K x-rays emitted by germanium and  $\omega_K$  is the K-shell fluorescence yield of germanium (*see the table 4.4*). For photon with energy of 30 keV ( $K_{\alpha}$ -Xe) and 100 keV ( $K_{\alpha}$ -U) the escape factor  $f_e$  is 0.963 and 0.998, respectively. This definition of escape correction factor is valid only when the escape through the sides and the rear of the crystal are negligible.

### The collimation correction factor $f_c$

This correction factor is introduced by the collimation of the detector solid angle to reduce the Doppler broadening. This limits the detector entrance window to less than the radius of the sensitive volume of the crystal. It accounts for attenuation in the collimator and the sensitivity of the volume under the collimator. The collimation correction factor can be calculated using the relation:

$$f_c = 1 + \frac{G'}{G} e^{-\mu_c x_c} \quad (4.21)$$

where  $x_c$  is the collimator thickness,  $\mu_c$  is the attenuation coefficient of the collimator material and  $G$  is the geometric factor. The primed quantity refers to the sensitive volume under the collimator, and all other correction factors are assumed to be the same as for the uncollimated region.

Table 4.5: Detector geometry and collimator parameters (all values are in  $mm$ ).

Angle	Diameter	Slit width	Slit thickness	Distance to target	$\frac{\Delta\Omega}{4\pi}$
35°	44	4	10	360	$1.08 \times 10^{-4}$
60°	50	3	7	420	$6.77 \times 10^{-5}$
90°	25	4	5	500	$3.18 \times 10^{-5}$
120°	25	3	5	500	$2.39 \times 10^{-5}$
150°	25	10	5	320	$1.94 \times 10^{-4}$

For the present measurements, the collimator was made out of lead having different slit thicknesses and widths. The geometrical parameters of the collimators used for the germanium detectors are listed in the table 4.5. For the energy range of interest ( $13 \text{ keV} \leq E \leq 100 \text{ keV}$ ) the attenuation coefficient for lead is given by:

$$\mu_{Pb}(E) = 2.19 * 10^6 * E^{-2.577} \text{ cm}^{-1}. \quad (4.22)$$

### 4.2.3 Model calculation and discussion

Using the previous considerations and the derived formulae, the detection efficiency of the germanium detectors used in the experiment was calculated for photon energies between  $13 \text{ keV}$  and  $100 \text{ keV}$ . By using the software package "MATHEMATICA 5.0" [84], the simulation of the detection efficiency have been done and the results of this calculation are presented in the figure 4.5. This procedure allowed to extrapolate the efficiency curves to regions above  $100 \text{ keV}$ . The detection efficiencies of the detectors used, in the energy ranges of interest, are varying between 80% and 90%. This estimation does not include the absorption in the beryllium window of the target chamber, and in the layer of air between chamber window and the detector window ( $\sim 5 \text{ mm}$ ).

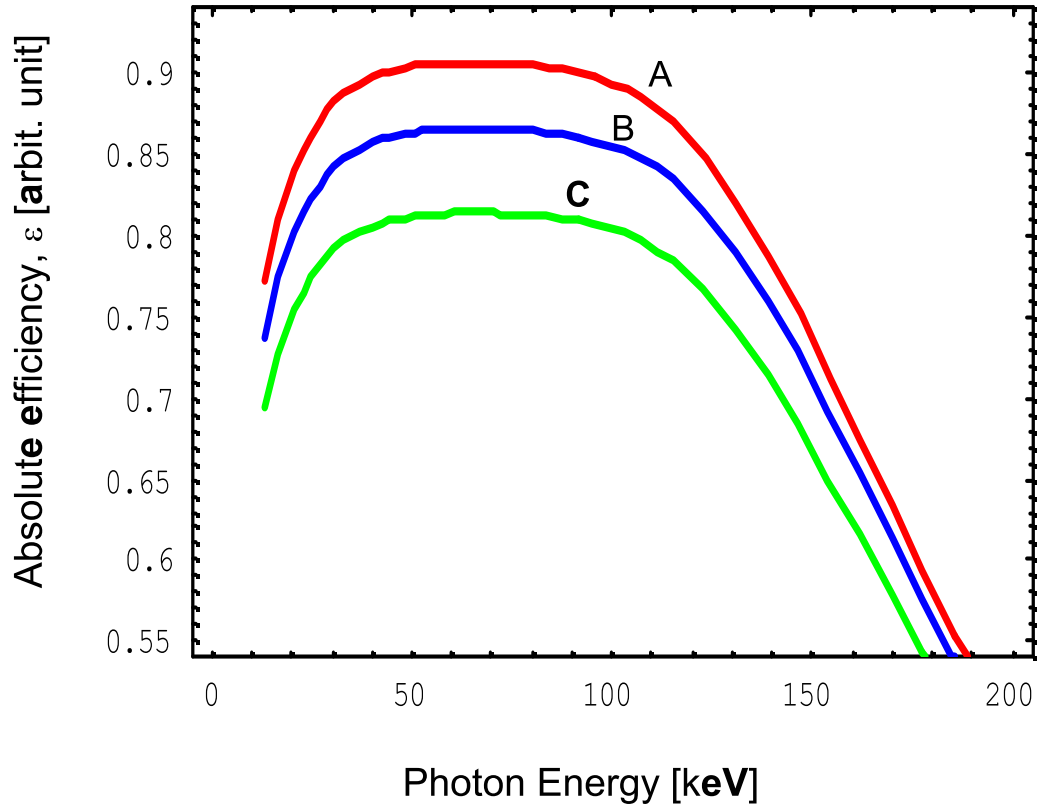


Figure 4.5: Absolute detector efficiency versus photon energy for the germanium detectors used in the present work and placed at: at  $35^\circ$  (A),  $60^\circ$  (B), and  $90^\circ$ ,  $120^\circ$  and  $150^\circ$  (C).

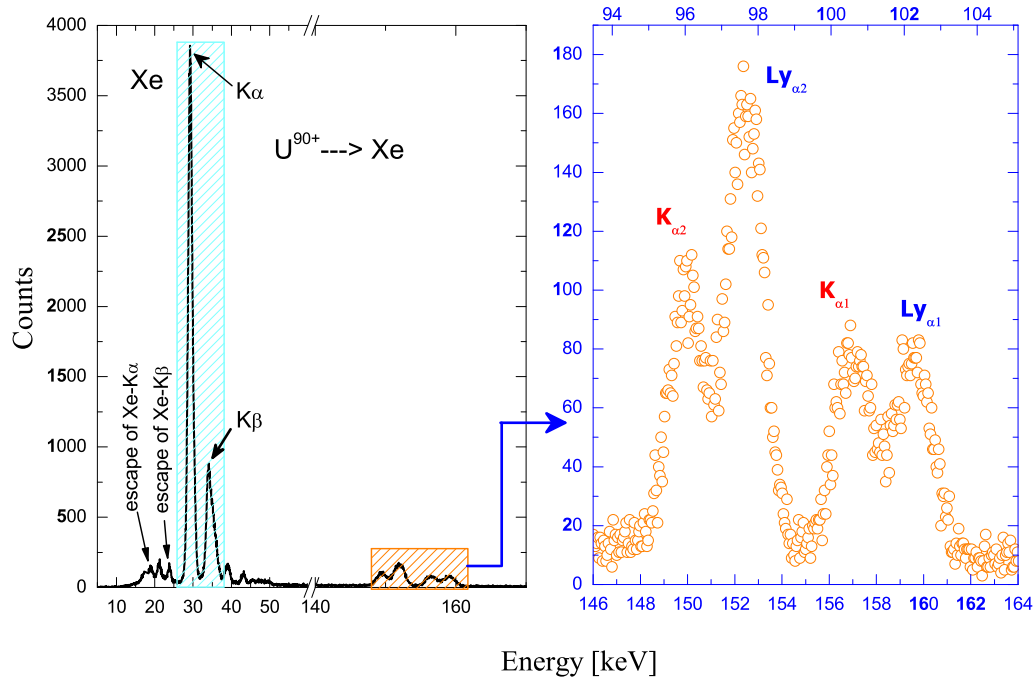


Figure 4.6: X-ray energy spectrum as observed by the germanium detector at 35°.

### 4.3 The Simultaneous Excitation and Ionization process

The simultaneous ionization and excitation of the He-like system into  $nlj$  states can be identified through the observation of ground state x-ray emission  $Ly_\alpha$  in coincidence with up-charged (H-like) projectiles. Using the coincidence technique, it is possible to measure the transition intensities to deduce the intensity ratio  $Ly_{\alpha 1}/Ly_{\alpha 2}$ .

Figure 4.6 shows an x-ray spectrum recorded for initially He-like uranium ions colliding with xenon target atoms at the energy of 220 MeV/u. The spectrum was recorded by using the germanium detector located at 35° in coincidence with the up-charged ions ( $U^{91+}$ ). In this spectrum, two groups of lines have been identified. In the low-energy region, the strong Xe-transition

Table 4.6: Energies of the x-ray emission lines from *Xe* and *Pb* (all values are in *keV*) [85].

	<i>Element</i>	$(2p_{\frac{3}{2}} \rightarrow 2s_{\frac{1}{2}})K_{\alpha 1}$	$(2p_{\frac{1}{2}} \rightarrow 2s_{\frac{1}{2}})K_{\alpha 2}$	$(3p_{\frac{3}{2}} \rightarrow 2s_{\frac{1}{2}})K_{\beta 1}$
<i>Theory</i>	<i>Xe</i>	29.78	29.458	33.62
	<i>Pb</i>	74.97	72.80	84.94
<i>Experiment</i>	<i>Xe</i>	30.01	–	34.00
	<i>Pb</i>	75.04	72.83	85.00

lines are visible. The presence of these lines is due to the ionization of the *Xe*-target by the projectile during the collisions. The values of the *Xe*-transition energies  $K_{\alpha}$  and  $K_{\beta}$  are listed in the table 4.6. In the high-energy part of the spectrum four different transition lines belonging to the uranium projectile are present. These transition lines give information about the different collision processes leading to the projectile x-ray emission.

In order to disentangle the contributions from the different collision processes, the coincidence time spectrum recorded simultaneously with the energy spectrum was used (*see figure 4.7*). The "prompt" peak denotes the true coincidence between photons and up-charged H-like uranium ions. The regions labeled "random" is created by photons originating from different beam pulses and cosmic rays. As seen in the figure, the spectrum shows two prompt peaks. The first narrow peak contains the  $Ly_{\alpha}$  line (L-shell to K-shell transitions) in the H-like uranium ions, whereas the second, broad peak arises from the emission in the *Xe* target atoms.

Starting from the original energy spectrum (*figure 4.6*) and selecting from the time spectrum represented in *figure 4.7*, only the true events contained in the first prompt peak, a new energy spectrum can be generated (*see figure 4.8*). In the new spectrum, the projectile contribution is reduced mainly to the  $Ly_{\alpha}$  transitions. However, the two lines belonging to the projectile ions still present small contribution with different energies (*the red marked part of the spectrum in figure 4.8*). This contribution was completely eliminated by subtracting from the time spectrum the random contribution. In addition, to reduce the background photons and produce a clean ground state x-ray energy spectrum,



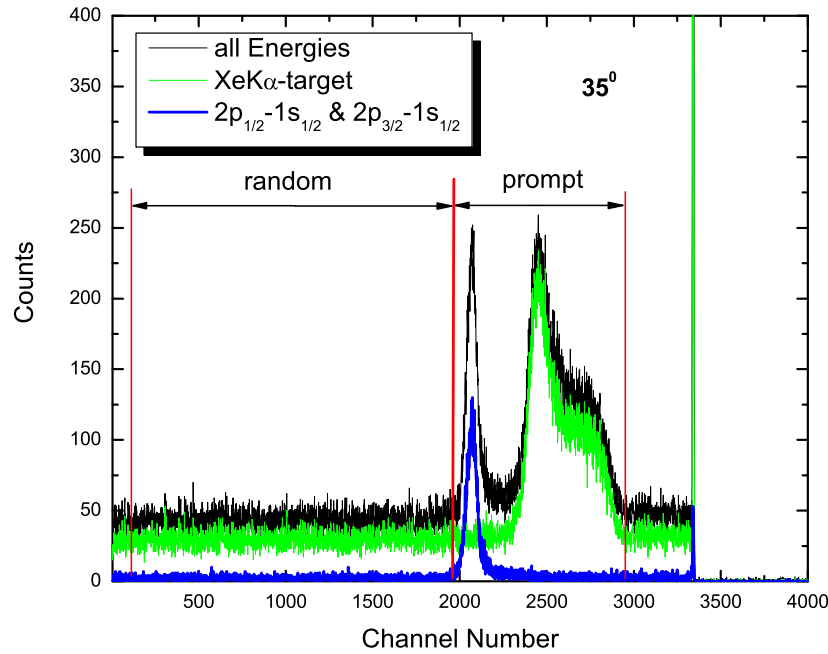


Figure 4.7: The photon-particle coincidence time spectrum. The x-ray detector was placed at  $35^\circ$  (for details see the text).

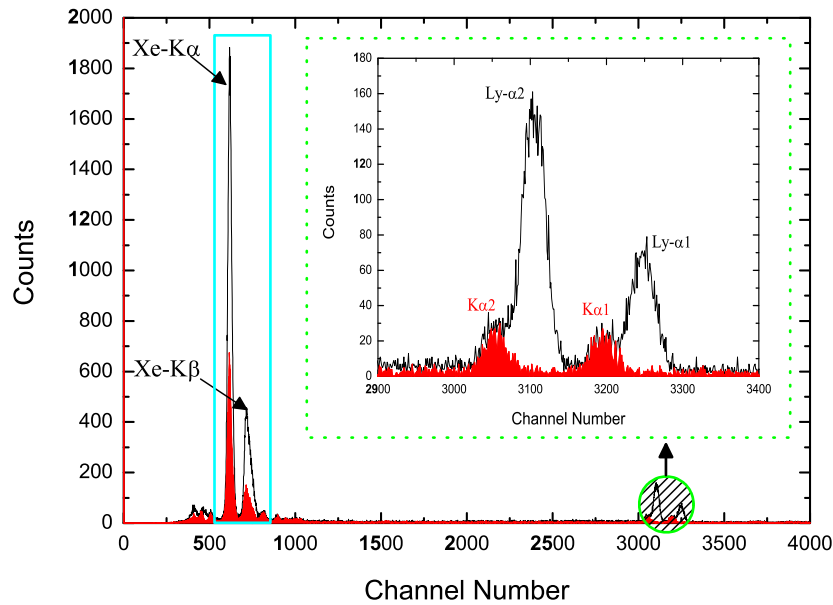


Figure 4.8: X-ray energy spectrum for H-like uranium. The spectrum was measured, at  $35^\circ$ , in coincidence with up-charged uranium ions. The filled spectrum corresponds to random events from the time spectrum. The inset displays the resolved Lyman transitions.

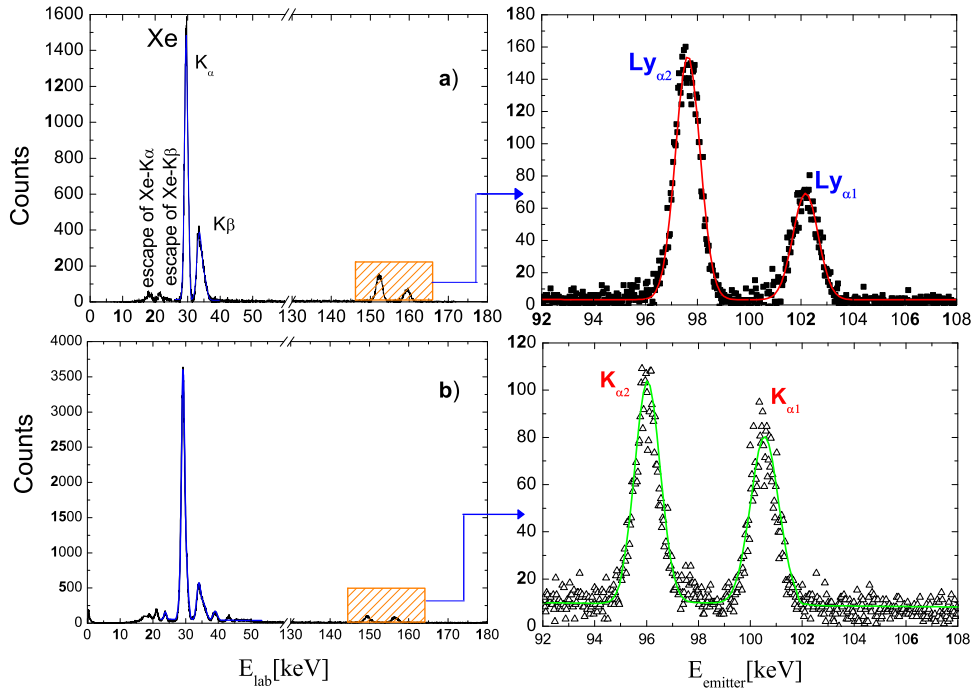


Figure 4.9: X-ray energy spectra, for  $220 \text{ MeV}/u \text{ U}^{90+}$  ions colliding with  $\text{Xe}$  gas target, as observed by the germanium detector at  $35^\circ$ .

different possibilities in the data analysis have been used; applying condition on the coincidence spectrum to produce new energy spectrum and vice versa. Using this technique, the background photons in the x-ray spectra disappear and a clean spectrum is produced. By applying proper energy windows on the  $\text{Ly}_\alpha$  transitions, a new plot of coincidence time spectrum is produced (*see the blue spectrum in the figure 4.7*).

The clean energy spectrum corresponding to the coincidence with the H-like uranium ions is shown in figure 4.9a. In order to separate the projectile  $\text{K}_\alpha$  transitions from the  $\text{Ly}_\alpha$  lines, the spectrum represented in figure 4.9a was subtracted from that in figure 4.6. The result of this technique is shown in figure 4.9b. After the disentanglement, the energy spectra have been corrected for the Doppler shift (*see section 4.1*) and the detection efficiency (*see section 4.2*).

Table 4.7: Gaussian fit parameters for the  $Ly_{\alpha}$  transitions detected at  $35^{\circ}$  in coincidence with the  $U^{91+}$  ions (*all values are in keV*).

Transition line	Angle	$a_0$	$a_1$	$a_2$	Peak area
$Ly_{\alpha 1}$	$35^{\circ}$	64.7	102.17	0.76	2485
	$60^{\circ}$	38.7	102.16	0.71	1511
	$90^{\circ}$	27.1	102.11	0.55	1200
	$120^{\circ}$	15.2	102.17	0.55	507
	$150^{\circ}$	18.2	102.18	0.23	490
$Ly_{\alpha 2}$	$35^{\circ}$	148.4	97.63	0.74	5520
	$60^{\circ}$	88.2	97.64	0.70	3414
	$90^{\circ}$	63.1	97.68	0.51	2727
	$120^{\circ}$	35.2	97.62	0.55	1253
	$150^{\circ}$	46.3	97.60	0.22	1300

For completeness, to cover the study of the angular distributions for the simultaneous ionization and excitation process, the spectra recorded by the detectors located at all different observation angles were analyzed in a similar way. Figure 4.10 shows the well resolved and emission lines due to ground-state electron excitation into the *L-shell* projectile states. It is interesting to note the significant change in the relative intensities of  $Ly_{\alpha 1}$  and  $Ly_{\alpha 2}$  lines with respect to the  $K_{\alpha 1}$  and  $K_{\alpha 2}$  lines.

Finally, the separated spectra have been fitted using a Gaussian-Amplitude function:

$$y = a_0 e^{-\frac{1}{2} \left( \frac{x-a_1}{a_2} \right)^2} \quad (4.23)$$

where  $a_0$  (amplitude),  $a_1$  (center) and  $a_2$  (width) are the fitting parameters. For  $Ly_{\alpha}$  transitions, the fitting parameters are listed in the table 4.7.

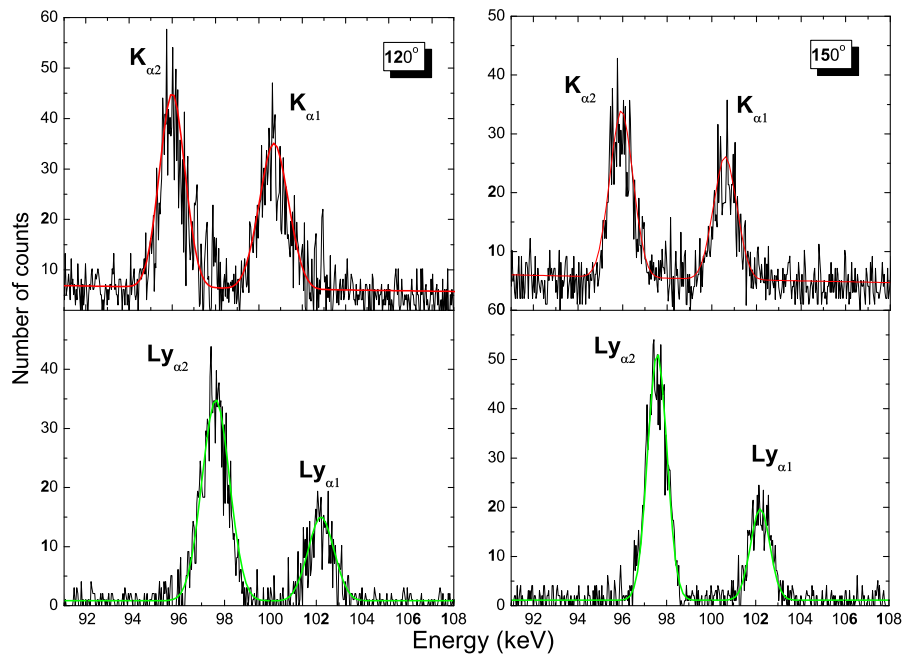
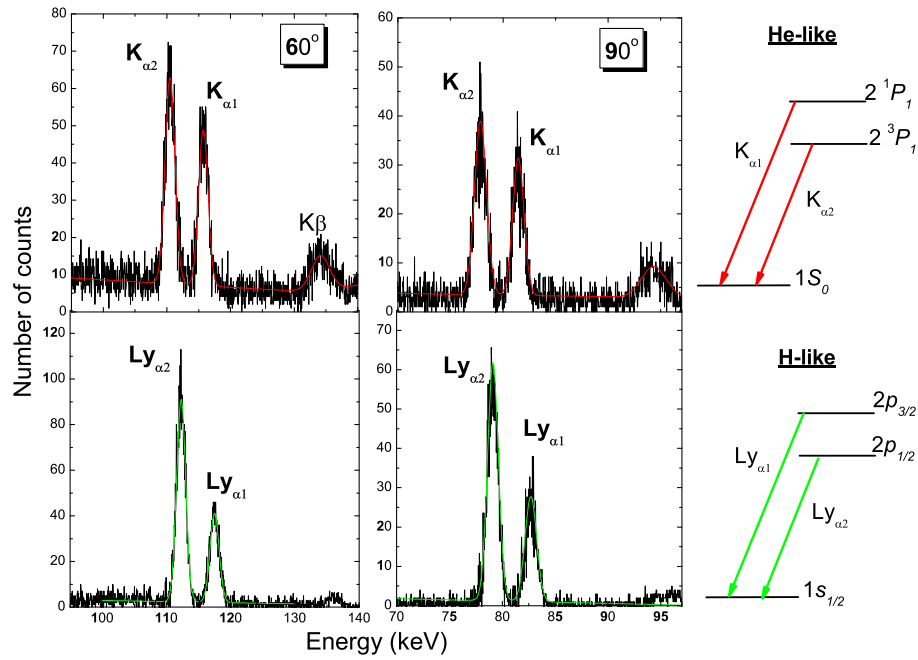


Figure 4.10: The x-ray spectra recorded at 60°, 90°, 120° and 150° for initially He-like uranium ions colliding with Xe gas-target atoms at an energy of 220 MeV/u. The  $K_{\alpha}$  transitions are connected to single excitation and the  $Ly_{\alpha}$  lines were recorded in coincidence with the up-charged H-like uranium ion.

## 4.4 Single Excitation of He-like uranium ions

In order to study the population mechanism for the excited states of He-like uranium ions, another measurement was done by using nitrogen gas-target. The excitation process can be identified by extracting the intensity ratios of the  $K_\alpha$  transitions ( $K_{\alpha 1}/K_{\alpha 2}$ ).

For  $220 \text{ MeV/u } U^{90+} \rightarrow N_2$  collisions, the x-ray spectra recorded without coincidence requirements on the projectile charge states, at different observation angles  $35^\circ$ ,  $60^\circ$ ,  $90^\circ$ ,  $120^\circ$  and  $150^\circ$ , are shown in figure 4.11a. The germanium detectors were covered with a lead shielding to reduce the surrounding background. The strong background radiation ionized the K-shell electrons of the lead atoms, resulting in fluorescence radiation of energies around  $74 \text{ keV}$  (Pb- $K_\alpha$ ) and  $85 \text{ keV}$  (Pb- $K_\beta$ )(*see the table 4.1*), which were detected in the x-ray spectra (*see figure 4.11a*). Due to the Doppler shift, the uranium transition lines are detected in the laboratory system at different energies starting with  $157 \text{ keV}$  ( $K_\alpha$ ) at  $35^\circ$  down to  $54 \text{ keV}$  at  $150^\circ$ . For  $90^\circ$ , the uranium  $K_\alpha$  lines are contaminated by the Pb- $K_\alpha$  lines which makes the separation difficult.

In figure 4.11b, the corresponding x-ray spectra associated with electron capture are also shown. In particular, strong x-ray transition lines in the low-energy region are present. These lines indicate the transitions from the higher levels of Li-like uranium ions into the L-shell ( $n = 2$ ). The group of transitions detected at high energies is associated to the direct electron capture into  $n = 2, 3, \dots, \text{etc.}$  From this group, the most probable transition, the L-REC, indicates a high probability for the direct capture into  $n = 2$ . Due to the filled  $K$ -shell, no  $K_\alpha$  emission is visible within these spectra. The presence of  $K_\alpha$  transition indicates a strong probability for the single excitation process in  $U^{90+} \rightarrow N_2$  collisions.

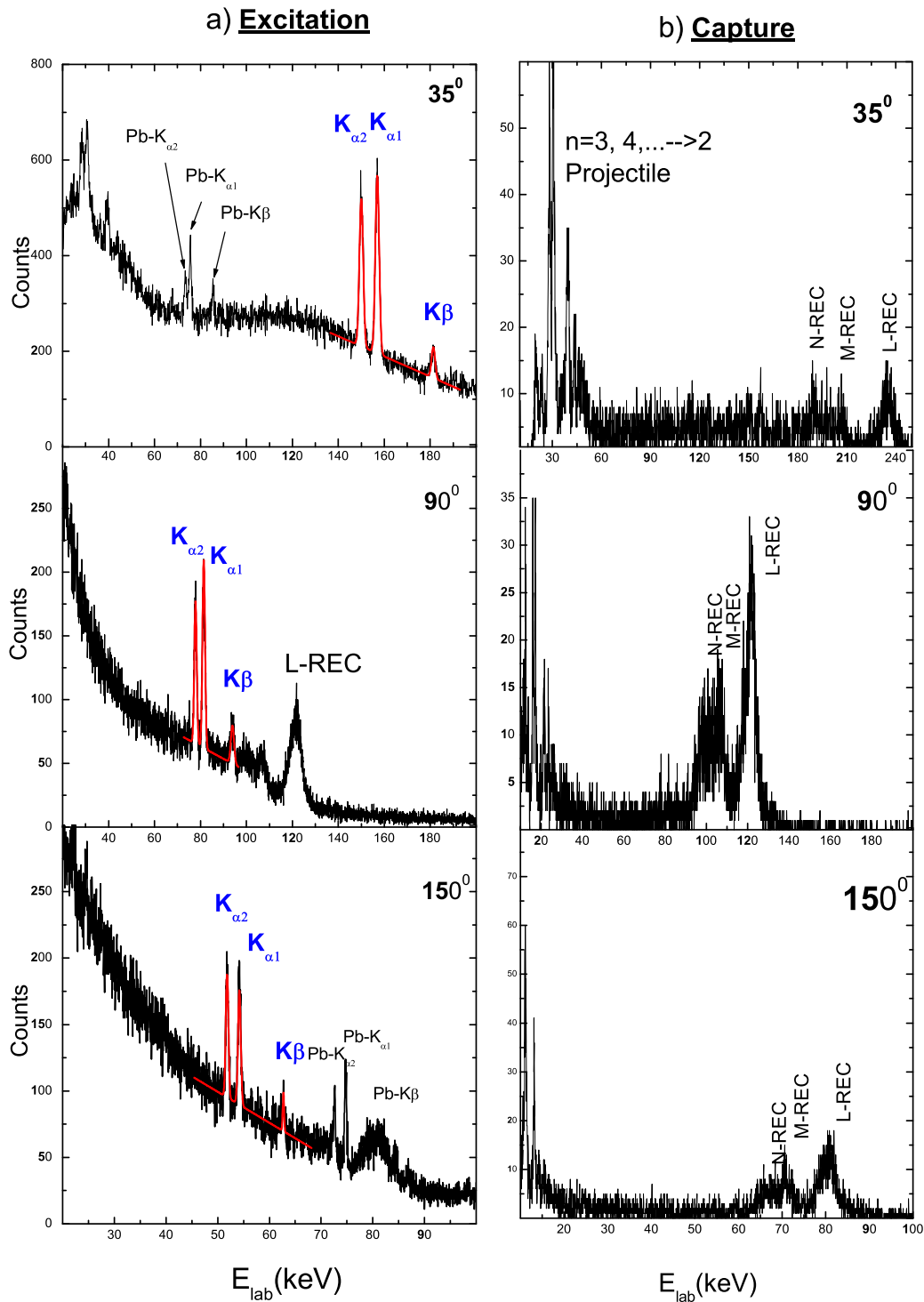


Figure 4.11: Projectile X-ray spectra for  $220 \text{ MeV}/u \text{ U}^{90+} \rightarrow \text{N}_2$  collision measured (a) without coincidence requirement (total emission spectra), (b) in coincidence with down-charged projectile ( $\text{U}^{89+}$ ).

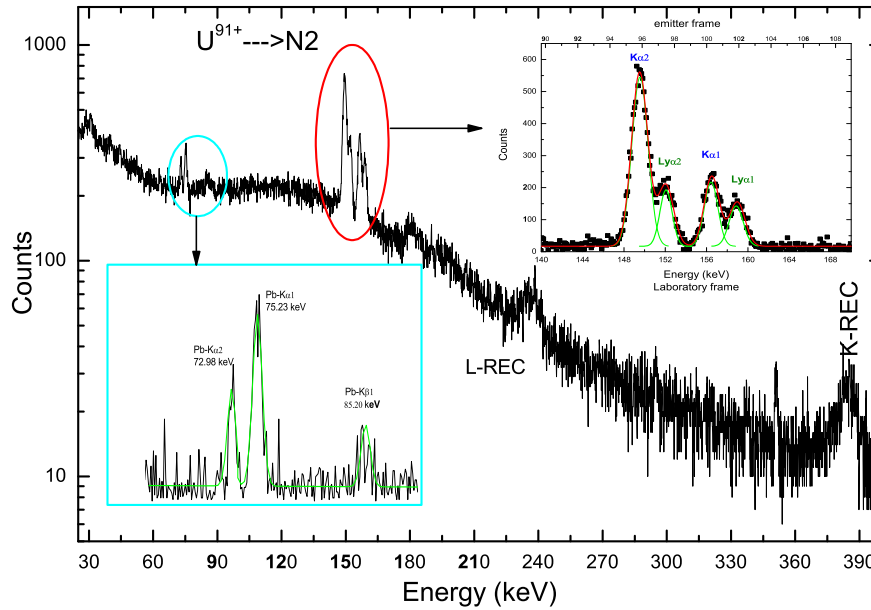


Figure 4.12: X-ray spectrum recorded for initially H-like uranium ions colliding with nitrogen gas target. The inset represents the ground-state x-ray transitions for H- and He-like ions.

## 4.5 Analysis of the REC spectra

To extend the present study to the photon angular distribution in the direct electron capture into the projectile K-shell process (K-REC), the initial projectile charge state was changed to H-like uranium ions. In this case, it was possible to resolve the main transition lines  $K_{\alpha}$  and  $Ly_{\alpha}$ . The energy of the REC photons is given by the sum of the electron binding energy ( $E_b$ ) and the kinetic energy of the free electron in the projectile frame ( $E_{KIN}$ ). In the present experiment the electron kinetic energy  $E_{KIN}$  amounts to  $120.6 \text{ keV}$ . For the REC transitions into the  $1s$  ground state of hydrogen like uranium ( $E_{1s} \approx 130 \text{ keV}$ ), the K-REC peak is found in the high-energy part of the spectrum, at a photon energy of around  $250 \text{ keV}$  (see the table 4.2). REC into excited states leads partially, via cascades, to the well-resolved  $K_{\alpha 1}$  and  $K_{\alpha 2}$  transitions.

Figure 4.12 shows an x-ray spectrum registered by the germanium detector placed at an observation angle of  $35^\circ$  for the projectile incident energy of  $220 \text{ MeV/u}$ . This spectrum was accumulated without coincidence conditions with the projectile charge state. The recorded spectra exhibit a complex structure, due to different atomic processes. The most important contributions are the  $K_\alpha$  and  $Ly_\alpha$  lines.

By selecting coincident events from the coincidence time spectrum between photons and down-charged He-like uranium ions, the x-ray spectra profiles change. The x-ray spectrum corresponding to the electron capture from the  $N_2$  molecules into the H-like uranium ions is represented in figure 4.13. In this spectrum, the main contributions are the  $K_{\alpha 1}$  and  $K_{\alpha 2}$  transitions, but also transitions due to the direct capture into  $n = 1, 2, 3, \dots$  states can be observed. The corresponding coincidence time spectrum is presented in figure 4.14 where different contributions to the capture process have been indicated. To discriminate between different transitions in the H-like ion, which provide direct information about the population yields of the projectile levels via the excitation process, the "anti-coincidence" technique was used. This procedure is demonstrated in the case of the x-ray spectrum detected at  $35^\circ$  (figure 4.12). The region of interest, containing the  $K_\alpha$  and  $Ly_\alpha$  lines, was selected and separately represented in figure 4.15a. Using the coincidence with He-like uranium ions, the contribution of the capture process (see figure 4.15b) can be closely selected from the integral spectrum shown in figure 4.15a. The plot represented in figure 4.15c, obtained as a difference between the single and coincidence spectrum, represents the x-rays originating in the ground state excitation process for the H-like uranium ions.

For completeness, also the x-ray spectra detected at  $60^\circ$ ,  $90^\circ$ ,  $120^\circ$  and  $150^\circ$  were analyzed in a similar way. Figure 4.16 represents the x-ray spectrum accumulated by the detector placed at  $120^\circ$ . The spectrum is entirely dominated by REC into the ground and excited states of the projectile. Due to the partially blocked  $K$ -shell of the projectiles, the yield of  $K$ - and  $L$ -REC photons is comparable.



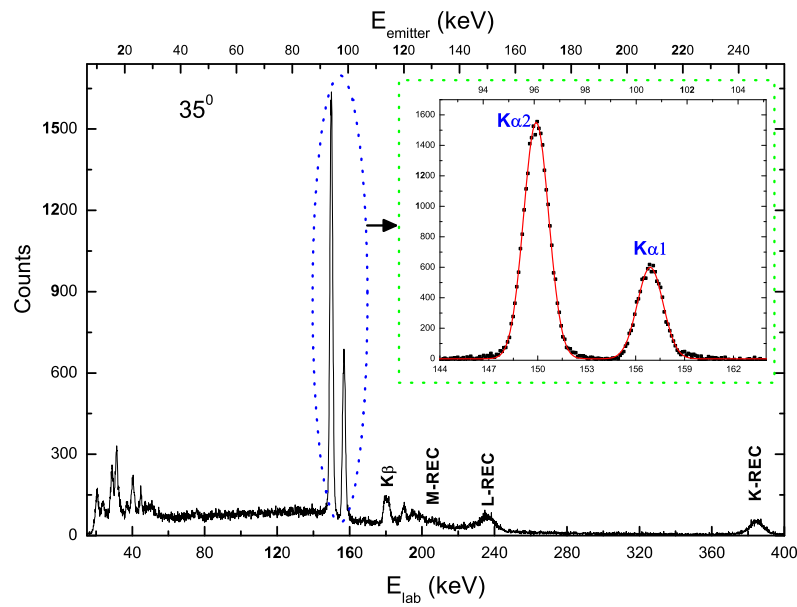


Figure 4.13: X-ray spectrum associated with electron capture into the  $220 \text{ MeV}/u \text{ U}^{91+}$  ions colliding with  $\text{N}_2$ -target, as observed at  $35^\circ$ .

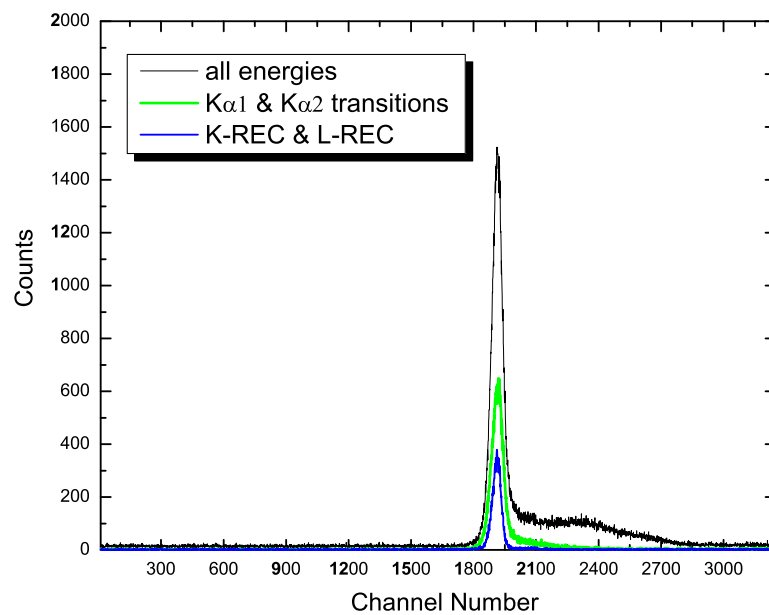


Figure 4.14: Coincidence time spectrum between the x-rays emitted at  $35^\circ$  and  $\text{U}^{90+}$  ions.

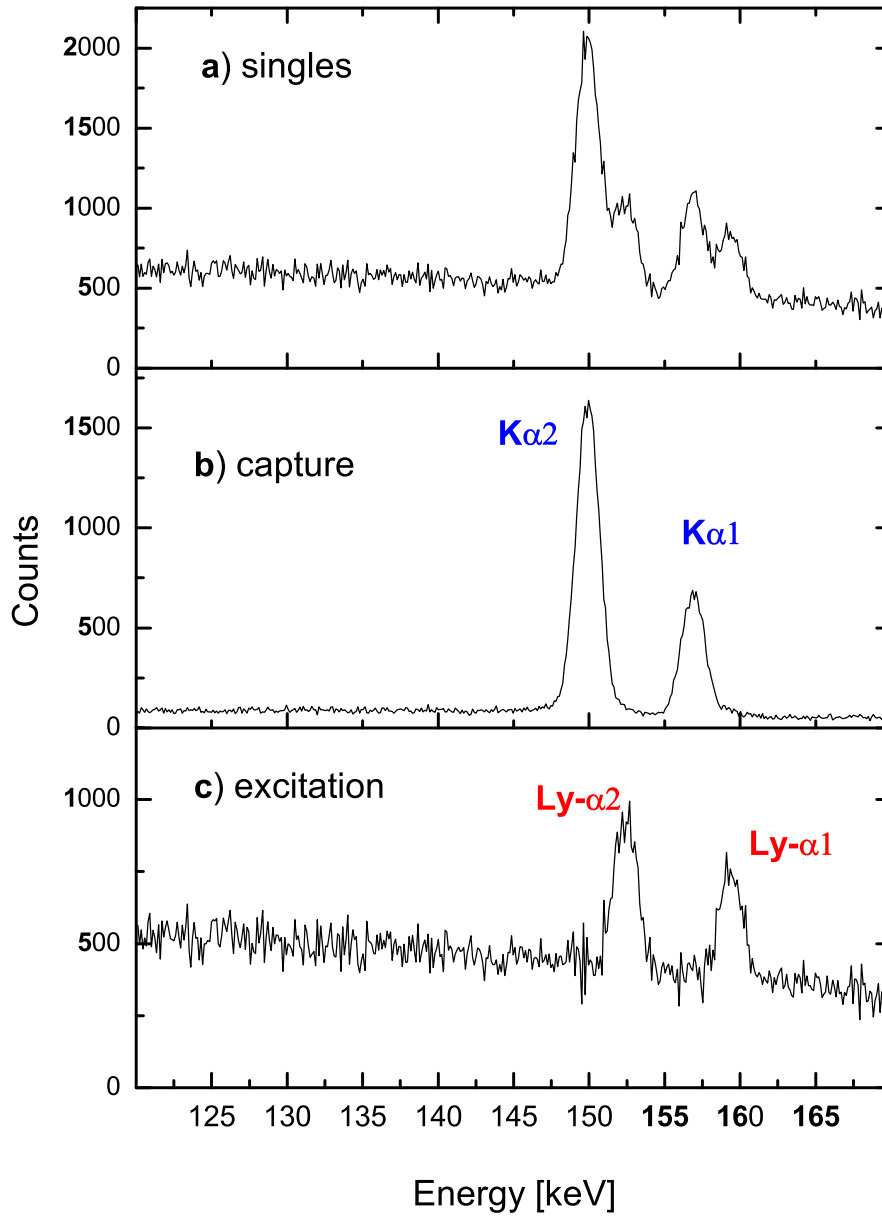


Figure 4.15: Ground state X-ray transitions measured at  $35^\circ$ . The upper plot represents raw data, the middle represent spectrum accumulated in coincidence with  $U^{90+}$  ions and the lower spectrum represents the difference between the two spectra (a) and (b).

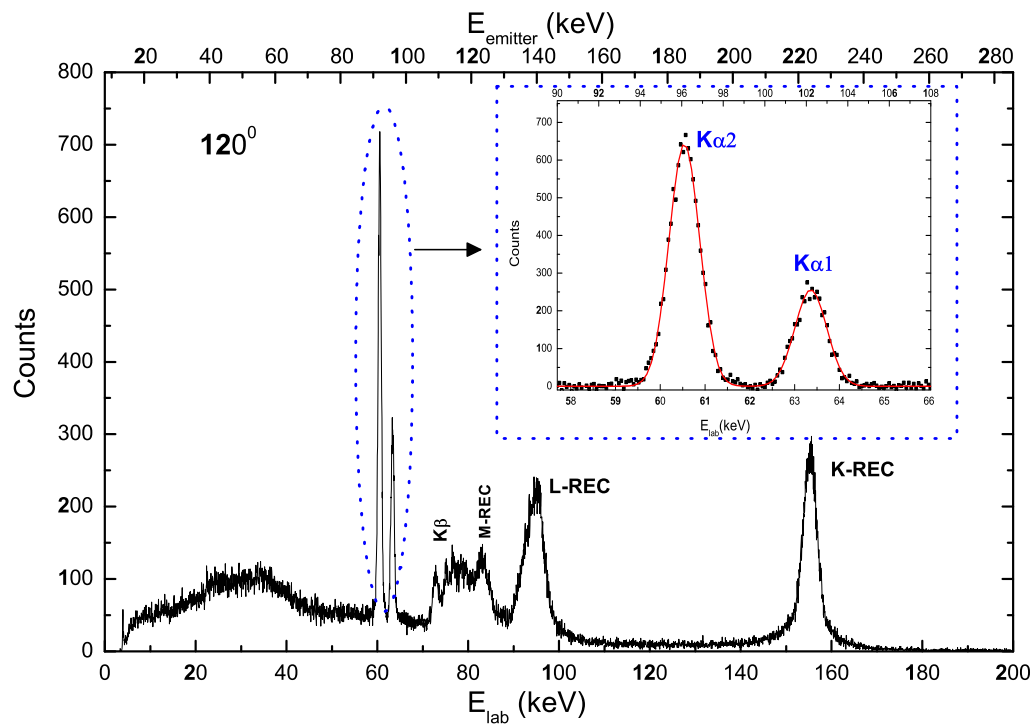


Figure 4.16: X-ray energy spectrum measured in coincidence with  $U^{90+}$ , as observed at  $120^\circ$ .



# Chapter 5

## Results and Discussion

### 5.1 K-shell Excitation of He-like Uranium Ions

He-like ions are the simplest atomic many-body systems. The investigations of the atomic structure of He-like ions probe the understanding of the interplay of relativistic effects on the dynamics of the simple atomic few-electron systems. The formation of excited states of He-like uranium ions can be studied by the observation of the radiative decay of the excited levels to the ground state (*see figure 2.10*). This study can be done via different processes which give information about the population mechanism of the excited L-shell levels.

The Coulomb excitation is a production process of characteristic projectile photons of high-Z ions interacting with light target atoms. Information about the K-shell excitation of He-like uranium ions can be obtained from the study of the angular distribution of the photons associated with the Coulomb excitation process. The experimental data obtained for the direct K-shell excitation of He-like uranium ions, colliding with nitrogen gas-target at a beam energy of  $220 \text{ MeV}/u$ , are plotted in figure 5.1. As can be seen in the figure 5.1, the behavior of the  $K_{\alpha 1}/K_{\alpha 2}$  intensity ratio is similar to that of a pure electric dipole ( $E1$ ) contribution, namely,  $[1s_{1/2}, 2p_{3/2}] \ ^1P_1$  and  $[1s_{1/2}, 2p_{1/2}] \ ^3P_1$  levels for  $K_{\alpha 1}$  and  $K_{\alpha 2}$  transitions, respectively. This suggests that the single excitation process is a highly selective mechanism for the population of  $^1P_1$  state in the He-like uranium ions.

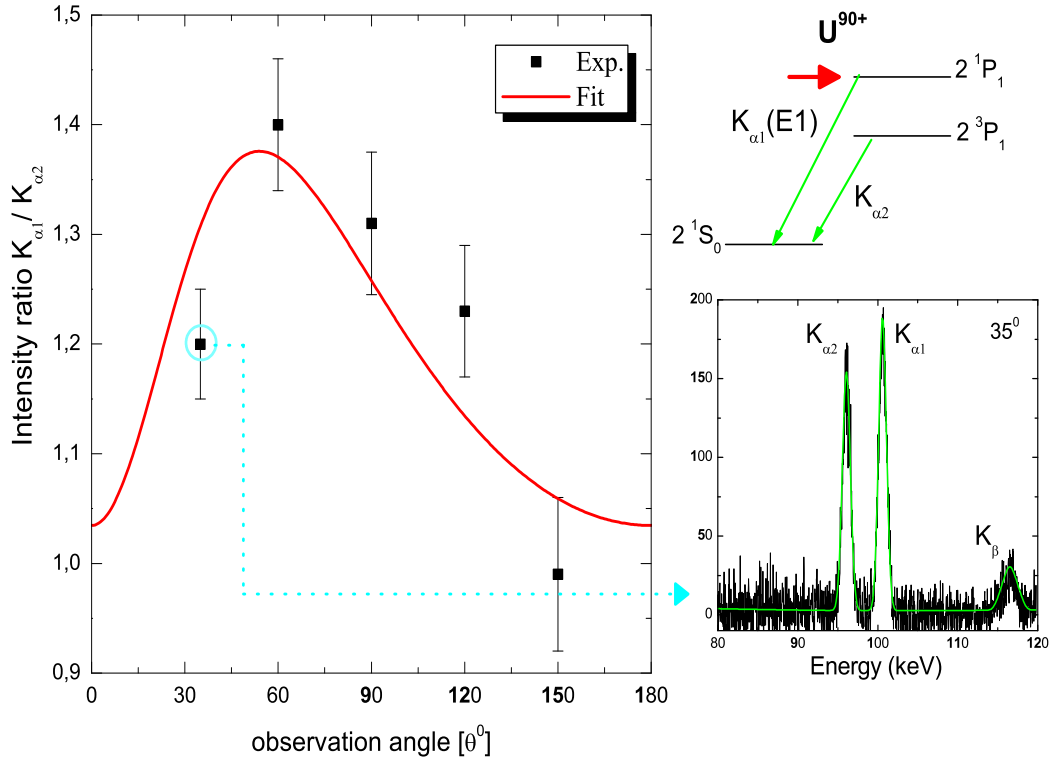


Figure 5.1: Angular distribution of the  $K_{\alpha 1}/K_{\alpha 2}$  intensity ratio, in the laboratory frame, as observed for K-shell excitation of He-like uranium ions colliding with  $N_2$  gas target. The solid line depicts the fit result to the experimental data using the equation 2.31.

Using the experimental angular distribution of the  $K_{\alpha 1}/K_{\alpha 2}$  intensity ratio, represented in the figure 5.1, it is possible to extract the value of anisotropy parameter  $\beta_{20}$ . The value of the anisotropy parameter  $\beta_{20}$  was deduced by a least square fit of equation 2.31 to the experimental data including all required relativistic transformations. The experimental value of anisotropy parameter obtained from this fit was found to be  $\beta_{20}^{exp} = -0.20 \pm 0.03$ .

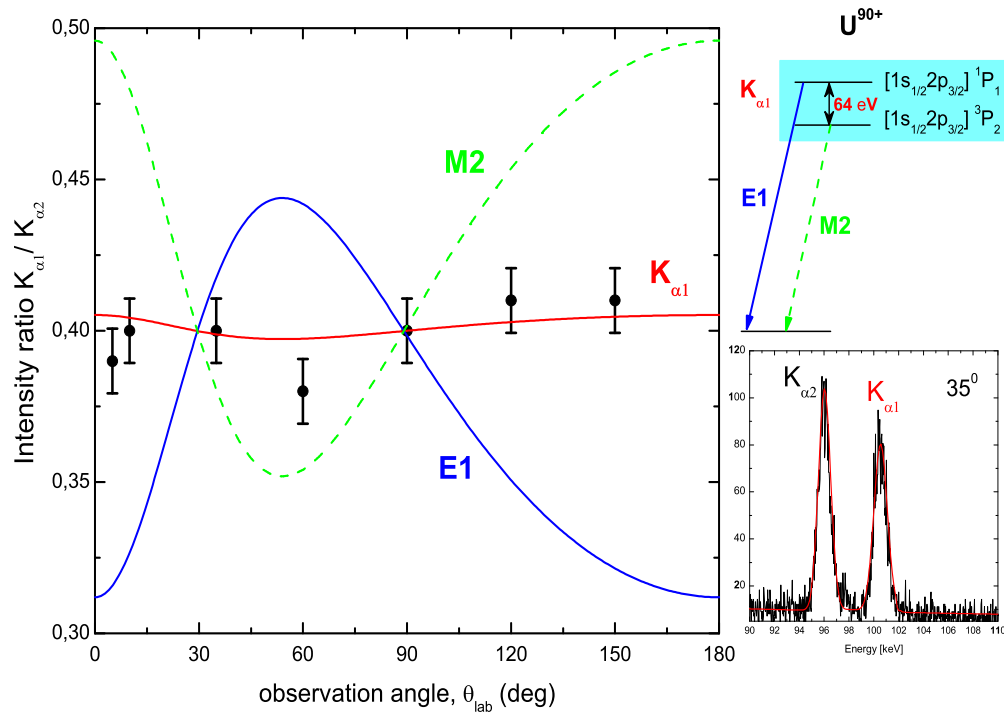


Figure 5.2: Angular distribution of the  $K_{\alpha 1}/K_{\alpha 2}$  intensity ratio as a function of the observation angle. The experimental data for  $220 \text{ MeV}/u \text{ U}^{91+} \rightarrow \text{N}_2$  [55].

## 5.2 Electron Capture into H-like Uranium Ions

### 5.2.1 $K_{\alpha 1}/K_{\alpha 2}$ Intensity Ratio for REC into $\text{U}^{91+}$

While for He-like uranium ions the observation of X-ray transition to the ground state of projectile is a direct signature of the ground state electron excitation, for H-like uranium ions an additional mechanism for the projectile x-rays produced should be considered. That is the radiative electron capture which may directly lead to the emission of the projectile  $K_{\alpha}$  transitions. The experimental results obtained in the present work for the electron capture into initially H-like uranium ions, in collisions with nitrogen gas target at the same incident energy of  $220 \text{ MeV}/u$ , is shown in figure 5.2. As long as the  $^1P_1$  ( $E1$ )

and  ${}^3P_2$  ( $M2$ ) levels are not experimentally resolved, their superposition ( $K_{\alpha 1}$ ) exhibit an isotropic behavior even if the individual components of this line are strongly anisotropic. The experimental proof of this behavior agrees reasonably well with the theoretical calculation based on the Multi-configuration Dirac-Fock (MCDF) approach [53, 55]. The experimental results confirm the theoretical treatment of the two-step capture and decay process which have been considered to describe the formation of the excited states.

### 5.2.2 $Ly_{\alpha 1}/Ly_{\alpha 2}$ Intensity Ratio for REC into $U^{91+}$

As discussed in detail in Ref. [19] the  $Ly_{\alpha 2}$  transition, arising from the decay of the  $2p_{1/2} \rightarrow 2s_{1/2}$ , shows an isotropic emission pattern. Consequently, it provides an ideal tool to measure a possible anisotropy of the  $Ly_{\alpha 1}$  and  $K_{\alpha}$  transitions.

For the collisions of the initially H-like uranium ions with nitrogen gas-target at  $220 \text{ MeV}/u$ , the experimental results in the present work for the emission pattern of the  $Ly_{\alpha 1}$ ,  $K_{\alpha 1}$  and  $K_{\alpha 2}$  transitions are shown in figure 5.3. These transitions are normalized to the  $Ly_{\alpha 2}$  line. As seen from the figure 5.3, no alignment is observed in all cases. For the case of the excitation of H-like uranium ions, the behavior of the  $Ly_{\alpha 1}$  ( $2p_{3/2} \rightarrow 2s_{1/2}$ ) transition agrees with the theoretical predictions for the Coulomb excitation in one-electron system [86]. In contrast to populating excited states of H-like uranium ions by electron excitation, the angular distribution of the  $Ly_{\alpha 1}$  transition produced by REC has been previously studied and found to be anisotropic. The anisotropy of the  $Ly_{\alpha 1}$  transition has been investigated over a large energy range from  $90 \text{ MeV}/u$  to  $300 \text{ MeV}/u$  for electron capture into bare uranium ions colliding with  $N_2$  [56, 87]. The previous experimental data were compared with the predicted results made by Surzhykov et al. [56] and a good agreement over the whole energy region was found.

For the  $K_{\alpha 1}$  transition caused by electron capture into initially H-like uranium ions, the  $K_{\alpha 1}/Ly_{\alpha 2}$  intensity ratio in the figure 5.3 shows within the experimental uncertainties an isotropic behavior (*see straight line*). The practically isotropic distribution displayed in this case, is in a clear contrast to the strong anisotropy found for the initially bare uranium ion case [87].



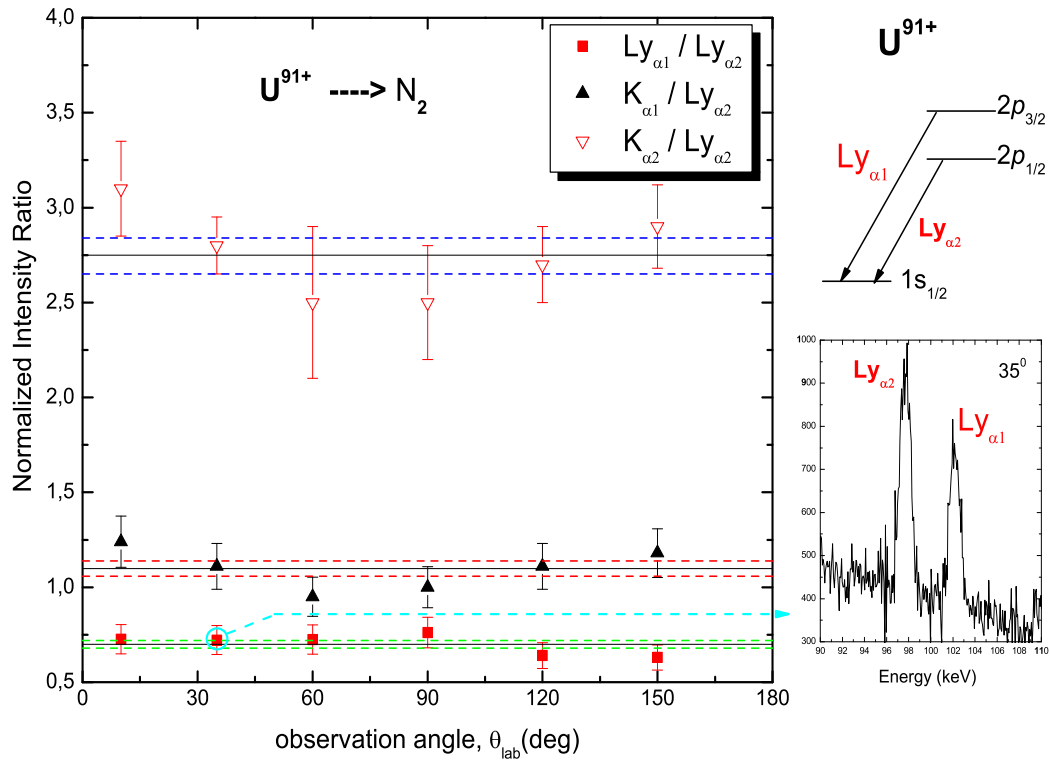


Figure 5.3: The experimental intensities of  $Ly_{\alpha 1}$ ,  $K_{\alpha 1}$  and  $K_{\alpha 2}$  normalized to the  $Ly_{\alpha 2}$  line. The experimental data were measured for  $220 \text{ MeV}/u \text{ } U^{91+} \rightarrow N_2$  collisions. The solid lines refer to the corresponding mean values and the dashed lines give the associated uncertainties.

In addition, the difference in the formation of the excited states in He-like uranium ions is also observed (*for comparison see figures 5.1 and 5.3*). In both cases the  $K_{\alpha 1}$  transition is produced, in one case by single excitation (*figure 5.1*) and in the other case by electron capture (*figure 5.3*). In *figure 5.1*, the angular distribution indicates that only the  $^1P_1$  level contributes to the  $K_{\alpha 1}$  transition. In *figure 5.3*, it is interesting to note the incoherent addition of the  $^1P_1$  (E1) and  $^3P_2$  (M2) components of the  $K_{\alpha 1}$  transition yields to an almost isotropic emission.

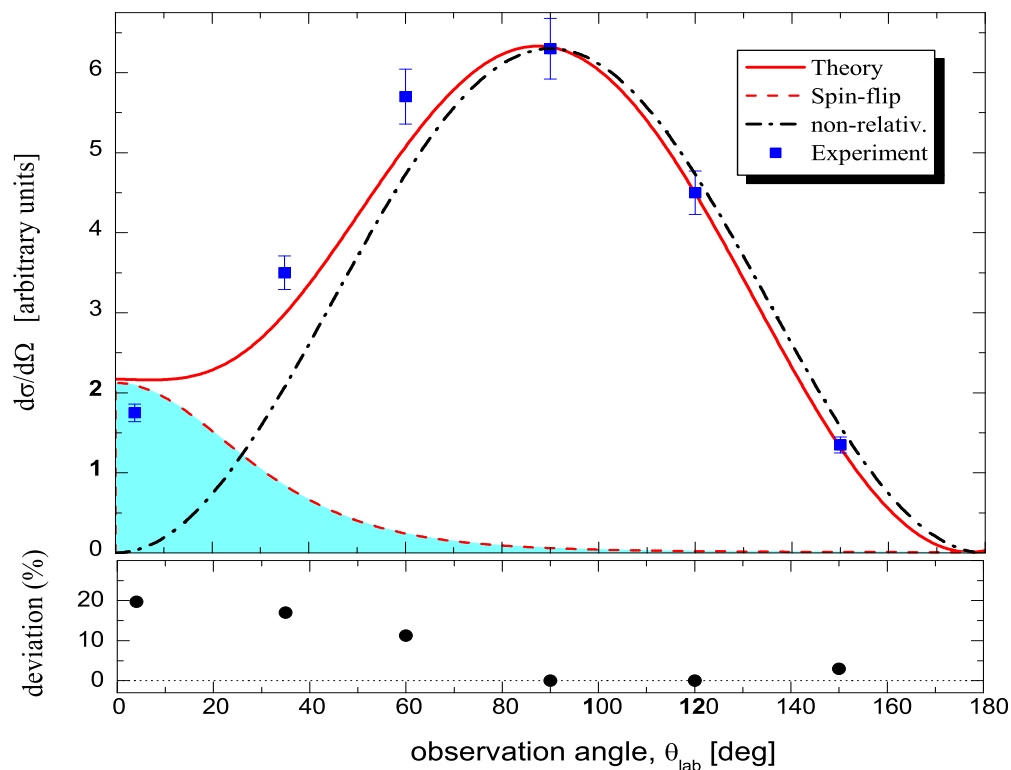


Figure 5.4: K-REC differential cross section for  $220 \text{ MeV}/u \text{ U}^{91+}$  colliding with  $N_2$  gas target as a function of the observation angle. The solid line refers to the complete relativistic calculations [18, 48].

### 5.2.3 Differential K-REC Cross Sections

For the direct electron capture into the K-shell of the H-like uranium ions measured at the same projectile energy,  $220 \text{ MeV}/u$ , impinging upon  $N_2$  target, the angle-differential cross section shows a dependence on the observation angle which deviates from the non-relativistic theoretical prediction ( $\sin^2\theta_{lab}$ -dependence). The full relativistic calculation, performed using the model proposed by Eichler and Ichihara [18] and improved by Fritzsche [48], shows a good

reproduction of the measured experimental data. This comparison is shown in the figure 5.4: *The solid line* represents the full relativistic calculation, *the dashed-dot line* refers to the non-relativistic prediction ( $\sin^2\theta_{lab}$ -distribution) and *the full squares* are the experimental points measured in the present work. In order to facilitate a comparison of experimental and theoretical cross section, the data were normalized to the theoretical prediction at  $90^\circ$ . The percentage error of the experimental data from the relativistic predictions as represented in the figure 5.4 bottom,  $([\frac{d\sigma}{d\Omega}]_{exp} - [\frac{d\sigma}{d\Omega}]_{theor}) / [\frac{d\sigma}{d\Omega}]_{theor}$ , is as high as 20 % especially at the forward angles. Also, due to the Lorentz transformation from the emitter frame to the laboratory frame, both the experimental data and the theoretical calculation, became almost symmetric around  $90^\circ$ . The increase in the differential cross section of the K-REC into the H-like uranium ions can be accounted for by considering the occurrence of the magnetic transitions due to the electron spin-flip. Therefore, the measurement of the K-REC transition at small angles, down to  $0^\circ$ , provides an unambiguous identification of spin-flip transitions occurring in relativistic ion-atom collisions.

In the figure 5.5, the deviation of the experimental differential cross section for the K-REC transition in 88 MeV/u bare uranium ions (*solid circles*) [88], 307 MeV/u bare uranium ions (*open circles*) and 220 MeV/u H-like uranium ions (*solid squares*) from the  $\sin^2\theta_{lab}$ -distribution are represented as a function of the observation angle. For forward observation angles smaller than  $60^\circ$ , a large deviation is observed. The value of the deviation seems to be strongly dependent on the projectile energy; higher the projectile energy, higher the measured cross section values. For angles larger than  $60^\circ$ , the energy dependence is reduced.

Therefore, one can conclude that the relativistic treatment of the K-REC transition yields provides a good approach for the spin-flip transition close to  $0^\circ$ . This originates from the magnetic field produced by the relativistic motion of the projectile ions. The magnetic contribution to this transition is strongly energy-dependent.

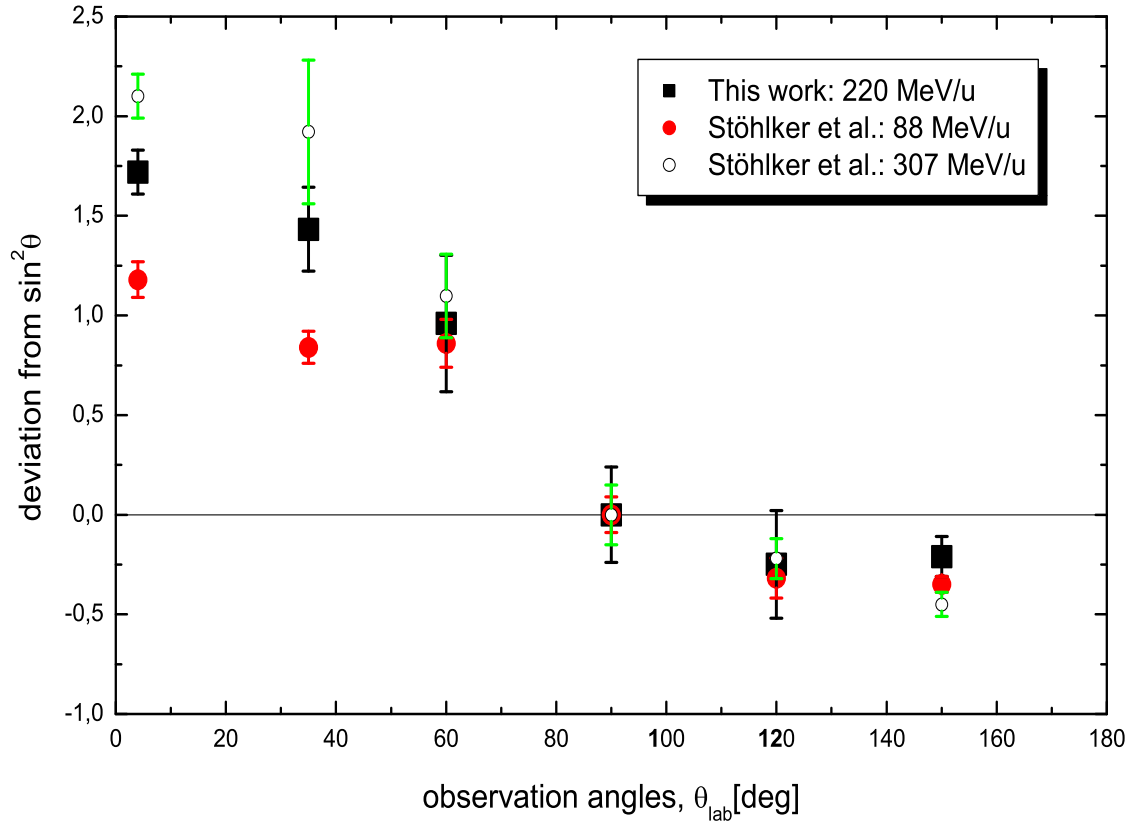


Figure 5.5: Deviations from the  $\sin^2\theta$  distribution for the K-REC transition intensities measured in: 88 MeV/u  $U^{92+}$  (solid circles)[88], 307 MeV/u  $U^{92+}$  (open circles)[89] and 220 MeV/u  $U^{91+}$  (solid squares) colliding with nitrogen target.

### 5.3 Simultaneous ionization and excitation in the $U^{90+} \rightarrow Xe$ collisions

The experimental relative cross sections for simultaneous ionization and excitation into the different total angular momentum states of the L-shell have been directly determined from the observed yields of the  $Ly_{\alpha 1}$  and  $Ly_{\alpha 2}$  radiation of the projectile. Experimental cross section ratios for excitation into the  $n = 2$  states of H-like uranium ions, following the collision of He-like uranium ions at  $220 \text{ MeV}/u$  with  $Xe$  gas target, as a function of observation angles are presented in figure 5.6.

As explained in chapter two, for the description of simultaneous excitation and ionization process, the approximation of the individual single electron processes was used. The ionization process was treated using the semi-classical approximation in which the magnetic part of the interaction potential was neglected, whereas for the case of projectile excitation, the fully relativistic approach has been used. In this model, the magnetic part of the interaction potential was included such that it was added coherently with the electric part of the interaction potential. This leads to a destructive interference resulting in a reduction of the total excitation cross section, as compared to the quasi-relativistic approach in which the electric and magnetic parts of the interaction potential are added incoherently. This approach seems to be well supported by the present experimental data (*see figure 5.6*).

Using the experimental angular distribution of the  $Ly_{\alpha 1}$  transition (*see figure 5.6*), it is possible to investigate the impact parameter characteristics of the simultaneous ionization and excitation process. This investigation can be done by the value of the alignment parameter  $A_{20}$ . The value of the alignment parameter  $A_{20}$  was deduced by a least square fit of equation 2.31 to the experimental data including all required relativistic transformations. The best fit to the experimental data for the yield ratio  $Ly_{\alpha 1}$  is shown in the figure 5.6. From the  $Ly_{\alpha 1}$  transition following the excitation of one K-shell electron of the initially He-like ions, via the simultaneous ionization and excitation process, the extracted alignment parameter value is  $A_{20} = -0.201 \pm 0.03$ . The experimental anisotropy parameter has large negative value which reflects the

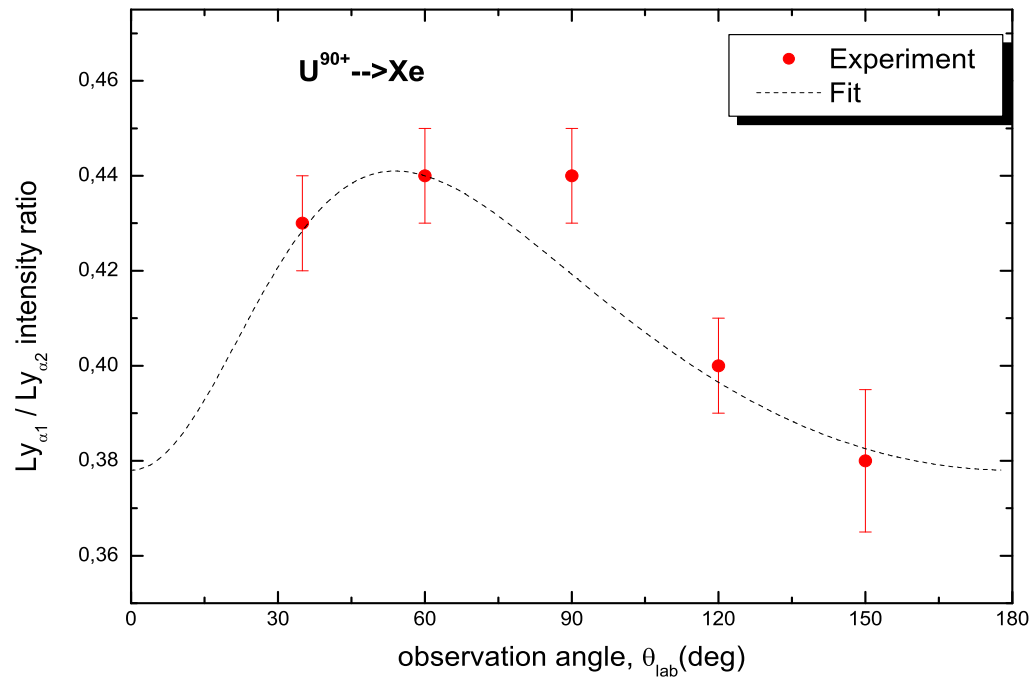


Figure 5.6: The relative cross section of the simultaneous ionization and excitation for  $U^{90+}$  (220 MeV/u)  $\rightarrow$  Xe collisions is represented by the  $Ly_{\alpha 1} / Ly_{\alpha 2}$  intensity ratio. The dashed line refers to a least square fit of equation 2.31.

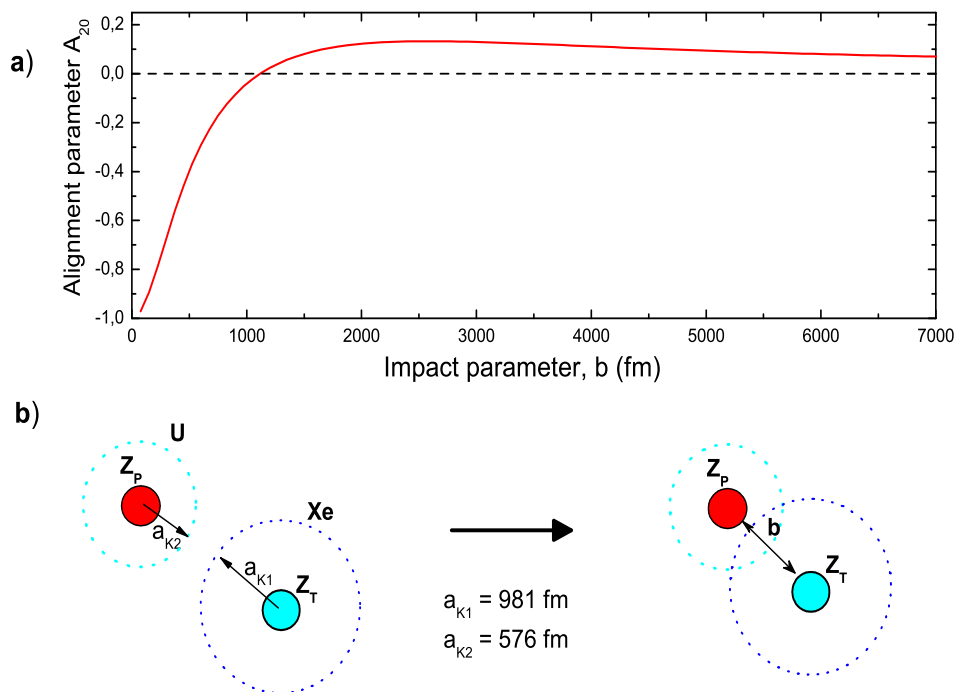


Figure 5.7: (a) Degree of alignment versus impact parameter for the  $2p_{3/2}$  state [39]. The Bohr radius  $a_{k_i}$  for the Uranium and Xenon atoms is shown in figure (b), where  $Z_P$  and  $Z_T$  represent the atomic number for the projectile (Uranium) and the target (Xenon), respectively.

nonstatistical population of magnetic sub-states of the  $2p_{3/2}$  level.

The dependence of the alignment parameter on the collision impact parameter, as calculated in [39], is shown in figure 5.7a. From the dependence of the alignment parameter  $A_{20}$  on the collision impact parameter  $b$ , theoretically calculated by Ludziejewski [39] for the  $2p_{3/2}$  level of uranium, it is possible to estimate the impact parameter range for the simultaneous ionization and excitation process ( $b^{exp} = 810$  fm). A good agreement between the experiment and the theory in which the collision occurs only at small impact parameter. This allows for conclusion that the experimental results confirm the theoretical predictions for the validity of first-order perturbation theory at relativistic energies.

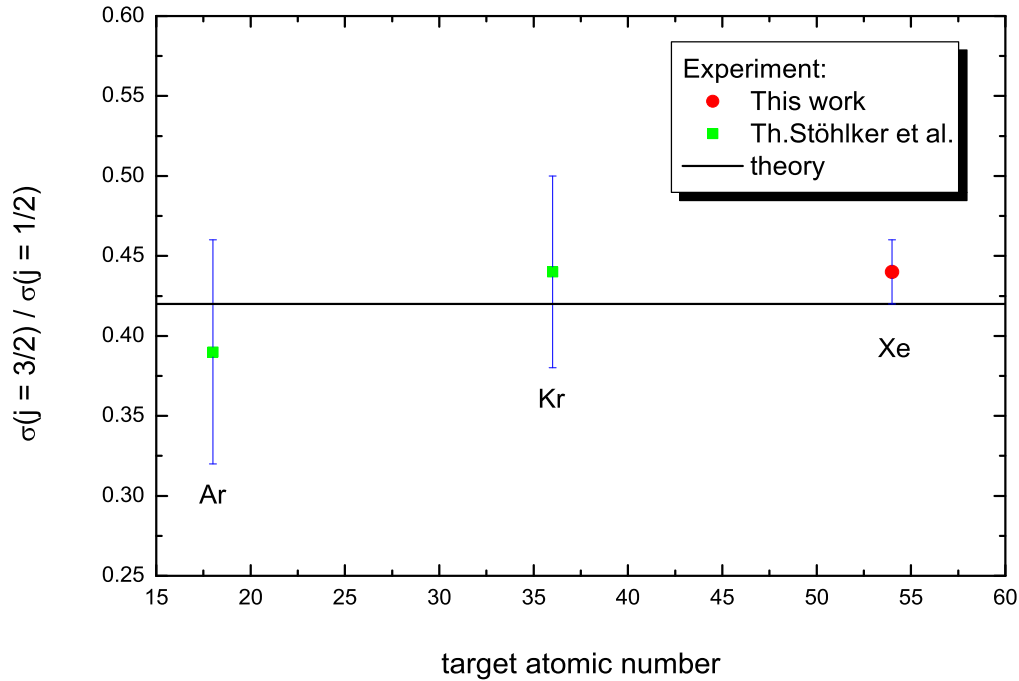


Figure 5.8: Experimental cross section ratios for the population of  $j = 1/2$  and  $j = 3/2$  by the excitation-ionization process of He-like ions. The solid squares and circle represent experimental results of Stöhlker et al [39] and the current work, respectively.

A comparison of the cross section ratios for the simultaneous excitation and ionization of He-like uranium ions colliding with Argon, Krypton and Xenon gas targets, at an incident energy of  $220 \text{ MeV}/u$ , is shown in the figure 5.8. For all these gas targets, the experimental results are in a good agreement with the theory. For the case of the xenon gas target used in the present work (*full circle*), the result has an accuracy of 2.3 %, better than the previous experiments where, due to a poor counting statistics the accuracy was 20 % [39]. For the case of Ar and Kr gas targets (*full squares*), the previously obtained accuracies are 7 % and 5 %, respectively. However, for all targets considered, it can be concluded that the good agreement between the experiment and the theory is due to the validity of the first-order perturbation theory for this energy-target



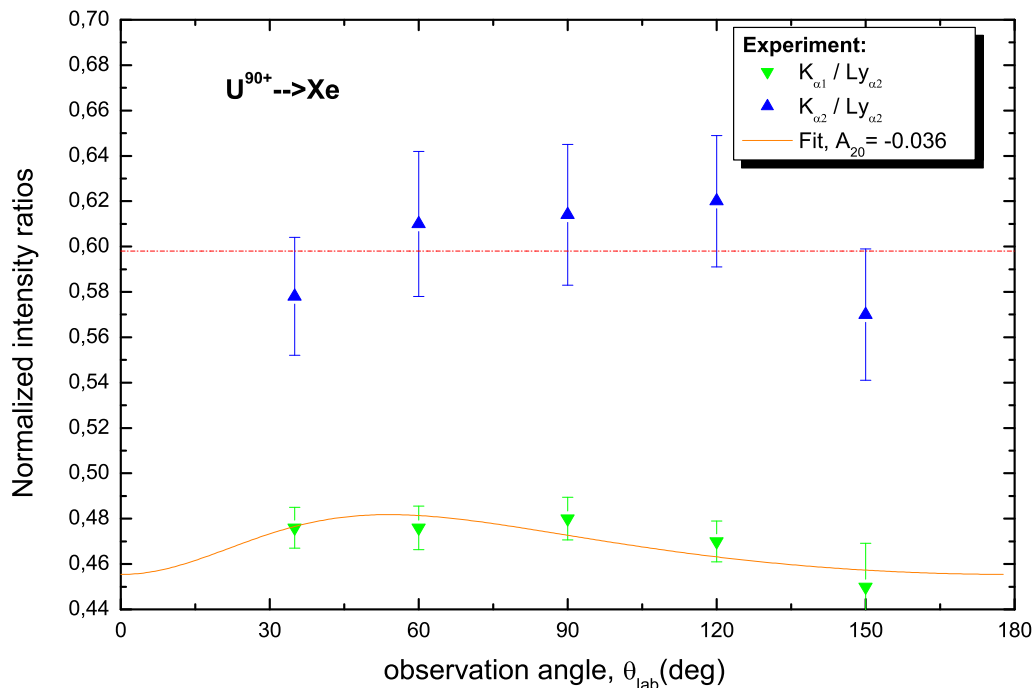


Figure 5.9: The intensities of  $K_{\alpha 1}$  (down-triangles) and  $K_{\alpha 2}$  (up-triangles) normalized to the  $Ly_{\alpha 2}$  line, for the  $U^{90+}$  ( $220 \text{ MeV}/u$ )  $\rightarrow Xe$  collisions, as a function of the observation angle.

atomic number regime.

The experimental angular dependence of the  $K_{\alpha}$  transitions for the excitation of the He-like uranium ions is shown in the figure 5.9. Considering the population of the  $n = 2$  state by the direct electron excitation mechanism in He-like uranium ions, for the  $K_{\alpha 1}$  transition, a value of  $-0.036 \pm 0.015$  for the alignment parameter  $A_{20}$  was obtained. This agrees with the theoretical alignment parameter which has a small negative value ( $-0.034$ ) [39]. This indicates that almost no alignment is observed and therefore the magnetic sub-states are statistically populated. As seen from the angular distribution of the emitted photons from the different transitions permit to obtain the information about the population mechanism of the decay levels by different excitation processes.



# Chapter 6

## Summary and Outlook

This work reports on the study of the projectile x-ray emission in relativistic ion-atom collisions. Excitation of K-shell in He-like uranium ions, electron capture into H-like uranium ions and Simultaneous ionization and excitation of initially He-like uranium ions have been studied using the experimental storage ring at GSI.

Information about the population of the excited states for the H- and He-like uranium ions, can be obtained by measuring the angular distribution of the decay radiation. Since the  $Ly_{\alpha 2}$  transition is isotropic, the intensities of the  $Ly_{\alpha 1}$  and  $K_{\alpha}$  transitions were normalized to the  $Ly_{\alpha 2}$  line. For the  $K_{\alpha 1}$  and  $K_{\alpha 2}$  transitions originating from the excitation of the He-like uranium ions, no alignment was observed (*see figure 5.9*). In contrast, the  $Ly_{\alpha 1}$  radiation from the simultaneous ionization-excitation process of the He-like uranium ions shows a clear alignment (*see figure 5.6*). It is shown that the alignment of  $Ly_{\alpha 1}$  was obtained by the Alignment parameter  $A_{20}$  which was found to be  $-0.201 \pm 0.03$ . The experimental value leads to the inclusion of a magnetic term in the interaction potential. It is interesting to note that in the case of the  $Ly_{\alpha 1}$  emission the small  $M2$  contribution added coherently to the  $E1$  transition amplitudes enhances the anisotropy.

The capture process of target electrons into the highly-charged heavy ions was studied using H-like uranium ions at an incident energy of  $220 \text{ MeV}/u$ , impinging on  $N_2$  gas-target. It was shown that, the strongly aligned electrons captured in  $2p_{3/2}$  level will couple with the available  $1s_{1/2}$  electron which

shows no initial directional preference. The magnetic sub-state population of the  $2p_{3/2}$  electron will be redistributed according to the coupling rules to the magnetic sub-states of the relevant two-electron states. Consequently, the  $^1P_1$  and  $^3P_2$  states are corresponding to the the strongly aligned  $2p_{3/2}$  state. This leads to the large anisotropy in the corresponding individual ground state transitions contributing to the  $K_{\alpha 1}$  emission (*see figure 2.11*). Due to the fact that the  $^1P_1 \rightarrow ^1S_0$  and  $^3P_2 \rightarrow ^1S_0$  transitions are experimentally *not resolved*, a more detailed analysis of the angular dependence of the  $K_{\alpha 1}$  radiation is required. From the  $K_{\alpha 1}/K_{\alpha 2}$  ratio (*see figure 5.2*), the current results show that the incoherent addition of the  $E1$  and  $M2$  transition components yield to an almost isotropic emission of the total  $K_{\alpha 1}$ . In contrast to the radiative electron capture, the experimental results for the K-shell single excitation of He-like uranium ions indicate that only the  $^1P_1$  level contributes to the  $K_{\alpha 1}$  transition (*see figure 5.1*). For this case, the anisotropy parameter  $\beta_{20}$  was found to be  $-0.20 \pm 0.03$  which is similar to that one calculated for pure  $E1$  transition [53].

Additional information about the nature of the radiative electron capture process at relativistic energy was obtained from the study of the angular distribution of the photon emission. For the direct electron capture into K-shell, the measured shape of the distribution deviates from the non-relativistic dipole-approximation predictions,  $\sin^2\theta$ -shape (*see figure 5.4*). This indicates the existence of a spin-flip transition occurring in relativistic ion-atom collisions, at forward angles. The experimental observation is supported by the theoretical predictions performed by Ichihara et. al [45, 46] and Fritzsche et. al [48]. On the theoretical side, the calculation of REC angular distribution has been carried out up to energies of  $10 \text{ GeV}/u$ . To verify the validity of these predictions, further experiments on the radiative electron capture in H-like uranium ions at  $500 \text{ MeV}/u$  and  $1 \text{ GeV}/u$  are planned at the GSI.

This work also reports on the study of a two-electron process: the simultaneous ionization and excitation occurring in relativistic collisions of heavy highly-charged ions with gaseous targets. The investigation was performed on He-like uranium ions impinging upon xenon gas-target at an incident energy of  $220 \text{ MeV}/u$ . The measurements have been performed at the ESR gas-target

---

using atomic xenon with a typical area density of  $10^{12}$  *particles/cm*<sup>2</sup>. In contrast to the solid state target, the use of gas target offers the advantage of clear separation of the one step two-electron process due to the fact that the probability of two consecutive collision in such thin targets is negligible and the double step processes can be excluded. During the process of simultaneous ionization and excitation in He-like uranium ions, one of the ground-state electrons is promoted into the continuum and the other into the L-subshell states of the projectile. To select this process, the Lyman-series ( $Ly_{\alpha}$ ) radiation has been measured at various observation angles in coincidence with up-charged projectiles ( $U^{91+}$ ), *see figure 4.9a*. From the yields of the  $Ly_{\alpha 1}$  and  $Ly_{\alpha 2}$  projectile radiation, the relative cross section for the process of simultaneous ionization and excitation was directly determined (*see figure 5.6*). The angle dependent measurement of the radiation yields provide information about the angular distributions of the emitted radiation and permits the determination of the alignment parameter  $A_{20}$ . This parameter gives information on the level population and the collision impact parameter [39]. The present results ( $b^{exp} = 810$  *fm*) show that the simultaneous ionization and excitation is a process which occurs at small impact parameter.



# Chapter 7

## Zusammenfassung

In der vorliegenden Arbeit wurde die Röntgen-Strahlung von H- und He-artigen Uranionen ( $U^{91+}$  and  $U^{90+}$ ) in relativistischen Ion-Atom-Stößen mit dem Ziel untersucht, den Einfluss relativistischer Effekte auf die Struktur einfacher Mehrteilchensysteme und die Dynamik elementarer atomarer Prozesse zu studieren. Hierbei wird die große Feinstrukturaufspaltung, wie sie in diesen sehr schweren Ionen vorliegt, ausgenutzt (L-Schale von Uran; ca.  $4.5 \text{ keV}$ ), um detaillierte, zustandsspezifische Informationen über elementare Wechselwirkungsprozesse zu erhalten. Aufgrund der Aufspaltung der K-Schalen-Röntgenübergänge in ihre Feinstrukturkomponenten ( $Ly_{\alpha 1}$  und  $Ly_{\alpha 2}$  für H-artiges Uran;  $K_{\alpha 1}$  und  $K_{\alpha 2}$  für He-artiges Uran) ist es nun möglich, selbst die Emissionscharakteristik (Winkelverteilung) für die individuellen Röntgenlinien zu vermessen. Eine mögliche Anisotropie der Strahlung ist Folge einer nicht-statistischen Bevölkerung der magnetischen Unterezustände (Alignment) und erlaubt eine äußerst präzise Überprüfung theoretischer Modelle. Dies war der zentrale Gegenstand meiner durchgeführten experimentellen Studien. Im Konkreten wurden hierzu Experimente für die folgende Prozesse durchgeführt: Elektronentransfer vom Target in das Projektil, Coulomb-Anregung der K-Schalenelektronen des Projektils wie auch K-Schalen Coulomb-Anregung bei gleichzeitiger K-Schalenionisation sowie der direkte radiative Elektroneneinfang in die K-Schale.

Die Experimente fanden am Gastarget des Experimentier Speicherrings (ESR) am GSI Helmholtzzentrum für Schwerionenforschung statt (Abb. 3.1

und 3.6), wobei die Energie der Ionen  $220 \text{ MeV/u}$  betrug (ca. 50% Lichtgeschwindigkeit). Die Energie ergab sich aus der Forderung, dass nach dem Durchgang der Ionenstrahlen durch eine Stripperfolie ausreichend Intensität für H- und He-artige Ionen garantiert sein muss. Für die verwendeten Gasarten  $N_2$  und  $Xe$  wurde das Target mit nur geringen Dichten von ca.  $10^{12}$  Teilchen/cm<sup>3</sup> (Durchmesser des Gasjets:  $5 \text{ mm}$ ) betrieben, um Einzelstoßbedingung zu garantieren. Die nach der Wechselwirkung mit dem Target emittierte Projektilstrahlung wurde mittels mehrerer an der Targetkammer aufgebauter Germanium Detektoren (Abbildung 3.8 und Tabelle 3.3) nachgewiesen. Die Detektoren waren hierzu vom Vakuum des ESR durch dünne Be- bzw. Edelstahlfenster getrennt. Zudem wurde der Landungszustand der Projektile nach Durchgang durch die Wechselwirkungszone des Targets analysiert (z. B. Abbildung 4.7 und 4.9). Die hierfür eingesetzten Teilchendetektoren ermöglichten zudem den koinzidenten aber auch anti-koinzidenten Nachweis der Projektilstrahlung mit dem Endladungszustand. Aus den so gewonnenen Daten wurde, unter Berücksichtigung der Nachweiseffizienz und der relativistischen Dopplerkorrektur für die individuellen Röntgendetektoren, die relative Ausbeute für die charakteristische Projektilstrahlungen (feinstrukturaufgelöste L-K Übergänge) und für den radiativen Elektroneneinfang gewonnen.

Der wesentliche Befund der Experimente ist eine ausgeprägte Abhängigkeit der Winkelverteilung der  $Ly_{\alpha 1}$  und  $K_{\alpha 1}$ -Strahlung in Abhängigkeit von den unterschiedlichen Bevölkerungsmechanismen (diese Daten wurden für Stöße mit  $N_2$  gewonnen). Auch sei hier angemerkt, dass in dieser Arbeit nur anisotrope Verteilungen nachgewiesen wurden, die durch einem negativen Alignment Parameter beschrieben werden. D.h. falls es in solch hochenergetischen Stößen zu einer nicht-statistischen Besetzung der magnetischen Unterzustände kommt, so werden grundsätzlich die Zustände mit kleinen absoluten magnetischen Quantenzahlen bevorzugt bevölkert.

Im Folgenden seien die gewonnenen experimentellen Resultate zur Emission von charakteristischer K-Strahlung, die für die Ein-Elektronenprozesse (Eingang und Anregung) gewonnen wurden, zusammengefasst:

- Elektroneneinfang in nacktes Uran (Zerfall von Zuständen im H-artigem Uran): Starke Anisotropie der  $Ly_{\alpha 1}/Ly_{\alpha 2}$  (dieses Ergebnis wurde bereits



in früheren Arbeiten der Arbeitsgruppe gefunden). Hier sei angemerkt, dass die  $Ly_{\alpha 2}$  ( $2s_{1/2}, 2p_{1/2} \rightarrow 1s_{1/2}$ ) Strahlung per Definition isotrope ist.

- Elektroneneinfang in H-artiges Uran (Zerfall von Zuständen im He-artigem Uran): Isotrope Winkelverteilung des  $K_{\alpha 1}/K_{\alpha 2}$ -Verhältnisses innerhalb der experimentellen Meßgenauigkeit.
- K-Schalen Coulomb-Anregung von H-artigem Uran (Zerfall von Zuständen im H-artigem Uran): Isotrope Winkelverteilung des  $Ly_{\alpha 1}/Ly_{\alpha 2}$ -Verhältnisses.
- K-Schalen Coulomb-Anregung von He-artigem Uran (Zerfall von Zuständen im He-artigem Uran): Starke-Anisotropie der Winkelverteilung des  $K_{\alpha 1}/K_{\alpha 2}$ -Verhältnisses.

Offensichtlich weisen diese Befunde darauf hin, dass sowohl für den Elektroneneinfang wie auch für die Anregung, die Anwesenheit eines weiteren Elektrons (H-artig im Fall des Einfangs, He-artig im Fall der Anregung) einen entscheidenden Einfluss auf die Emissionscharakteristik hat. Tatsächlich konnten für den Fall des Elektroneneinfangs die gefundenen Resultate durch neueste theoretische Arbeiten von Surzhykov et al. erklärt werden. Hierbei ist es wesentlich darauf hinzuweisen, dass sich im Falle der  $K_{\alpha 1}$  Strahlung zwei Röntgenübergänge überlagern ( $[1s_{1/2}, 2p_{1/2}] \ ^1P_1$  und  $[1s_{1/2}, 2p_{3/2}] \ ^3P_2$ ). Diese können experimentell nicht aufgelöst werden. Die theoretische Behandlung zeigt nun, dass beide Zustände nahezu mit gleicher Stärke besetzt werden, jedoch der Zerfall des  $^3P_2$  Zustands durch eine Winkelverteilung beschrieben wird (M2-Strahlung), die invers zu der des  $^1P_1$  ist (E1-Strahlung). Dies bedeutet, dass während der  $^1P_1$  im Emittersystem ein Maximum unter 90 Grad aufweist, zeigt hier die Verteilung des  $^3P_2$  Zustands ein Minimum. Somit kommt es so zufällig zu der beobachteten Isotropie der  $K_{\alpha 1}$  Strahlung und des  $K_{\alpha 1}/K_{\alpha 2}$  Verhältnisses.

Diese Erkenntnisse werfen auch ein neues Licht auf die für den Prozess der Anregung gewonnen Daten. Für die H-artigen Ionen liegen bereits theoretische Beschreibungen vor, die in der Tat im Einklang mit den gemessenen Daten stehen. Für die Anregung He-artiger Ionen existiert jedoch bislang keine

adäquate theoretische Beschreibung. Jedoch deuten die experimentellen Befunde darauf hin, dass der Prozess der Coulomb-Anregung ein sehr zustandsselektiver Prozeß ist und hierdurch nur der  $^1P_1$  bevölkert werden kann. Dieser kann direkt durch Dipolanregung erreicht werden, während die Anregung des  $^3P_2$  Niveaus einen Spinflip erfordert. Selbst für den hier vorliegenden Fall von Uran als Projektil und der moderaten relativistischen Stoßgeschwindigkeit, ist die Wahrscheinlichkeit für solche Anregungsmoden sehr gering. In der Tat stimmt auch die Form der gemessenen Winkelverteilung sehr gut mit die Annahme überein, dass wir es hier nur mit der Besetzung des  $^1P_1$  zu tun haben. Trotzdem ist es nicht geklärt, warum für H-artiges Uran die Anregung des  $2p_{3/2}$  Zustands zu einer isotropen Winkelverteilung führt, während die Winkelverteilung als Folge der Anregung in das  $^1P_1$  Niveau im He-artigen Uran eine starke Anisotropie aufweist. Die Klärung dieses Befunds erfordert eingehende theoretische Untersuchungen.

Zudem wurde im Rahmen dieser Arbeit auch der Zweielektronen-Prozess der Anregung bei gleichzeitiger Ionisation für den Fall von He-ähnlichem Uran untersucht (ein Prozess zweiter Ordnung). Die Messungen wurden erneut bei  $220 \text{ MeV}/u$  aber in Kombination mit einem Xe-Gastarget durchgeführt. Bei der Coulomb-Anregung bei simultaner Ionisation wird ein Elektron in das Kontinuum ionisiert während das Andere gleichzeitig in einen angeregten Zustand angehoben wird. Die hier vorgenommene Interpretation dieses Effektes beruht auf der Annahme, dass beide Prozesse zwar gleichzeitig aber unabhängig voneinander stattfinden. Zur Interpretation wurden deshalb beide Prozesse im Rahmen der semiklassischen Näherung berechnet (SCA). Hierdurch lassen sich sowohl Ionisation wie auch Anregung unter Annahme klassischer Trajektorien und unter Verwendung relativistischer Wellenfunktionen beschreiben. Qualitativ zeigen bereits diese Rechnungen, dass dieser Prozess insbesondere sensitiv auf kleine Stoßparameter ist.

Das gemessene Resultat für das Alignment der  $Ly_{\alpha 1}$ -Strahlung befindet sich in qualitativer Übereinstimmung mit der theoretischen Näherung. Insbesondere zeigt die Dominanz der  $Ly_{\alpha 2}$  Strahlung, dass in der Tat die Anregung in s-Zustände überwiegt, d.h. bei kleinen Stoßparametern dominiert die Monopolanregung, was sich auch im Einklang mit dem theoretischen Model

befindet.

Schließlich wurde auch der Prozeß des strahlenden Elektroneneinfangs (REC) untersucht, der vor allem zum Konsistenztest für die bereits diskutierten Daten dient. Zu diesem Prozeß liegen bereits viele Daten aus früheren Messungen der Arbeitsgruppe vor. In Bezug auf die Winkelverteilung für diesen Prozeß ist zu vermerken, dass im Rahmen der nichtrelativistischen Näherung aber unter Berücksichtigung aller Multipolordnungen (Retardierung) es zu einer vollständigen, gegenseitigen Aufhebung der Retardierung und der Lorentz-Transformation kommt und die  $\sin^2\theta$ -Abhängigkeit, wie man sie im Rahmen der nichtrelativistischen Dipolnäherung erwartet, erhalten bleibt. Somit sind Abweichungen von der  $\sin^2\theta$ -Abhängigkeit ein Maß für relativistische Effekte, also insbesondere für die Kopplung des magnetischen Moments des Elektrons mit dem dynamischen elektromagnetischen Feld des Projektils. D.h. hier treten magnetische Übergängen auf. In der Tat zeigen auch die hier nachgewiesenen winkeldifferenziellen Wirkungsquerschnitte für den REC in die K-Schale eine Winkelabhängigkeit, die von der nicht-relativistischen theoretischen Vorhersage abweicht (Abb. 5.4). Vollrelativistische Rechnungen von Eichler und Ichihara [18] sowie von Fritzsche [48] zeigen eine gute Übereinstimmung mit den in dieser Arbeit gewonnenen Daten. Der Anstieg des K-REC Wirkungsquerschnitts bei kleinen Emissionswinkeln kann durch die Berücksichtigung magnetischer Übergänge erklärt werden. Die Schlussfolgerung dieser Interpretation ist, dass durch Messung des K-REC Übergangs bei kleinen Beobachtungswinkeln, nahe Null, eindeutig auf den Beitrag magnetischer Übergänge zum Prozess des REC geschlossen werden kann.



# List of Figures

2.1	The classical trajectory of a particle in the laboratory system, defined by the impact parameter $\mathbf{b}$ and the scattering angle $\theta$ . . . . .	9
2.2	The coordinate systems, laboratory and emitter frames, for a collision between two atoms: the target and $Z_T$ the projectile $Z_P$ [28]. . . . .	10
2.3	Polar diagrams for the angular dependence of the electric field strength produced by a point charge moving with the velocity $v$ to the right. . . . .	12
2.4	Calculated probabilities for excitation and ionization in hydrogen like uranium ions and excitation-ionization processes helium like uranium ions, plotted versus collision impact parameter [39]. For further explanation see the text. . . . .	15
2.5	Radiative recombination can be viewed as time-reversed photoionization: an electron is captured into a bound state of the ion with simultaneous emission of a photon. . . . .	17
2.6	Schematic representation of the REC and NRC processes. The electron is captured from a bound state of the target atom into the K-shell of the projectile with the emission of a K-REC photon (A), or no photon emission (C). The electron capture into the L-shell is followed by the decay in the ground state resulting in a photon emission of energy $\hbar\omega_{K\alpha}$ (B and D). . . . .	20

2.7	(a) The total electron capture cross section dependence on projectile energy for bare uranium ions on $N_2$ [43]. (b) The total electron capture cross section dependence on target nuclear charge $Z_T$ for bare uranium ions at $300 \text{ MeV}/u$ colliding with gaseous targets $N_2$ and $Ar$ (solid squares) and with solid targets $Be$ and $C$ (solid circles) [27, 43]. The dashed line represents the eikonal approach [27] for the NRC process. The dotted line shows the prediction obtained for REC within the dipole approximation. The solid line represents the sum of both predictions. . . . .	22
2.8	Schematic illustration of the photon angular distribution for REC in the projectile and laboratory frame. . . . .	24
2.9	Angle-differential REC cross sections for electron capture into the K-shell of uranium ions at $220 \text{ MeV}/u$ . The solid line refers to complete relativistic calculations and shaded area to the spin-flip contributions. The dashed line represents the non-relativistic theory for dipole approximation [48]. . . . .	25
2.10	Level diagram for H- and He-like U. Multipolarities for the most probable decay modes are indicated by solid arrows, weaker decay modes are shown as dashed arrows. . . . .	27
2.11	The angular distribution of the $K_{\alpha 1}$ decay in (a) the laboratory and (b) the emitter systems, for initially H-like uranium ions at $220 \text{ MeV}/u$ . Additionally, the angular distributions for the electric and magnetic components of the decay are displayed [55]. . . . .	30
3.1	Layout of the accelerator facility and experimental areas at GSI. . . . .	32
3.2	Layout of the Experimental Storage Ring (ESR) at GSI. The positions of the e-cooler and the internal jet-target are marked. . . . .	35
3.3	Layout of the electron cooler device used at the storage ring ESR. . . . .	36
3.4	Schottky frequency spectrum for a circulating beam of $U^{92+}$ ions at $295 \text{ MeV}/u$ . The broad distribution refers to the non-cooled beam, measured directly after injection into the ESR. The narrow distribution reflects the momentum profile of a continuously cooled ion beam. . . . .	38
3.5	The effective number of stored particles per second available for experiments in ESR. The average over a time cycle of 1 day is displayed [41]. . . . .	39
3.6	Schematic representation of the ESR internal gas-jet target [69, 70]. . . . .	40

3.7	Principle of the charge exchange experiments at the internal jet target of the ESR illustrated for the case of H-like ions primary beam. Up-charged ( $Q + 1$ ) and down-charged ( $Q - 1$ ) ions are separated from the primary beam and detected by particle detectors. . . . .	42
3.8	Layout of the experimental arrangement at the ESR jet-target. Photon emission is observed in coincidence with the up- or down-charged ions, detected by a particle counter placed behind the dipole magnets. . . . .	43
3.9	The Ge(i) detectors used in the experiment. . . . .	44
3.10	Block diagram of the electronics and data acquisition used in this work. . .	46
4.1	Relativistic transformation of the transition energy from the emitter frame moving with a reduced velocity of $\beta \approx 0.6$ ( $220 \text{ MeV}/u$ ) in the laboratory frame as a function of observation angle. . . . .	50
4.2	Doppler broadening for the transition in H-like uranium ions as calculated from the equation 4.2: (a) without collimator ( $\Delta\theta = 3.5^\circ$ ), and (b) with the collimator ( $\Delta\theta = 0.2^\circ$ ). . . . .	50
4.3	Total linear attenuation coefficients plotted as a function of photon energy for germanium, beryllium and lead [72]. . . . .	54
4.4	The source-detector geometry. . . . .	56
4.5	Absolute detector efficiency versus photon energy for the germanium detectors used in the present work and placed at: at $35^\circ$ (A), $60^\circ$ (B), and $90^\circ$ , $120^\circ$ and $150^\circ$ (C). . . . .	60
4.6	X-ray energy spectrum as observed by the germanium detector at $35^\circ$ . . .	61
4.7	The photon-particle coincidence time spectrum. The x-ray detector was placed at $35^\circ$ ( <i>for details see the text</i> ). . . . .	63
4.8	X-ray energy spectrum for H-like uranium. The spectrum was measured, at $35^\circ$ , in coincidence with up-charged uranium ions. The filled spectrum corresponds to random events from the time spectrum. The inset displays the resolved Lyman transitions. . . . .	63
4.9	X-ray energy spectra, for $220 \text{ MeV}/u \text{ U}^{90+}$ ions colliding with $\text{Xe}$ gas target, as observed by the germanium detector at $35^\circ$ . . . . .	64

4.10	The x-ray spectra recorded at $60^\circ$ , $90^\circ$ , $120^\circ$ and $150^\circ$ for initially He-like uranium ions colliding with Xe gas-target atoms at an energy of $220 \text{ MeV}/u$ . The $K_\alpha$ transitions are connected to single excitation and the $Ly_\alpha$ lines were recorded in coincidence with the up-charged H-like uranium ion. . . . .	66
4.11	Projectile X-ray spectra for $220 \text{ MeV}/u \text{ U}^{90+} \rightarrow N_2$ collision measured (a) without coincidence requirement (total emission spectra), (b) in coincidence with down-charged projectile ( $\text{U}^{89+}$ ). . . . .	68
4.12	X-ray spectrum recorded for initially H-like uranium ions colliding with nitrogen gas target. The inset represents the ground-state x-ray transitions for H- and He-like ions. . . . .	69
4.13	X-ray spectrum associated with electron capture into the $220 \text{ MeV}/u \text{ U}^{91+}$ ions colliding with $N_2$ -target, as observed at $35^\circ$ . . . . .	71
4.14	Coincidence time spectrum between the x-rays emitted at $35^\circ$ and $\text{U}^{90+}$ ions. . . . .	71
4.15	Ground state X-ray transitions measured at $35^\circ$ . The upper plot represents raw data, the middle represent spectrum accumulated in coincidence with $\text{U}^{90+}$ ions and the lower spectrum represents the difference between the two spectra (a) and (b). . . . .	72
4.16	X-ray energy spectrum measured in coincidence with $\text{U}^{90+}$ , as observed at $120^\circ$ . . . . .	73
5.1	Angular distribution of the $K_{\alpha 1}/K_{\alpha 2}$ intensity ratio, in the laboratory frame, as observed for K-shell excitation of He-like uranium ions colliding with $N_2$ gas target. The solid line depict the fit result to the experimental data using the equation 2.31. . . . .	76
5.2	Angular distribution of the $K_{\alpha 1}/K_{\alpha 2}$ intensity ratio as a function of the observation angle. The experimental data for $220 \text{ MeV}/u \text{ U}^{91+} \rightarrow N_2$ [55]. . . . .	77
5.3	The experimental intensities of $Ly_{\alpha 1}$ , $K_{\alpha 1}$ and $K_{\alpha 2}$ normalized to the $Ly_{\alpha 2}$ line. The experimental data were measured for $220 \text{ MeV}/u \text{ U}^{91+} \rightarrow N_2$ collisions. The solid lines refer to the corresponding mean values and the dashed lines give the associated uncertainties. . . . .	79
5.4	K-REC differential cross section for $220 \text{ MeV}/u \text{ U}^{91+}$ colliding with $N_2$ gas target as a function of the observation angle. The solid line refers to the complete relativistic calculations [18, 48]. . . . .	80



- 5.5 Deviations from the  $\sin^2\theta$  distribution for the K-REC transition intensities measured in: 88 MeV/u  $U^{92+}$  (solid circles)[88], 307 MeV/u  $U^{92+}$  (open circles)[89] and 220 MeV/u  $U^{91+}$  (solid squares) colliding with nitrogen target. . . . . 82
- 5.6 The relative cross section of the simultaneous ionization and excitation for  $U^{90+}$  (220 MeV/u)  $\rightarrow Xe$  collisions is represented by the  $Ly_{\alpha 1}/Ly_{\alpha 2}$  intensity ratio. The dashed line refers to a least square fit of equation 2.31. 84
- 5.7 (a) Degree of alignment versus impact parameter for the  $2p_{3/2}$  state [39]. The Bohr radius  $a_{k_i}$  for the Uranium and Xenon atoms is shown in figure (b), where  $Z_P$  and  $Z_T$  represent the atomic number for the projectile (Uranium) and the target (Xenon), respectively. . . . . 85
- 5.8 Experimental cross section ratios for the population of  $j = 1/2$  and  $j = 3/2$  by the excitation-ionization process of He-like ions. The solid squares and circle represent experimental results of Stöhlker et al [39] and the current work, respectively. . . . . 86
- 5.9 The intensities of  $K_{\alpha 1}$  (down-triangles) and  $K_{\alpha 2}$  (up-triangles) normalized to the  $Ly_{\alpha 2}$  line, for the  $U^{90+}$  (220 MeV/u)  $\rightarrow Xe$  collisions, as a function of the observation angle. . . . . 87



# List of Tables

3.1	The major ESR parameters. . . . .	37
3.2	Estimated life times for different bare ions stored in the ESR. . . . .	37
3.3	Characteristics of the Germanium detectors used in the present experiment.	44
4.1	Most probable characteristic transitions for $U^{90+}$ and $U^{91+}$ . . . . .	48
4.2	Transition energies transformation from laboratory frame to the emitter frame. . . . .	49
4.3	Fit values for the parameters a and b describing the energy dependence of the photon attenuation coefficient ( <i>see equation 4.9</i> ). . . . .	54
4.4	The K-line energies and corresponding fluorescence coefficient for Ge. . . .	58
4.5	Detector geometry and collimator parameters (all values are in <i>mm</i> ). . . .	59
4.6	Energies of the x-ray emission lines from <i>Xe</i> and <i>Pb</i> (all values are in <i>keV</i> ) [85]. . . . .	62
4.7	Gaussian fit parameters for the $Ly_\alpha$ transitions detected at $35^\circ$ in coinci- dence with the $U^{91+}$ ions ( <i>all values are in keV</i> ). . . . .	65



# Bibliography

- [1] J. H. MCGUIRE, *Phys. Rev. A* **36**, 1166 (1987).
- [2] J. H. MCGUIRE, *Advances in Atomic, Molecular and Optical Physics* **29**, 217 (1992).
- [3] H. MERABET, R. BRUCH, S. FUELLING, M. BAILY, A. L. GODUNOV, J. H. MCGUIRE, and K. BARTSCHAT, *Nucl. Inst. and Meth. in Phys. Research B* **205**, 399 (2003).
- [4] A. GENSMANTEL, J. ULLRICH, R. DOERNER, and R. E. OLSON, *Phys. Rev. A* **45**, 4572 (1992).
- [5] R. E. OLSON, J. ULLRICH, R. DOERNER, and H. SCHMIDT-BÖCKING, *Phys. Rev. A* **40**, 2843 (1989).
- [6] R. DOERNER, J. ULLRICH, H. SCHMIDT-BÖCKING, and R. E. OLSON, *Phys. Rev. Lett. A* **36**, 147 (1989).
- [7] P. A. HAYES and J. F. WILLIAMS, *Phys. Rev. Lett.* **77**, 3098 (1996).
- [8] D. VERNHET, L. ADOUI, J. P. ROZET, K. WOHRER, A. CHETIOUI, A. CASSIMI, J. P. GRANDIN, J. M. RAMILLON, M. CORNILLE, and C. STEPHAN, *Phys. Rev. Lett.* **79**, 3625 (1997).
- [9] L. H. ANDERSEN, M. FROST, P. HVELPLUND, H. KNUDSEN, and S. DATZ, *Phys. Rev. Lett.* **52**, 518 (1984).
- [10] J. A. TANIS, E. M. BERNSTEIN, M. CLARK, W. G. GRAHAM, R. H. MCFARLAND, T. J. MORGAN, B. M. JOHNSON, K. W. JONES, and M. MERON, *Phys. Rev. A* **31**, 4040 (1985).

- 
- [11] N. STOLTERFOHT, C. C. HAVENER, R. A. PHANEUF, J. K. SWENSON, and S. M. S. F. W. MEYER, *Phys. Rev. Lett.* **57**, 74 (1986).
- [12] J. P. PEDERSEN and P. HVELPLUND, *Phys. Rev. Lett.* **62**, 2373 (1989).
- [13] S. SALEM, A. BRÄUNING-DEMIAN, R. DUNFORD, F. BOSCH, H. BRÄUNING, S. CHATTERJEE, S. HAGMANN, C. KOZHUHAROV, D. LIESEN, P. H. MOKLER, Z. STACHURA, and A. WARCZACK, *GSI Scientific Report 2005, Darmstadt, Germany*, 307.
- [14] P. H. MOKLER and T. STOEHLKER, *Advances in Atomic, Molecular and Optical Phys.* **37**, 297 (1996).
- [15] S. CHENG, H. G. BERRY, R. W. DUNFORD, D. S. GEMMELL, E. P. KANTER, C. KURTZ, K. E. REHM, and B. J. ZABRANSKY, *Phys. Rev. A* **50**, 2197 (1994).
- [16] T. STOEHLKER, A. GUMBERIDZE, G. BEDNARZ, F. BOSCH, S. FRITZSCHE, S. HAGMANN, D. C. IONESCU, C. KOZHUHAROV, A. KRÄMER, D. LIESEN, X. MA, R. MANN, P. H. MOKLER, D. SEIRPOWSKI, Z. STACHURA, M. STECK, and A. WARCZAK, *GSI Scientific Report 2000, Darmstadt, Germany*.
- [17] T. STOEHLKER, A. GUMBERIDZE, X. MA, H. F. BEYER, G. BEDNARZ, F. BOSCH, X. CAI, S. FRITZSCHE, S. HAGMANN, C. KOZHUHAROV, O. KLEPPER, D. LIESEN, P. H. MOKLER, D. SEIRPOWSKI, Z. STACHURA, M. STECK, A. SURZHYKOV, S. TOLEIKIS, A. WARCZAK, and Y. ZOU, *Hyperfine Interact.* **146-147**, 97 (2003).
- [18] J. EICHLER and W. E. MEYERHOF, "*Relativistic Atomic Collisions*", Academic Press San Diego, (1995).
- [19] T. STOEHLKER, F. BOSCH, A. GALLUS, C. KOZHUHAROV, G. MENZEL, P. H. MOKLER, H. T. PRINZ, J. EICHLER, A. ICHIHARA, T. SHIRAI, R. W. DUNFORD, T. LUDZIEJEWSKI, H. REICH, P. RYMUZA, Z. STACHURA, P. SWIAT, and A. WARCZAK, *Phys. Rev. Lett.* **79**, 3270 (1997).

- [20] A. GUMBERIDZE, T. STOEHLKER, G. BEDNARZ, F. BOSCH, S. FRITZSCHE, S. HAGMANN, D. C. IONESCU, O. KLEPPER, C. KOZHUHAROV, A. KRÄMER, D. LIESEN, X. MA, R. MANN, P. H. MOKLER, D. SIERPOWSKI, Z. STACHURA, M. STECK, S. TOLEIKIS, and A. WARCZACK, *Hyperfine Interact.* **146-147**, 133 (2003).
- [21] D. LIESEN, *Phys. Scripta* **36**, 723 (1987).
- [22] P. H. MOKLER, S. REUSCH, T. STOEHLKER, R. SCHUCH, M. SCHULZ, G. WINTERMEYER, Z. STACHURA, A. WARCZACK, A. MUELLER, Y. AWAYA, and T. KAMBARA, *Radiat. Eff. and Defects in solids* **110**, 39 (1989).
- [23] T. STOEHLKER, P. H. MOKLER, C. KOZHUHAROV, E. A. LIVINGSTON, and J. ULLRICH, *Nucl. Inst. and Meth. in Phys. Res. B* **56/57**, 86 (1991).
- [24] C. BRANDAU, *Nucl. Instrum. Methods Phys. Res. B* **205**, 66 (2003).
- [25] R. ANHOLT, *Phys. Rev. A* **31**, 3579 (1985).
- [26] R. ANHOLT and H. GOULD, *Adv. Atom. Mol. Phys.* **22**, 315 (1986).
- [27] J. EICHLER, *Phys. Rev. A* **32**, 112 (1985).
- [28] J. EICHLER and W. E. MEYERHOF, "Lectures on Ion-Atom Collisions: From Nonrelativistic to Relativistic Velocities", Elsevier Amsterdam, (2005).
- [29] X. MA, P. H. MOKLER, F. BOSCH, A. GUMBERIDZE, C. KOZHUHAROV, D. LIESEN, D. SIERPOWSKI, Z. STACHURA, T. STOEHLKER, and A. WARCZACK, *Phys. Rev. A* **68**, 042712 (2003).
- [30] A. SURZHYKOV, T. STOEHLKER, and S. FRITZSCHE, *Phys. Rev. A* **74**, 052710 (2006).
- [31] J. J. SAKURAI, "Advanced Quantum Mechanics", John Wiley New York, (1975).

- 
- [32] J. D. JACKSON, " *Classical Electrodynamics*", John Wiley New York, (1975).
- [33] J. BANG and J. M. HANSTEEN, *Mat. Fys. Medd. K. Dan. Vidensk. Selsk.* **31**, 13 (1959).
- [34] J. M. HANSTEEN, O. M. JOHNSON, and L. KOEBACH, *At. Data Nucl. Data Tables* **15**, 305 (1975).
- [35] D. TRAUTMANN and F. RÖSEL, *Nucl. Instrum. Methods* **169**, 259 (1980).
- [36] R. ANHOLT, *Phys. Rev. A* **19**, 1004 (1979).
- [37] T. STOEHLKER, D. C. IONESCU, P. RYMUZA, T. LUDZIEJEWSKI, P. H. M. C. SCHEIDENBERGER, F. BOSCH, H. GEISSEL, O. KLEPPER, C. KOZHUHAROV, R. MOSHAMMER, F. NICKEL, H. REICH, Z. STACHURA, and A. WARCZACK, *Nucl. Instrum. Methods Phys. Res. B* **124**, 160 (1997).
- [38] H. F. KRAUSE, C. R. VANE, S. DATZ, P. GRAFSTRÖM, H. KNUDSEN, C. SCHEIDENBERGER, and R. H. SCHUCH, *Phys. Rev. Lett.* **80**, 1190 (1998).
- [39] T. LUDZIEJEWSKI, T. STOEHLKER, D. C. IONESCU, P. RYMUZA, H. BEYER, F. BOSCH, C. KOZHUHAROV, A. KRÄMER, D. LIESEN, P. H. MOKLER, Z. STACHURA, P. SWIAT, and R. W. DUNFORD, *Phys. Rev. A* **61**, 052706 (2000).
- [40] F. COESTER, *Phys. Rev.* **84**, 1259 (1951).
- [41] J. EICHLER and T. STOEHLKER, *Phys. Rep.* **439** (2007).
- [42] J. R. OPPENHEIMER, *Nucl. Phys.* **31**, 349 (1928).
- [43] T. STOEHLKER, D. C. IONESCU, P. RYMUZA, F. BOSCH, H. GEISSEL, C. KOZHUHAROV, T. LUDZIEJEWSKI, P. H. MOKLER, C. SCHEIDENBERGER, Z. STACHURA, A. WARCZACK, and R. W. DUNFORD, *Phys. Rev. A* **57**, 845 (1998).



- [44] M. STOBBE, *Ann. Phys.* **7**, 661 (1930).
- [45] A. ICHIHARA, T. SHIRAI, and J. EICHLER, *Phys. Rev. A* **54**, 4954 (1996).
- [46] A. ICHIHARA and J. EICHLER, *Atomic Data and Nuclear Data Tables A* **79**, 187 (2001).
- [47] J. EICHLER and A. ICHIHARA, *Phys. Rev. A* **65**, 052716 (2002).
- [48] S. FRITZSCHE, A. SURZHYKOV, and T. STOEHLKER, *Phys. Rev. A* **72**, 012704 (2005).
- [49] J. EICHLER, *Phys. Rev. A* **58**, 2128 (1998).
- [50] E. G. BEREZHKO and N. M. KABACHNIK, *J. Phys. Rev. B* **10**, 2467 (1977).
- [51] V. V. BALASHOV, A. N. GRUM-GRZHIMAILO, and N. M. KABACHNIK, "Polarization and Correlation Phenomena in Atomic Collisions", Kluwer Academic New York, (2000).
- [52] J. EICHLER, *Nucl. Phys. A* **572**, 147 (1994).
- [53] A. SURZHYKOV, U. D. JENTSCHURA, T. STOEHLKER, and S. FRITZSCHE, *Eur. Phys. J. D* **46**, 27 (2008).
- [54] E. G. DRUKAREV, X. MA, A. I. MIKHAILOV, I. A. MIKHAILOV, and P. H. MOKLER, *Phys. Rev. A* **74**, 022717 (2006).
- [55] A. SURZHYKOV, U. D. JENTSCHURA, T. STOEHLKER, and S. FRITZSCHE, *Phys. Rev. A* **73**, 032716 (2006).
- [56] A. SURZHYKOV, S. FRITZSCHE, A. GUMBERIDZE, and T. STOEHLKER, *Phys. Rev. Lett.* **88**, 153001 (2002).
- [57] P. SPÄDTKE, J. BOSSLER, H. EMIG, K. LEIBLE, M. KHAOULI, C. MÜHLE, S. SCHENNACH, H. SCHULTE, and K. TINSCHERT, *C. Hill and M. Vertenar editors "Proceedings of the XVIII international linear accelerator conference", Geneva, Switzerland* (1996).

- 
- [58] P. SPÄDTKE, F. HEZMACH, R. HOLLINGER, R. IANNUCCI, R. LANG, H. REICH, H. SCHULTE, and K. TINSCHERT, *GSI Annual Report 2000, Darmstadt, Germany* .
- [59] B. H. WOLF, H. EMIG, D. RÜCK, and P. SPÄDTKE, *Rev. Sci. Instrum.* **65** , 3091 (1994).
- [60] E. OKS, P. SPÄDTKE, H. EMIG, and B. H. WOLF, *Rev. Sci. Instr.* **65** , 3109 (1994).
- [61] N. ANGERT, W. BOURGEOIS, H. EMIG, B. FRANZKE, B. LANGENBECK, K. D. LEIBLE, H. SCHULTE, P. SPÄDTKE, and B. WOLF, " *Proceedings of the European Particle Accelerator Conference* ", 1436, (1988).
- [62] M. STECK, P. BELLER, K. BECKERT, B. FRANZKE, and F. NOLDEN, *Nucl. Instr. Meth. A* **532** , 357 (2004).
- [63] M. STECK, K. BECKERT, H. EICKHOFF, B. FRANZKE, F. NOLDEN, and P. SPÄDTKE, " *Proceedings of the 1993 particle accelerator conference* ", 1738, (1993).
- [64] M. STECK, K. BECKERT, P. BELLER, B. FRANZKE, F. NOLDEN, U. POPP, and A. SCHWINN, *Physica Scripta* **T104** , 64 (2003).
- [65] G. Weber, GSI Darmstadt, Private Communication (2008).
- [66] Ch. Dimopoulou, GSI Darmstadt, Private Communication (2008).
- [67] B. FRANZKE, *GSI-ESR/TN-86-01 (Internal Report)* (1986).
- [68] B. FRANZKE, *Nucl. Instr. Meth B* **24/25** , 18 (1987).
- [69] H. REICH, W. BOURGEOIS, B. FRANZKE, A. KRITZER, and V. VARENTOV, *Nucl. Phys. A* **626** , 417c (1997).
- [70] A. KRÄMER, Ph. D. Thesis, Universität Frankfurt, (2000).
- [71] O. KLEPPER and C. KOZHUHAROV, *Nucl. Instr. in Physics Research B* **204** , 553 ((2003)).

- [72] G. F. KNOLL, "Radiation detection and measurement", John Wiley and Sons, (1989).
- [73] F. SAULI, *Lectures given in the Academic Training Programm of CERN 1975-1976*, CERN **77-09**, Geneva (1977).
- [74] H. GÖRINGER, S. GRALLA, P. MALZACHER, M. RICHTER, D. SCHALL, and K. WINKELMANN, *GSI Annual Report 1988, Darmstadt, Germany*.
- [75] A. N. ARTEMYEV, V. M. SHABAEV, V. A. YEROKHIN, G. PLUNIEN, and G. SOFF, *Phys. Rev. A* **71**, 062104 (2005).
- [76] C. MUELLER, "The Theory of Relativity", Oxford University Press, (1952).
- [77] J. S. HANSEN, J. C. MCGEORGE, W. D. SCHMIDT-OTT, and R. W. FINK, *Nucl. Instr. and Meth.* **106**, 365 (1973).
- [78] W. R. LEO, "Techniques for Nuclear and Particle Physics Experiments", Springer Verlag, (1994).
- [79] S. TASHENOV, Ph.D. thesis, Universität Frankfurt, (2005).
- [80] J. S. HANSEN, Ph.D. thesis, Georgia Institute of Technology, (1971).
- [81] J. A. BEARDEN, *Rev. Mod. Phys.* **39**, 78 (1967).
- [82] W. HARTL and J. W. HAMMER, *Z. Phys. A* **279**, 135 (1976).
- [83] B. B. DHAL and H. C. PADHI, *Phys. Rev. A* **50**, 1096 (1994).
- [84] MATHEMATICA, *Wolfram Research*, <http://www.wolfram.com> (2005).
- [85] A. N. KHOPERSKII, A. M. NADOLINSKII, V. A. YAVANA, and A. S. KASPRZHITSKII, *Optics and Spectroscopy* **103**, 694 (2007).
- [86] D. C. IONESCU and T. STOEHLKER, *Phys. Rev. A* **67**, 022705 (2003).

- 
- [87] T. STOEHLKER, D. BANAS, S. FRITZSCHE, A. GUMBERIRDZE, C. KOZHUHAROV, X. MA, A. ORSIC-MTHIG, U. SPILLMANN, D. SIERPOWSKI, A. SURZHYKOV, S. TASHENOV, and A. WARCZAK, *Phys. Scr.*, **T 110**, 384 (2004).
- [88] T. STOEHLKER, X. MA, T. LUDZIEWSKI, H. F. BEYER, F. BOSCH, O. BRINZANESCU, R. W. DUNFORD, J. EICHLER, S. HAGMANN, A. ICHIHARA, C. KOZHUHAROV, A. KRÄMER, D. LIESEN, P. H. MOKLER, Z. STACHURA, P. SWIAT, and A. WARCZACK, *Phys. Rev. Lett.* **86**, 983 (2001).
- [89] T. STOEHLKER, T. LUDZIEJEWSKI, F. BOSCH, R. W. DUNFORD, C. KOZHUHAROV, P. H. MOKLER, H. F. BEYER, O. BRINZANESCU, B. FRANZKE, J. EICHLER, A. GRIEGAL, S. HAGMANN, A. ICHIHARA, A. KRÄMER, J. LEKKI, D. LIESEN, F. NOLDEN, H. REICH, P. RYMUZA, Z. STACHURA, M. STECK, P. SWIAT, and A. WARCZAK, *Phys. Rev. Lett* **82**, 3232 (1999).

# *Acknowledgements*

It is minimum I can do to dedicate the successful work to my **God**. I truly thank my **God** every time for his support and care which helped me to overcome the frequent moments of disappointment me throughout the years of my Ph.D. From my experience, I can realize that the patience is the key to relief.

Next, I would like to direct many thanks to **Prof. Dr. Heinz-Jürgen Kluge** for his acceptance of me to do my PhD work in GSI institute.

Also, I'm very thankful to **Prof. Dr. Reinhard Dörner** for the acceptance and admittance of me as a PhD student in Frankfurt University.

I would like to express my very special thanks to **Prof. Dr. Thomas Stöhlker** for giving me the opportunity to pursue the research work at the ESR, and providing me the financial support by the **GSI Helmholtzzentrum für Schwerionenforschung GmbH** (*Darmstadt/Germany*) throughout the thesis work. In addition, I have learnt from him a lot of physics. I am infinitely grateful to him for encouragement, support and guidance throughout this work. His trust towards my work is also highly appreciated.

In the four years I spent in this PhD work, I have had the great pleasure to work with my direct advisor **Dr. Angela Bräuning-Demian** who introduced me into the field of experimental atomic physics. She has demonstrated nearly infinite patience in discussing my work. I thank Angela also for encouragement, guidance, support and availability.

I wish to express my thanks to **Dr. Andrey Surzhykov** and **Dr. Stephan Fritzsche** for performing the theoretical calculations.

Pleasantly, I would like to direct my thanks to my colleagues in the atomic physics department: **Prof. Dr. P.H. Mokler**, **Dr. Ch. Kozhuharov**, **Dr. Harald Bräuning**, **Prof. F. Bosch**, **Prof. D. Liesen**, **Dr. H. Beyer**, **Dr. W. Nörtershäuser**, **O. Kester**, and **S. Lüttges**, **U. Spillmann**, **R. Reuschel**, **A. Gumberidze**, **S. Trotsenko**, **S. Heß**, **S. Tachenov**, **C. Brandau**.

Also, I thank my dear friends **Dr. M. Nofal** and **Dr. M. Al-Turany** who helped me starting my life in Germany.

My great wife **Alaa Issa** deserves a special mention in this acknowledgement for her distinguished emotional support which kept me in great spirits throughout my PhD work. I thank **Alaa** for patience, understanding, bearing my absence during the working hours, and for the many happy moments we spent together. The presence of my daughter **Jory** has been a singular source of joy during the process of this work. I thank them for the nice environment at home.

I would like to express my very special gratefulness to my parents, **Mohammad Salem** and **Fathia Salem**, who have been a great source of support and encouragement throughout my life. I thank both for their financial support and arrangements for my wedding party in Amman/Jordan. My **family in-law** in Syria and have also been very supportive and encouraging. I am also grateful to the rest of my family members and friends in Jordan, those who, in spite of the distance, were always close to me and conveyed the familiar feeling of home.

And last but not least, I would like to express my gratitude to all those people who have contributed to the completion and success of this work. I apologize if I have accidentally omitted somebody to whom acknowledgement is due.

*Shadi Salem*

# *Curriculum Vitae*

## *Personal Information:*

Name : Shadi Salem  
Date of Birth : 26.05.1978  
Place of Birth : Khafji-Saudi Arabia.  
Nationality : Jordanian.  
Marital status : Married, One Child.  
E-mail : S.Salem@gsi.de

## *Academic Qualifications:*

B.Sc. Physics : The Hashemite University, Zarqa, Jordan, June 2000.  
M.Sc. Solid State Physics : University of Jordan, Amman, Jordan, February 2003.  
Ph.D. Atomic Physics : Frankfurt University, Institute of Nuclear Physics,  
Germany, January 2010.

## *Work Experience:*

Feb./2001 - Jan./2005 : Teaching and Research Assistant, Physics Department,  
University of Jordan, Amman, Jordan.  
Feb./2005 - Dec./2009 : Ph.D. Research, GSI, Germany.